Coordination Chemistry Reviews 458 (2022) 214428

Contents lists available at ScienceDirect

Coordination Chemistry Reviews

journal homepage: www.elsevier.com/locate/ccr

Review

Modified UiO-66 as photocatalysts for boosting the carbon-neutral energy cycle and solving environmental remediation issues

Hongda Liu [a,b], Min Cheng [a,b,*], Yang Liu [c,*], Gaoxia Zhang [a,b], Ling Li [a,b], Li Du [a,b], Bo Li [a,b], Sa Xiao [a,b], Guangfu Wang [a,b], Xiaofeng Yang [a,b]

[a] College of Environmental Science and Engineering, Hunan University, Changsha, Hunan 410082, China
[b] Key Laboratory of Environmental Biology and Pollution Control (Hunan University), Ministry of Education, Changsha, Hunan 410082, China
[c] School of Minerals Processing and Bioengineering, Key Laboratory of Biohydrometallurgy of Ministry of Education, Central South University, Changsha, 410083, China

ARTICLE INFO

Article history:
Received 29 June 2021
Accepted 18 January 2022
Available online xxxx

Keywords:
Metal–organic frameworks
UiO-66
Photocatalysts
Modifications
Applications

ABSTRACT

UiO-66, a water-resistant zirconium-based metal–organic framework (MOF) with ultra-high porosity, larger surface area and plentiful active sites, has an advantage over conventional photocatalysts. Notably, its excellent environmental resistances (chemical, hydrothermal and mechanical stability) make it more competent for practical applications than other types of MOFs. Furthermore, the photoresponse range and charge separation efficiency of UiO-66 can be significantly improved by rational design and adjustment. In this review, we aim to provide an overview of the latest advances in the modification and design of UiO-66 for photocatalytic applications, including the selection of metal node, the functionalization of organic linker, defect engineering, foreign metal loading, dye sensitization, and combination with semiconductors. Then, the applications of modified UiO-66 photocatalysts in CO_2 reduction, hydrogen generation, organic pollutants removal, Cr(VI) reduction and so on, are elaborated. In particular, the reaction mechanisms are principally highlighted. Finally, referencing these studies, future insights and perspectives are proposed. Our intention is to comprehensively review various modified UiO-66 photocatalysts, which can stimulate for the design of efficient photocatalysts to make better utilization of solar energy.

Contents

Abbreviations: MOF, metal–organic framework; Cr, chromium; UV, ultraviolet; H2BDC, terephthalic acids; DMF, N, N-dimethylformamide; SEM, scanning electron microscopy; LMCT, linker-to-metal charge-transfer; HOMO, highest occupied molecular orbital; LUMO, lowest unoccupied molecular orbital; VB, valence band; CB, conduction band; RhB, Rhodamine B; XRD, X-ray diffractometry; DFT, density functional theory; ESR, electron spin resonance; OV, oxygen vacancy; Vis, visible; DRS, diffuse reflectance spectra; H_2ATA, amino-functionalized benzoic acids; MCCT, metal-to-cluster; MMCT, metal-to-metal charge transfer; NPs, nanoparticles; LSPR, local surface plasmon resonance; SAs, single-atom catalysts; EY, Eosin Y; ErB, Erythrosine B; PL, photoluminescence; COF, covalent organic framework; g-C_3N_4, graphitic carbon nitrides; MB, methylene blue; CDs, carbon nanodots; TCH, tetracycline hydrochloride; NHE, normal hydrogen electrode; •OH, hydroxyl radical; TCPP, tetra(4-carboxylphenyl) porphyrin; rGO, reduced graphene oxide; CNTs, carbon nanotubes; GR, graphene; DF, diclofenac; TC, tetracycline.

* Corresponding author at: College of Environmental Science and Engineering, Hunan University, Changsha, Hunan 410082, China (M. Cheng); School of Minerals Processing and Bioengineering, Key Laboratory of Biohydrometallurgy of Ministry of Education, Central South University, Changsha, 410083, China (Y. Liu).

E-mail addresses: chengmin@hnu.edu.cn (M. Cheng), liuyang_feiyang@163.com (Y. Liu).

https://doi.org/10.1016/j.ccr.2022.214428
0010-8545/

1. Introduction

With accelerating of industrialization, the increasing consumption of fossil fuels (oil, coal, natural gas, etc.) has triggered various environmental issues and global energy challenges [1,2]. As awareness of energy scarcity and environmental protection grows, significant efforts have been devoted to the exploitation of sustainable energy resources [3-5]. Among all possible options, solar energy, with its huge reverses, reliable, efficient, and environmental-friendly, has been considered as the best energy resource to promote the carbon–neutral energy cycle and solve environmental remediation issues for maintaining a sustainable planet [6-8]. Afterwards, artificial photocatalysis was initially developed by Fujishima in 1972 s and TiO_2 was used as a photocatalyst to drive water splitting under ultraviolet (UV) irradiation but with low efficiency [9]. Accordingly, the active pursuit of effective and satisfactory photocatalytic materials for overcoming deteriorating energy crises and environmental problems is being carried out.

In recent years, metal–organic frameworks (MOFs), structured by linking metal-containing units (secondary structural units) with organic linkers, is emerged as a new class of coordination polymers with finely tunable and permanent pore structures [10-13]. They have enjoyed widespread interest in many areas, including photocatalysis [14-17]. To be specific, MOFs are so fascinating as photocatalysts because of the following points: (a) the ultrahigh porosity and large specific surface area of MOFs could allow for high-density adsorption and photocatalytic sites [18-21]; (b) the metal ions/clusters or organic linkers in MOFs could be photoexcited to generate photogenerated electrons and holes under illumination [22,23]; (c) the variety of combinations between clusters and linkers hold great promise for rational design of MOFs in terms of photofunctionality; (d) the intrinsic porous structure of MOFs is favorable for substrates and products transportation in photocatalytic processes [24-26], and may provide additional channels for the migration of photogenerated electrons, thus facilitating the separation of photogenerated carriers [27]; and (e) pre-synthetic and post-synthetic modifications of MOFs with rational function and photoactive components can improve photocatalytic performance [28].

Within the various types of MOFs, UiO-66 ($Zr_6O_4(OH)_4(BDC)_{12}$), the water-resistant zirconium-based MOF composed of Zr-based building bricks and terephthalic acids (H_2BDC) linkers, has attracted great attention since its first discovery by Lillerud's group [18]. Each $Zr_6O_4(OH)_4$ octahedron is coordinated with 12 H_2BDC, which is the highest coordination within the reported MOFs. Since the pioneering discovery by Garcia et al. [29] that UiO-66 featured intrinsic photocatalytic hydrogen generation activity under UV irradiation, it has been intensively investigated in the heterogeneous photocatalysis. The advantages of UiO-66, such as large specific surface area, high porosity, low density, and diversity of topological structure, which make it more suitable for photocatalysis than conventional inorganic semiconductor photocatalysts [30-33]. In particular, UiO-66 features superior environmental resistances (chemical, hydrothermal and mechanical stability) to other MOFs. The thermal stability of most reported MOFs is restricted to between 350 and 400 °C, however, UiO-66 can still be unprecedented stable at 540 °C due to the strong Zr-O bond with high coordination number [18]. Stability is a major issue for MOFs used in practical applications [34,35]. However, by virtue of the highly oxygenophilic capability of Zr^{4+}, UiO-66 can be robust and inert under various aggressive chemical conditions (benzene, ethanol, acetone, etc.) and elevated pressures [18,36]. These distinctive advantages of UiO-66, which are unavailable in other MOFs, are of particular relevance as these remarkable resistances give UiO-66 inherent benefits over other MOFs in photocatalysis, particularly under harsh conditions. Also, under UV illumination, energy can be transferred from the organic linker H_2BDC to the Zr oxo cluster in UiO-66 [37]. Therefore, UiO-66 can be directly applied as a photocatalyst in various photocatalytic systems. Nevertheless, there are some problems with UiO-66 in photocatalysis. It is worth noting that although UiO-66 exhibit intrinsic photoresponse, its photoactivity is not superior to that of conventional semiconductor photocatalysts [30,32]. Moreover, UiO-66 possesses miserable UV absorption with an absorption range edge around 310 nm due to π-π electronic jumping of the aromatic ring in H_2BDC, unlike other zirconium–porphyrinic MOFs (e.g., PCN-224) with visible light response, which limits its light utilization in the visible light region [38,39]. This suggests that UiO-66 accounts for only 4% of overall solar energy, which largely limits the practical photocatalytic applications [37]. Furthermore, compared with MIL-125, which also has similar UV absorption and wide band gap (about 3.6 eV), but the electron transfer from the excited organic linker to the Zr oxo cluster of UiO-66 appears to be inefficient because the Zr oxo cluster has a highly redox potential energy level, leading to the deficient transfer and separation efficiency of photogenerated charge carries [40]. Fortunately, due to the modular nature of UiO-66, it can be easily tailored by various functional metal nodes/linkers, defect engineering or different photofunctional components coupling to achieve light-responsive, high efficiency of charge transfer and high-performance in photocatalysis [41-44]. More importantly, the structural stability of UiO-66 can still be maintained after the incorporation of active functional groups [45]. Summarizing, in sharp contrast to most reported MOFs, UiO-66 is a remarkably intriguing material with unlimited

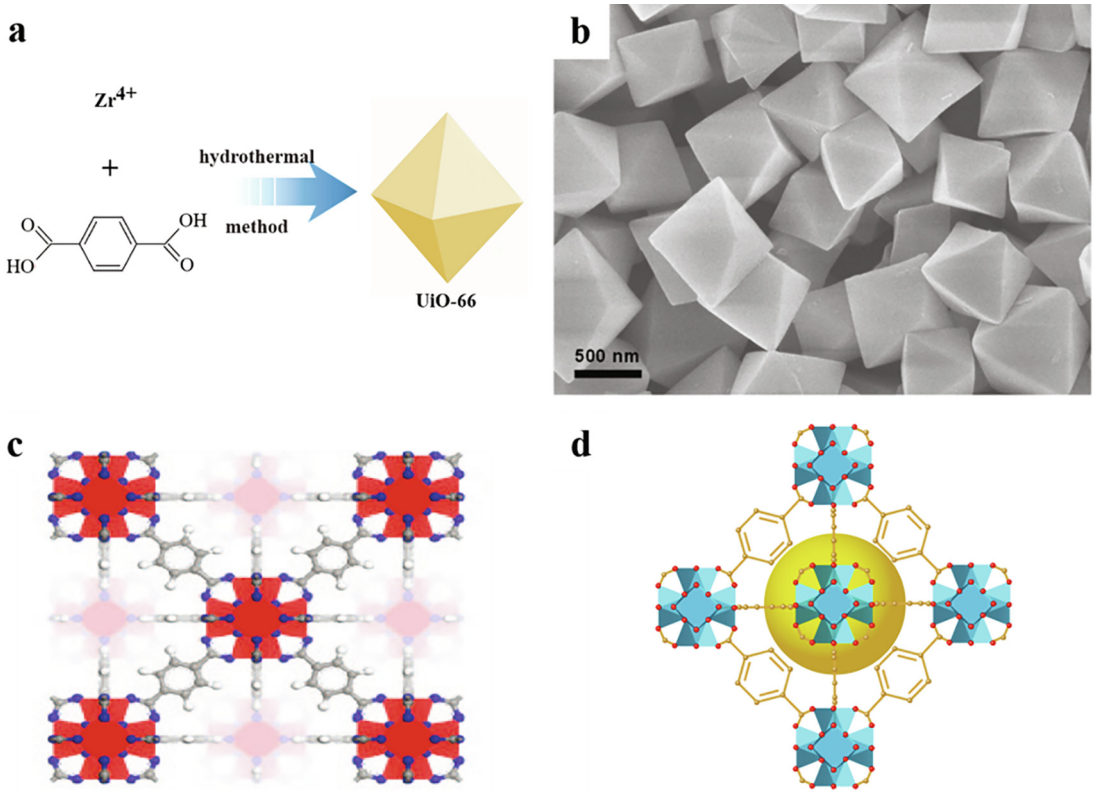

Fig. 1. (a) Schematic diagram of the UiO-66 synthesis; (b) SEM images of UiO-66; (c) simulated configuration of UiO-66, the zirconium, carbon, oxygen and hydrogen atoms are red, grey, blue and white, respectively; (d) clear simulated conformation of UiO-66. Adapted with permission from Ref. [18,67], Copyright 2008 and 2018, American Chemical Society. (For interpretation of the references to colour in this figure legend, the reader is referred to the web version of this article.)

potential for photocatalytic applications in aqueous medium, even in harsh conditions.

Up to date, several review papers covering general aspects of various MOFs/MOFs derivatives have been published [46-50]. For example, Dhakshinamoorthy et al. [37] discussed the advantages, uniqueness, optimal design and applications of MOFs in photocatalysis. Recently, Kolobov et al. [51] reviewed how MOFs in photocatalysis worked like conventional semiconductors and how they acted like infinite molecules in solution. The exploitation of UiO-66 for light-harvesting and photocatalytic applications began with Garcia et al. [29], who investigated hydrogen generation under UV light from UiO-66 and amino-functionalized UiO-66. From then on, UiO-66 was also developed for other photocatalytic reactions, including Cr(VI) reduction, oxidation of alcohols, and CO_2 reduction [52-54]. Meanwhile, in recent years, the exploitation and modification of UiO-66 as photocatalyst have achieved ameliorated photocatalytic performance and multifunctional development in photocatalytic applications [55-57]. However, the photocatalytic applications of UiO-66 to boost the carbon–neutral energy cycle and address environmental remediation issues have only been briefly described in some reviews, and their superior properties in photocatalysis have not been elaborated [58,59]. For instance, Xiang et al. [60] reviewed the synthesis, characterization and application of defective metal organic skeletons, however, the unique advantages of UiO-66 for photocatalysis have rarely been discussed. Therefore, it is quite essential to clearly summarize the structure, modification methods, and applications of UiO-66 in photocatalysis to provide researchers with a fundamental and valuable guidance for the rational layout and research of UiO-66-related photocatalysts.

2. Structure of UiO-66

Understanding the structure of the basic UiO-66 is a prerequisite for experimental research. The hydrothermal method is the most typical and effective method to obtain high-quality UiO-66 (Fig. 1a). In general, zirconium source $ZrCl_4$ and the organic linkers H_2BDC were dissolved in the solvent DMF (N, N-dimethylformamide), followed by adding acetic acid to form a crystalline mother liquor, the obtained mixture was then crystallized at 120 °C with 24 h. After filtration, the white solid was thoroughly washed in DMF and dried to obtain solid samples of UiO-66 [61]. However, most of these procedures require solvothermal synthesis at relatively high temperature ranges and over long periods of time (24 h), which is not conductive to the practical applications of UiO-66. Based on this, several studies have attempted to synthesize high-quality UiO-66 by solution-based synthesis at lower temperatures [62,63]. Surprisingly, the crystallinity and porosity of the UiO-66 synthesized by DeStefano et al. [64] at room temperature were the same as those obtained at elevated temperatures. The two-step synthesis procedure began with the preformation of the secondary building unit intermediate at high temperature, followed by its combination with the H_2BDC at room temperature. In order to avoid the use of high temperatures, strong acids, high temperatures or excess reactants, liquid-assisted grinding and solvent-free routes for the synthesis of UiO-66 have been developed, which can enable yields in the gram range [65]. By using a Spex 8000 mill, 3 g of highly porous UiO-66 could be synthesized in 75 min through liquid-assisted grinding $Zr_6O_4(OH)_4(C_2H_3CO_2)_{12}$ and H_2BDC with methanol. For the solvent-free and low-energy method, a physical mixture of $Zr_6O_4(OH)_4(C_2H_3CO_2)_{12}$ and H_2BDC

was ground for a short time and subsequently exposed to methanol vapour at 45 ℃, leading to the spontaneous assembly of UiO-66. Furthermore, film deposition greatly increased the feasibility of integrating UiO-66 into practical applications [66]. Specifically, the Zr^{4+} generated by the corrosion of the anodic zirconium foil was coordinated with the deprotonated BDC^{2-} in the solvent to form the UiO-66 film covering the cathode and anode zirconium foils.

Generally, the obtained UiO-66 crystals exhibit a well-defined octahedral outline with a smooth surface as shown by scanning electron microscopy (SEM) (Fig. 1b) [67]. The octahedral structural unit of UiO-66 is made up of $(Zr_6O_4(OH)_4)$ metal clusters linked to 12 H_2BDC coordination units. The six vertices of the Zr_6-octahedron are occupied by Zr^{4+} and the eight triangular faces are covered by four μ_3-O and μ_3-OH groups, a three-dimensional microporous structure with an octahedral central hole cage (7.2 Å) and eight tetrahedral corner cages (6.8 Å) (Fig. 1 c,d) [18]. The theoretical values of specific surface area is 1187 m^2/g [18]. The poor stability of MOFs due to the invertible nature of coordination bonds is generally considered to be the main obstacle to their practical applications [34,35]. However, this does not occur in UiO-66. The metal-linker bond strength is thought to be a major factor in determining the stability of MOFs [68]. Due to the bond polarization and high charge density, the strong affinity between carboxylate O atoms and Zr^{4+} can be formed in UiO-66 [36]. Thus, UiO-66 features remarkable thermal and chemical stability as well as mechanical stability beyond most reported MOFs [69]. Even at 540 °C or a high mechanical pressure of 1.0 MPa, UiO-66 can preserve the integrity of its octahedral structure [18]. Moreover, it can be incredibly resistant to chemicals, including benzene, acetone, acid and DMF [70]. Silva et al. [29] tested in the laboratory that UiO-66 can be suspended in water for 4 h without changing the porous structure even at 100 °C. All of these unique advantages offer unlimited potential for photocatalytic applications of UiO-66.

It is noteworthy that UiO-66 is suitable as a semiconductor material because of its intrinsic photocatalytic activity [29]. Meanwhile, UiO-66 has a characteristic UV absorption range edge around 310 nm, which can be attributed to π-π electronic jumping of the aromatic ring in the organic linker H_2BDC [71]. Therefore, under illumination, in the presence of the metal centers Zr and organic linkers H_2BDC, UiO-66 can be photoexcited to generate photogenerated electron-hole pairs, and photogenerated electron transferred from the photoexcited H_2BDC to the Zr oxo clusters in UiO-66 to generate Zr^{3+} [37]. Through such a linker-to-metal charge-transfer (LMCT) process, the highest occupied molecular orbital (HOMO) of UiO-66 is formed by the unoccupied d orbitals of metal centers, and the lowest unoccupied molecular orbital (LUMO) is mainly constructed by the outer orbitals of organic linkers H_2BDC. However, there is a major limitation for its photocatalytic activity. The redox potential energy level of Zr oxo clusters in UiO-66 is higher than that of LUMO in organic linker H_2BDC [72,73]. Therefore, it is difficult to accept photogenerated electrons from the organic linker H_2BDC, leading to inefficient charge transfer from H_2BDC to the Zr oxo clusters. Although the above reasons lead to a relatively wide band gap of UiO-66, which make it somewhat difficult to be photoexcited under visible light, certain modification strategies can be used to overcome this problem and develop efficient UiO-66-based photocatalysts.

3. Functional design of UiO-66

Actually, UiO-66 has three types of active sites, including metal nodes, organic linkers and guest active species (Fig. 2a), which can be functionally modified with several methods to improve its photocatalytic performance, including (a) selecting functional metal sites or organic linker to reduce the band gap between the valence band (VB) and the conduction band (CB), therefore strengthening its photoresponse range; (b) defect engineering to modulate energy band and electronic structures together with tailored material properties; (c) introducing metal modifications to create another channel for charge separation and transfer, thereby enhancing charge separation efficiency; (d) constructing dye sensitization system to endow UiO-66 with visible light harvesting; and (e) combining with other photoactive semiconductors to engender matched band gap, facilitating separation and transfer of photogenerated charge carriers, thus promoting photocatalytic activity. These methods are specified below (Fig. 2b).

3.1. Functionalize organic linker H_2BDC

Functionalized organic linker H_2BDC is an effective way to improve the photoresponse [74]. The modification of UiO-66 for light-harvesting began with Silva et al. [29], who used the synthesized amino-functionalized UiO-66 (UiO-66-NH_2) for hydrogen generation. They demonstrated that the $-NH_2$ group caused a shift in the absorption spectrum towards the visible range (the strong absorption band from 300 ~ 440 nm with a peak at 360 nm), compared to the absorption range of UiO-66 (270 ~ 300 nm). The pres-

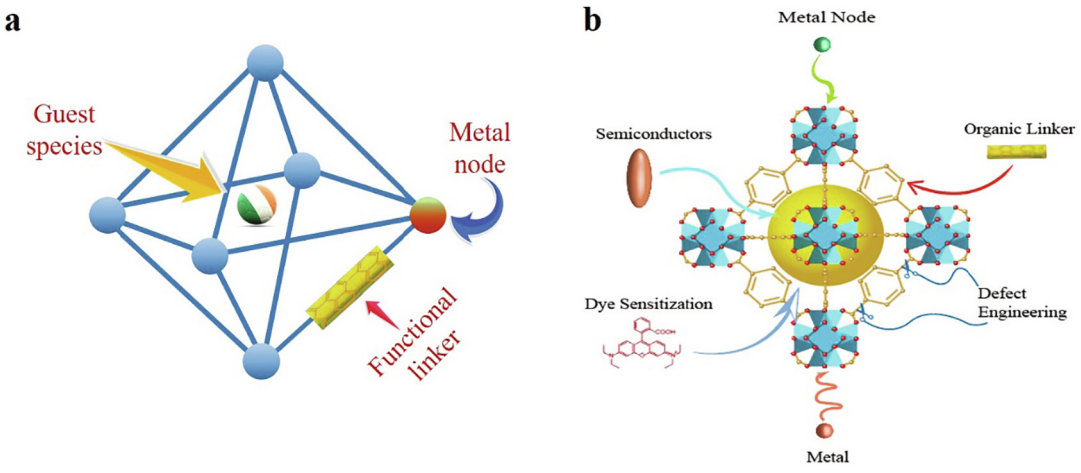

Fig. 2. (a) Schematic illustration of the active sites available for modification of UiO-66, including metal nodes, organic ligands and guest active species. (b) The specific modifications to UiO-66, including selecting functional metal nodes or organic linkers, defect engineering, metal modifications, constructing dye sensitization system, combing with other photoactive semiconductors.

Table 1
Optical properties after modification of the benzene ring on H_2BDC in UiO-66.

Organic linkers	Optical absorption edge (nm)	Band gap (eV)	Ref.
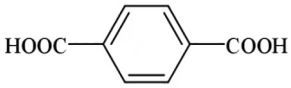	330 nm	3.91 eV	[74,76]
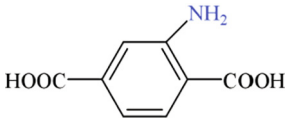	450 nm	2.83 eV	[76]
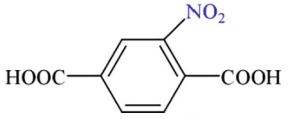	400 nm	–	[74]
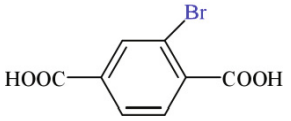	355 nm	3.88 eV	[74]
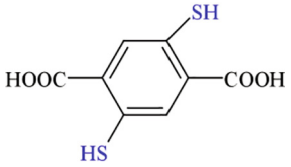	450 nm	2.75 eV	[42,76,78,121]
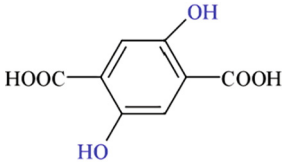	490 nm	2.69 eV	[76]
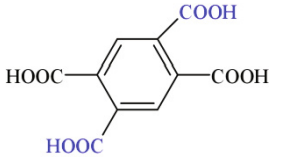	~340 nm	3.62 eV	[77]
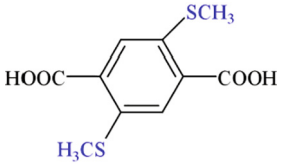	470 nm	2.80 eV	[42]
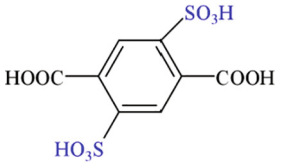	425 nm	3.22 eV	[42]

ence of $-NH_2$ was crucial for enhancing the photocatalytic performance of UiO-66. Under optimum conditions, the maximum hydrogen volume of UiO-66-NH_2 was 2.8 mL after 3 h, higher than the 2.4 mL of UiO-66. Subsequently, Sun et al. [54] prepared mixed UiO-66-NH_2/UiO-66–2,5-NH_2 by introducing a second amino group to the partially amino-functionalized H_2BDC, which exhibited enhanced visible light absorption and photocatalytic activity for CO_2 reduction compared to UiO-66-NH_2. This study fully demonstrated that further enhancement of light absorption can be achieved by increasing the number of functional groups in the organic linker or by a mixed-linker approach. It was further confirmed by Hendrickx et al. [75]. The authors investigated the effect of modifying single and double electron-donating groups (OH, NH_2, SH) on organic functional groups on the intrinsic light absorption capacity by means of theoretical and experimental studies. In the cases of monofunctionalization, the maximum absorption of visible light increased from OH to NH_2 to SH, and this effect was further enhanced in bifunctionalized cases. The band gap of UiO-66 can be tailored from 4.0 eV to 2.2 eV. This were because these introductions allowed the LUMO to remain in situ while the HOMO band moved upwards with the contribution of the electron-donating groups, producing a fully filled energy gap state and an effective reduced band gap. In 2019, Chen et al. [42] systematically synthesized UiO-66-X_2 by modifying H_2BDC with different X groups (X = -SH, -SCH_3, -SO_3H) to study the effect of sulfur-containing groups modification on the band gap and photoactive features of UiO-66. The obtained UiO-66-X_2 (X = -SH, -SCH_3, -SO_3H) showed band edges of around 440, 470 and 425 nm compared to the poor UV absorption of UiO-66 (320 nm), respectively. The authors suggested that the electron donating capacity, geometry and dimensions of the X group performed a decisive role in determining the band gap of UiO-66-X_2. -SCH_3 was the strongest functional group causing the remarkably decreased band gap and enhanced photocatalytic performance of UiO-66$(SCH_3)_2$. Surprisingly, compared to the most representative UiO-66-NH_2 which had no visible light-induced photocatalytic hydrogen generation activity, Pt/UiO-66-$(SCH_3)_2$ exhibited an efficient hydrogen generation rate of 3871 μmol/g under the same reaction conditions. However, in some reactions, the narrow band gap and excellent visible light harvesting ability of modified UiO-66 does not suggest exceptional photocatalytic performance. Mu et al. [76] synthesized UiO-66 as well as its isostructural derivatives UiO-66-X with NH_2, Br, $(OH)_2$, and $(SH)_2$ functional group in aromatic ring of the organic linker H_2BDC for the photodegradation of Rhodamine B (RhB). X-ray diffractometry (XRD) patterns showed that the five samples were isostructural and the substitution of linkers did not affect the crystal structure. Inferred from relevant characterization results, these functional groups were present in the micropores and did not coordinate with metal centers. UV–vis diffuse reflectance spectra (DRS) indicated that the light absorption edges of UiO-66-NH_2, UiO-66-$(OH)_2$ and UiO-66-$(SH)_2$ visibly shifted to the visible light region (Table 1). Although UiO-66-$(OH)_2$ and UiO-66-NH_2 possessed apparent visible light absorption, both had significantly weaker degradation efficiency than UiO-66-Br and UiO-66 with almost no visible light absorption. Therefore, the light absorption ability of modified UiO-66 was not the decisive factor in determining its photocatalytic activity, other properties should also be taken into account, such as the efficiency of charge separation and potential relationship between the target and modified UiO-66. There are also many relevant reports on ligand modifications of UiO-66 and the corresponding photoresponse ranges are shown in Table 1. Even more noteworthy is that the modification of organic linkers may also allow UiO-66 to be better modified by other functional substances in photocatalysis, resulting in better photocatalytic properties and recycling reusability [77,78].

The introduction of functional groups on the organic linkers of UiO-66 will influence the specific surface area, light absorption capacity and electron density around the metal center. In particular, the higher electron density caused by the electron-donating functional groups (–NH_2, -SCH_3 and so on) will reduce absorption energy and increase the potential for absorption in the visible range of solar radiation, thus greatly increasing the photocatalytic performance of the UiO-66. However, the introduction of functional groups plays a restricted role in enhancing the LMCT excitation, and the choice of substituents is limited, which leaves new strategies for modification to be expected in the future. In future research, it will be necessary to consider the effect of electron-donating functional groups on the photocatalytic activity of UiO-66 to better determine the appropriate number of functional

groups on each linker. If possible, the introduction of different groups onto the organic linkers could also be explored to explore if there is a synergistic effect affecting the optical properties of UiO-66.

3.2. Select functional metal nodes

Another strategy to enhance photoresponse is to build mixed metal nodes in UiO-66 [41,73,79]. By introducing new metal nodes, the electron transfer between different metals formed can narrow the effective band gap, which can also contribute to photocatalytic performance by improving the charge separation efficiency [80]. In recent years, Ti^{4+} has been widely introduced as metal node to coexist with the original Zr metal node in UiO-66. Sun et al. [80] first successfully prepared Ti-substituted UiO-66-NH_2(Zr/Ti) using a post-synthetic exchange method, which exhibited enhanced CO_2 reduction (5.8 mmol mol^{-1} in 10 h) and hydrogen generation (3.5 mmol mol^{-1} in 9 h) activities under visible light. In contrast, relatively weak CO_2 reduction (3.4 mmol mol^{-1}) and hydrogen production (2.4 mmol mol^{-1}) activities were obtained using UiO-66-NH_2 as a photocatalyst. The enhanced performance derived from the fact that the introduction of Ti can act as a mediator to facilitate electron transfer as confirmed by density functional theory (DFT) calculations and electron spin resonance (ESR). Concretely, Ti^{4+} in UiO-66-NH_2 (Zr/Ti) can accept most of electrons from the excited state organic linkers to form the excited state $(Ti^{3+}/Zr^{4+})_6O_4(OH)_4$. Due to the overlap of electronic states of Zr and Ti atoms, Ti^{3+} can further transfer electrons via oxo-bridged Ti^{3+}-O-Zr^{4+} to Zr^{4+} to form Ti^{4+}-O-Zr^{3+}. Such electron transfer was very beneficial to enhance the photocatalytic performance as confirmed by other studies [73,79,81,82].

The complete replacement of the Zr node in UiO-66 by Ce to form UiO-66(Ce), has also aroused similarly widespread interest in the field of photocatalysis. Due to the introduction of the low-lying 4f orbital of Ce^{4+}, UiO-66(Ce) can exhibit strong absorption in the ultraviolet–visible region (300–500 nm) and can also promote LMCT with negative LMCT energy, giving it a long-excited state lifetime and outstanding photogenerated carrier separation ability [83-86]. More intriguingly, the Ce^{4+}/Ce^{3+} spontaneous redox cycling can also greatly contribute to the photocatalytic activity of UiO-66(Ce) in redox reactions [87-89]. In 2015, Lammert et al. [88] demonstrated for the first time that UiO-66(Ce) synthesized by DMF solvent method has hexanuclear clusters $[Ce_6O_4(OH)_4]^{12+}$ with strong homology to UiO-66(Zr). Inspired by this work, Campanelli et al. [90] developed a new method for the rapid and facile synthesis of Ce-UiO-66 MOFs, with very small amounts of acetic acid, differently substituted H_2BDC linkers and $Ce(NH_4)_2(NO_3)_6$ as precursors. The theoretical calculations showed that the band gap of the prepared UiO-66(Ce) was 2.99 eV, which was smaller than the 3.91 eV of UiO-66. In the photocatalytic degradation of organic pollutants, owing to the electrostatic interaction between the aromatic ring and the Ce-O bonding/hydrogen bonding, UiO-66(Ce) also can present favorable adsorption capabilities for organic pollutants [85]. Although a number of theoretical calculations suggested that UiO-66(Ce) had sufficient energy to be applied in both oxidation and reduction, more experimental evidence is still needed for these predictions.

Interestingly, it has been shown that Ti 3d can mix more effectively with organic linkers than Ce^{4+} 4f, which facilitates the engineering of band gap to achieve a response to visible light and greatly improve LMCT [83]. Accordingly, Zhang et al. [91] prepared bimetallic UiO-66(Ce/Ti) for the first time by incorporating Ti into UiO-66(Ce) through facile cation exchange, which achieved enormously enhanced photocatalytic performance. Fascinatingly, the authors found the presence of abundant oxygen vacancy (OV) in UiO-66(Ce/Ti) for the first time by ESR, which was created by the transformation of $Ce^{4+} + Ti^{3+} \leftrightarrow Ce^{3+} + Ti^{4+} + OV$. On one hand, the abundant OV could introduce localized states lower than the CB (the CB position shifted from −0.50 eV to −0.40 eV), resulting in more effective LMCT and stronger visible light response than UiO-66(Ce). On the other hand, the abundant OV can further work as the charge carrier trap to maintain photogenerated electrons and holes in the CB and VB, respectively. What's more, the OV could further induce the formation of redox Ce–OV–Ti defects, which can facilitate the enhancement of redox capacity of UiO-66(Ce/Ti). Therefore, the incorporation of Ti can greatly enhance the photocatalytic capacity of the Ce^{4+}/Ce^{3+} redox cycle in UiO-66 (Ce).

The trimetallic UiO-66 may reap unexpected gains in photocatalytic performance with continuously studying the controlled metal node strategy. Melillo et al. [61] developed five types of UiO-66 materials (M: Zr, Zr/Ti, Zr/Ce, Zr/Ce/Ti, Ce) by controlling metal node composition for photocatalytic overall water splitting. Monometallic Zr- or Ce-containing UiO-66 was prepared by conventional means of H_2BDC and $ZrCl_4$ or $Ce(NH_4)_2(NO_3)_6$, respectively. Bimetallic Zr- and Ce-containing UiO-66 (Zr/Ce) was obtained through a mixture of H_2BDC, $ZrCl_4$ and Ce $(NH_4)_2(NO_3)_6$. Other bimetallic and trimetallic UiO-66 (Zr/Ti, Zr/Ce/Ti) were obtained by further ion exchange of the UiO-66 (Zr, Zr/Ce) materials obtained above with the use of $TiCl_4(THF)_2$ as Ti source. Compared to pristine UiO-66, all other samples showed a redshift in light absorption or enhanced light absorption. Based on the UV–Vis DRS, the estimated band gap values of the samples after the modulated metal nodes were all lower than those of pure UiO-66 (Zr). This demonstrated that it is reasonable and effective to enhance photoresponse by modulating the composition of the metal node. Surprisingly, the UiO-66(Ce) exhibited higher visible light absorption but lower activity, and the trimetallic UiO-66 (Zr/Ce/Ti) exhibited the strongest photocatalytic activity for overall water splitting, which could yield 70 μmol g^{-1} of O_2 and 210 μmol g^{-1} of H_2 under visible light irradiation. This suggested that in the case of trimetallic UiO-66, the intensity of light absorption may not be the key factor in determining the photocatalytic activity. The authors ascribed this to the collective cooperation of the three metals within $M_6^{4+}O_4(OH)_4^{12+}$ clusters of UiO-66(Zr/Ce/Ti) with distinct oxidation potentials, which was conducive to the kinetics of the four-electrons-four proton process, thus facilitating the formation of O_2.

As described above, the construction of polymetallic nodes and the functionalization of organic linkers are both beneficial in enhancing the photocatalytic performance. Furthermore, there have been several efforts to combine both modifications in UiO-66 to explore the effects on photocatalytic performance. For instance, An et al. [92] synthesized a kind of modified UiO-66 with bimetallic nodes (Zr and Hf) and functionalized linkers (H_2BDC with chlorine, thiol or hydroxyl groups) for visible-light-driven nitrogen fixation. The Hf was successfully introduced into the metal nodes of UiO-66 to form bimetallic Zr-Hf clusters, and the regular octahedral shape of UiO-66 was retained due to its similar atomic structure to Zr. However, further modified the bimetallic UiO-66 with side-chain groups (-Cl, −2SH or –OH) in H_2BDC, the crystalline structure of UiO-66 also hardly altered, but its morphology was apparently changed. In the metal nodes, the bimetallic Zr-Hf clusters in UiO-66 could be attributed to the adsorption of nitrogen molecules and further activated N≡N through the π-backbonding molecule mechanism. UiO-66 with a Zr/Hf molar ratio of 1:1, denoted as U(0.5Hf), demonstrated much superior adsorption probability and enhanced charge separation and transfer efficiency than UiO-66(Zr) and UiO-66(Hf). This could be ascribed to the difference CB positions between Hf-O cluster and Zr-O cluster, the electron could be transferred from Hf-O cluster to Zr-O cluster. The Hf-O cluster served as the electron mediator

to prolong the electron lifetime, while the Zr-O cluster acted as active sites for nitrogen fixation. In the linkers, the light absorption of all U(0.5Hf) was enhanced after organic linker functionalized. Only U(0.5Hf)-2SH functionalized with two thiol groups in H_2BDC successfully extended the absorption edge from UV to visible light, with an absorption edge at 502 nm. Notably, U(0.5Hf)-2SH showed the best charge separation and transfer efficiency compared to all other samples. This could contribute to the introduction of two thiol groups in the H_2BDC of U(0.5Hf) with best light absorption and utilization could efficiently generate electrons, and then enhance the linker-to-metal-to-metal electron transfer (electrons were first transferred from the linker to the Hf-O cluster, and then to the Zr-O cluster). As a result, under visible light, U(0.5Hf)-2SH displayed the optimal photocatalytic nitrogen fixation performance with an NH_3 generation rate of 116.1 μmol $g^{-1}h^{-1}$ and a superior apparent quantum efficiency of 0.55 % at 420 nm.

Replacing all or part of the metal node Zr with Ce or Ti in the secondary building units of UiO-66 is an effective strategy for adjusting the position of the energy band edges and the band gap, alternating hybridization level between the linker and the metal center and realizing metal-centered electron localization. Future work could revolve around the continued functionalization of the organic linkers with electron-donating functional groups in the case of metal center replacement in UiO-66 to explore whether further LMCT can be facilitated.

3.3. Defect engineering

Structural defects are usually formed along with bond breakage and reformation, lattice distortion and as well as electronic localization at the time of their formation, then causing changes in material properties [93]. Defect engineering is therefore an effective approach to modulate energy bands and electronic structures together with tailored material properties [94-96]. By introducing suitable structural defects into the crystal structure, it is possible to achieve high charge separation efficiency and affluent active sites [97,98]. In addition, the formation of defects on the surface and internal nanopores could also be beneficial for the adsorption [99,100]. For UiO-66, because of the strong chemical bonding of the Zr atom to the oxygen atom and the coordination of a single secondary building block of Zr_6 clusters with 12 H_2BDC (the highest number of organic linkers and metal cluster Zr_6 coordination available in MOFs), making a high tolerance for structural defect tuning [101]. Structural defects are usually formed in response to the missing of organic linkers H_2BDC and Zr_6 clusters in nucleation or post-synthesis process [41,102,103]. It has been revealed that the framework structure of UiO-66 could remain unchanged with the missing of up to 4.3 organic linkers per Zr oxo cluster [104]. Partial substitution of the organic linker H_2BDC is an effective way to modulate the defective structure of UiO-66 [43]. Vos et al. [105] evaluated the effect of missing linker defects on the electronic structure of UiO-66 and discussed their ability to enhance LMCT. The authors found that the nature of the UiO-66 defect structures relied heavily on the coordination of the nodes, and the nodes with the strongest local distortions had the greatest influence on electronic structure. When only one H_2BDC was removed, the unoccupied d orbitals of Zr remained almost unchanged from pure UiO-66(Zr). With the removal of more H_2BDC per node, the energy of d orbitals decreased, resulting in nodes with enhanced charge transfer capabilities and therefore improved the photocatalytic activity. Taddei et al. [106] first prepared UiO-66 with defects using formic acid as the modulator, followed by attaching a series of amino-functionalized benzoic acids onto the defective sites through post-synthetic exchange, which allowed the band gap of UiO-66 to be regulated in the range of 4.1–3.3 eV. DFT calculations suggested that the narrowing of the band gap was mainly caused by a rise in valence band energy due to the availability of light-absorbing monocarboxylates. In another work, Ma et al. [93] used acetic acid as the modulator to synthesize UiO-66-NH_2 with controlled structural defects and systematically explored the influence of structural defects on photocatalytic performance. It was found that the structural defects in UiO-66-NH_2 were missing linker defects and caused by the substitution of acetic acid for the linker. The surface area (705 to 1057 m^2 g^{-1}) and pore volume (0.53 to 0.62 cm^3 g^{-1}) increased with the increased of structural defects. However, all UiO-66-NH_2 engineered with controlled defects showed similar light absorption and band gap (3.0 eV), indicating the light-harvesting ability of UiO-66-NH_2 was hardly affected by the structural defects. Remarkably, in the presence of Pt NPs, all UiO-66-NH_2 engineered with controlled defects exhibited volcanic growth of hydrogen generation activity up to 381.2 μmol $g^{-1}h^{-1}$, far exceeding the negligible activity of UiO-66-NH_2 synthesized without modulator. The ultra-high activity stemmed from the fact that defect engineering in UiO-66-NH_2 could turn on photocatalysis and accelerate effective electron-hole separation, as unambiguously revealed by ultrafast transient absorption spectroscopy. Besides, there was an optimal level of structural defects to promote electron-hole separation, while excessive structural defects deteriorated into recombination centers for electron-hole pairs, leading to a decrease in activity. Fu et al. [107] obtained a series of defective UiO-66-NH_2(Zr) by simply adjusting the crystallization temperature in the presence of hydrochloric acid as the modulator and examined their photocatalytic activity in CO_2 reduction. Compared with the defect-free UiO-66-NH_2, the photocatalytic CO_2 reduction activity of the defective UiO-66-NH_2 were significantly enhanced, and the maximum generation of HCOOH was up to 129.8 μmol $g^{-1}h^{-1}$. This was because defective engineering created a more open framework and active binding sites, which facilitated photogenerated charge transfer. In addition, according to relevant reports, the following approaches to creating structural defects can be considered: (a) the use of $ZrOCl_2{\cdot}8H_2O$ as Zr-precursor rather than $ZrCl_4$, would allow the competition between the organic linker H_2BDC and the coordinated hydroxyl group as well as the coordinated water in $ZrOCl_2{\cdot}8H_2O$, resulting in less coordination of the organic linker to the metal center Zr [81,108]; (b) synthetic conditions without solvent (DMF) could reduce the solubility of the H_2BDC linker, then resulting in inferior coordination between clusters and linkers [108]; and (c) the use of mixed metals node to generate missing Zr_6 clusters, for instance, with the six-coordinated Ti linked to fewer organic linkers compared with the eight-coordinated Zr ions [41,79]. Moreover, cluster defects and linker defects could also be easily introduced in UiO-66 under UV light compared to conventional strategies (synthesis conditions, thermal activation, incorporation of modulators, etc.). Gao et al. [109] firstly introduced photoexcited defects in UiO-66 for effective photocatalytic nitrogen fixation. It was found that the defects were successfully introduced in UiO-66 and were caused by the decomposition of formic acid and acetic acid in fresh UiO-66 under UV light. The band gap of UiO-66 decreased from 3.32 eV to 2.73 eV after light irradiation, suggesting that UiO-66 with defects possessed visible light adsorption ability. The nitrogen photofixation performance of UiO-66 was greatly enhanced after first light irradiation, with an enhancement from 131 to 196 μmol h^{-1} g^{-1} compared to fresh UiO-66. The authors found that charge separation and transfer were not responsible for enhanced performance as confirmed by the electrochemical results, but rather for the defects introduced in UiO-66 after light irradiation. Furthermore, the authors proved that the remarkable improvement in nitrogen photofixation performance was attributed to the metal-unsaturated coordination environment induced by linker defects instead of cluster defects.

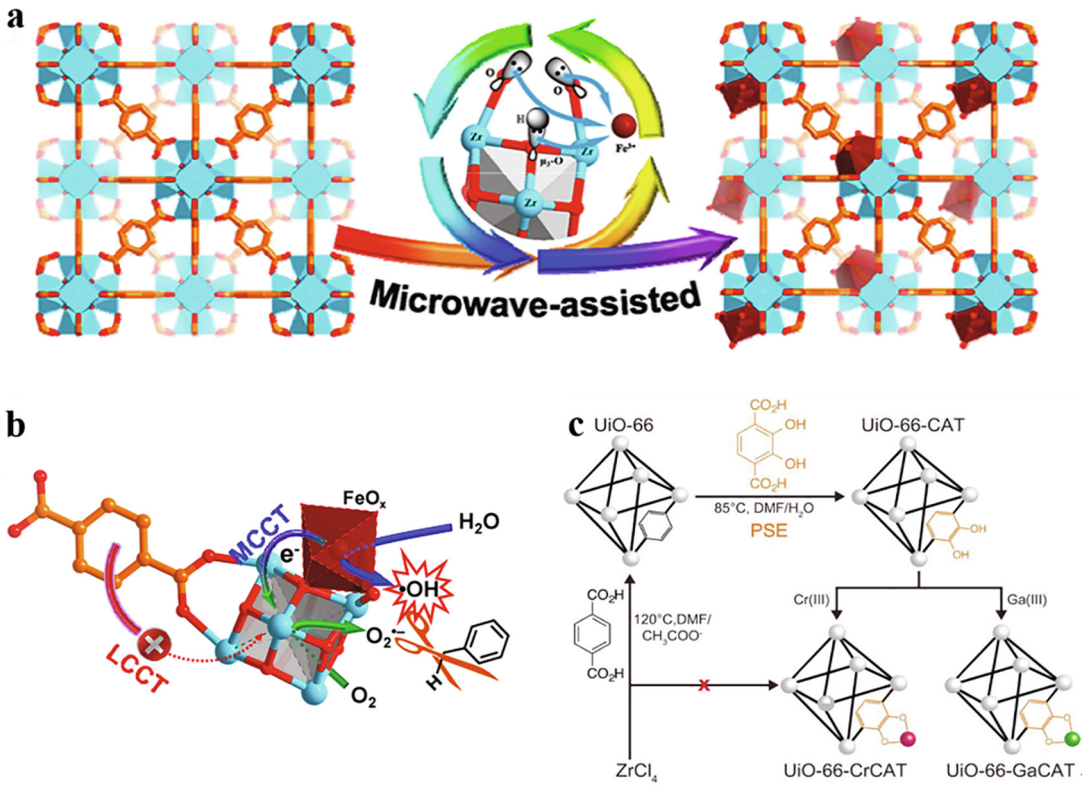

Fig. 3. Schematic illustration showing (a) FeOx attached to the Zr-o cluster via coordination interactions; (b) the pathway for the conversion of H_2O to •OH; (c) the trivalent metal ion (Cr(III) and Ga(III)) attached to the catechol-functionalized organic linker. Adapted with permission from Ref. [114,115], Copyright 2019, American Chemical Society, and Copyright 2015, The Royal Society of Chemistry.

In summary, the creation of structural defects can make the adsorption process easier and supply ample active sites for photocatalytic reaction. However, structural defects in the framework tend to adversely affect the stability due to the reduced density and rigidity of the framework, so controlling reasonable structural defects remains challenging and potentially promising.

3.4. Introduction of foreign metal

3.4.1. Metal ions

The incorporation of metal-to-cluster (MCCT) and metal-to-metal charge transfer (MMCT) by doping inorganic photocatalysts with metals provides an effective technique to extend the range of light absorption and possess appropriate active sites to enhance photocatalytic performance [110,111]. Likewise, metal doped modifications on UiO-66 have achieved a quantum leap in photocatalytic activity enhancement [112,113]. Embodied in, the introduction of foreign metal ion induces MCCT or MMCT to construct bimetallic UiO-66, which can promote effective charge separation and broaden the photoresponse for excellent photocatalytic performance [71,114]. More importantly, the incorporated metal ions are not present in UiO-66 as the metal nodes, but on the surface or chemically bonded to Zr oxo clusters or organic linkers.

For instance, Xu et al. [71] firstly introduced Fe^{3+} onto the UiO-66 surface without destroying the UiO-66 skeleton structure to synthesize FeUiO-66 for the oxidation of alcohols. The addition of Fe^{3+} resulted in a red-shifted absorption edge for FeUiO-66 compared to pure UiO-66. In addition, based on MMCT excitation, electron transfer between Fe and Zr could extend the lifetime of electrons and thus improve the efficiency of photogenerated charge separation. At the same conditions, the photocatalytic conversion of benzyl alcohol was only 10% when using UiO-66 with limited absorption of visible light, where the introduction of Fe increased the conversion to a maximum of 32%. Similarly, by attaching Fe^{3+} to Zr oxo clusters, Xu et al. [114] obtained a strong oxidation-capable Fe-UiO-66 photocatalyst via the microwave-assisted method for photocatalytic C–H bond activation under visible-light irradiation (Fig. 3a). It was found that original octahedral structure of UiO-66 was retained after the incorporation of Fe^{3+}, and there were no additional particles outside or inside of Fe-UiO-66. Also, the incorporated Fe^{3+} ions were attached to the Zr oxo cluster via the Fe-O-Zr connection and about 1.2 Fe atoms present on each Zr oxo cluster in Fe-UiO-66. The successful introduction of Fe^{3+} ions via Fe-O-Zr connection was favorable to the photocatalytic efficiency. The absorption edge of Fe-UiO-66 exhibited a red-shift after Fe^{3+} modification, indicating that the light utilization efficiency of Fe-UiO-66 was enhanced. In the original LMCT, it could induce the formation of an additional MCCT that allowed Fe-UiO-66 to be excited by visible light. Accordingly, when irradiated by visible light, photogenerated electrons could migrate from Fe^{3+} to Zr oxo clusters, resulting in an effective charge separation that facilitated the oxidation reaction of the C–H bond (Fig. 3b). Notably, the incorporated Fe^{3+} ions to Zr oxo cluster were more probable to act as oxidation sites and electron donors instead of electron mediators to enhance charge separation under illumination. The results showed that in contrast to the negligible activity of UiO-66, the toluene oxidation of Fe-UiO-66 was 70.1% within 2 h and 96.9% within 3.5 h under visible light, and the selectivity of benzoic acid was almost complete. Moreover, the reusability of Fe-UiO-66 can be well maintained over at least 5 successive cycles due to the stable immobilization of Fe in the Zr oxo clusters with a low iron leaching rate of only 0.03 wt%.

Different from the former metal ion connection, Lee et al. [115] introduced trivalent metal elements involving Cr(III) and Ga(III)

into catbdc organic linker of catechol-functionalized UiO-66 as robust photocatalysts for CO_2 photoreduction. The LMCT could also occur between the catbdc organic linkers and the metal (Cr and Ga) elements, while catbdc organic linkers were conductive to visible light absorption for UiO-66 (Fig. 3c). Thus, this combined effect allowed UiO-66-M(III) CAT to exhibit good performance for CO_2 photoreduction. Under visible light irradiation for 6 h, UiO-66-CrCAT and UiO-66-GaCAT could generate 51.73 ± 2.64 μmol and 28.78 ± 2.52 μmol of HCOOH with no change in activity over the three cycles, respectively, from the photocatalytic reduction of CO_2. The authors also determined the photocatalytic activity of Fe (III)-metalated UiO-66-CAT. Under the same photocatalytic conditions, UiO-66-FeCAT could only produce a small amount of HCOOH (1.47 μmol) due to the low redox potential of Fe(III). In general, the introduction of oxidation-active metal elements such as Fe into the backbone structure of UiO-66 has demonstrated to be an effective and promising way to achieve modifications that enhance the photocatalytic properties of UiO-66.

3.4.2. Metallic nanoparticles

In recent years, noble-metal nanoparticles (NPs) have grabbed great attention owing to their potential in various applications, especially in the field of catalysis [116]. In photocatalytic reactions, the introduction of noble-metal nanoparticles in MOFs can: (a) serve as visible-light harvesters with enhanced spectral absorption; and (b) serve as electron acceptors and active reaction sites.

Certain noble-metals such as Ag, Cu, when confined into nanometric size particles of the UiO-66, might enhance the photoresponse range through the local surface plasmon resonance (LSPR) effect [117,118]. In particular, the collective oscillation of electrons on metal surfaces confined in nanoscale cages could exhibit a characteristic photoresponse band [37,119]. For example, in the short-wave range, Au@UiO-66-NH_2 exhibited a similar light absorption to UiO-66-NH_2, but an energy band peak at 548 nm appeared for the LSPR of Au [117]. Another function performed by noble-metal NPs is to serve as electron reservoirs and as co-catalysts providing active reaction sites and transferring electrons to the reactants [120]. Under irradiation, the photogenerated electron could be transferred from UiO-66 to noble-metal NPs, resulting in increased lifetime of the photogenerated charge-separated state and enhanced the photogenerated electron-hole separation efficiency. In 2021, Mao et al. [121] reported that Au nanodots encapsulated in the UiO-66-$(SH)_2$ pores not only enhanced the visible light absorption of UiO-66-$(SH)_2$, but also acted as photogenerated electron reservoirs because of the presence of Schottky junctions, which contributed to the high photogenerated electron-hole separation efficiency. Furthermore, the photocatalytic efficiency is closely correlated with the position of noble-metal NPs relative to the MOF. For instance, Pt NPs were successfully introduced into the UiO-66-NH_2 in two different ways (internally and externally as Pt@UiO-66-NH_2 and Pt/UiO-66-NH_2, respectively), and the results showed that all Pt-decorated UiO-66-NH_2 photocatalysts exhibited significantly greater photocatalytic hydrogen generation efficiency compared to the poor activity of UiO-66-NH_2 (1.72 μmol $g^{-1}h^{-1}$) [122]. The authors suggested that this was because the low overpotential Pt was an ideal electron trap to offer redox reaction sites for hydrogen generation, and the photogenerated electrons on the UiO-66-NH_2 were transferred to Pt via the Schottky junction for proton reduction. Strikingly, At the same Pt loading, the photocatalyst with Pt inside the UiO-66-NH_2 (257.38 μmol $g^{-1}h^{-1}$) exhibited approximately 5 times better photocatalytic activity than the external one (50.26 μmol $g^{-1}h^{-1}$). This lied in the fact that the photogenerated electron migration from UiO-66-NH_2 to the internal Pt was much shorter than to the externally loaded Pt, effectively preventing undesired photogenerated charge recombination. In addition, Pt NPs in Pt@UiO-66-NH_2 have better stability and recoverability due to the greater restriction in UiO-66-NH_2, while Pt NPs in Pt/ UiO-66-NH_2 were more likely to aggregate and leach, leading to loss of activity.

Although the introduction of noble-metal NPs has greatly ameliorated the photocatalytic efficiency of UiO-66, the practical application of photocatalysts containing noble-metals still has serious problems, such as their scarcity and high price. It is therefore necessary to develop suitable materials as cheap, efficient and sustainable substitutes to noble-metals as cocatalysts. In addition, as the unique instincts of the noble-metals themselves, further work is required to fulfill the requirements for excellent photocatalytic activity in this area.

3.4.3. Single metal atoms

Actually, only a small fraction of the metal NPs on UiO-66, no matter how finely dispersed they are, can participate in the photocatalytic process as photoactive centers. More often than not, metal NPs of unsuitable size are inherently ineffective for the photocatalytic reaction, or even causing undesirable side reactions, resulting in low atom utilization or low photocatalytic efficiency. In recent years, single-atom catalysts (SAs) have drawn enormous attention for their quantum size effects, unsaturated coordination environments, and unique electronic structure properties [123-134]. Compared with conventional metal NPs, SAs can induce higher levels of atom use and expose plentiful photocatalytic sites, which has been particularly efficacious in enhancing photocatalytic ability. In 2020, Wang et al. [135] successfully anchored Cu single atoms to the UiO-66-NH_2 surface using a photoinduced method to realize efficient photocatalytic reduction of CO_2 to liquid fuels (Fig. 4a-e). Cu SAs species are coordinated to the NH_2 group on UiO-66-NH_2 and subsequently anchored upon visible-light irradiation. The relevant atomic structure characterizations revealed that the Cu atoms were coordinated with two N atoms and anchored at the atomic level by the UiO-66-NH_2 support. Cu SAs/UiO-66-NH_2 and Cu NPs/UiO-66-NH_2 exhibited similar light absorption intensities due to the presence of visible-light harvesting Cu, with a maximum absorption peak at 500 nm, but varied considerably in their photocatalytic activity. The results also showed that the charge transfer and separation efficiency of the Cu SAs/UiO-66-NH_2 was significantly improved and far exceeded that of the corresponding materials. The incorporation of Cu SAs species could lead to the accumulation of photogenerated electrons on Cu SAs/UiO-66-NH_2, thereby facilitating the photoconversion of CO_2 to liquid fuels. Under driven by solar energy, Cu SAs/UiO-66-NH_2 converted CO_2 to methanol and ethanol at rates of 5.33 and 4.22 μmol h^{-1} g^{-1}, respectively, much higher than the pristine UiO-66-NH_2 and Cu NPs/UiO-66-NH_2.

In another case, Ma et al. [136] recently developed MOF supported SAs with a tunable coordination microenvironment for photocatalytic hydrogen generation via a facile microwave-assisted approach. The -O/OH_x groups of Zr oxo cluster in UiO-66-NH_2 supplied the lone-pair electrons and charge balance to anchor single Ni metal species. Subsequently, the coordination environment of single Ni metal species could be flexibly controlled to generate Ni_1 – X/UiO-66-NH_2 (X = S, O and Sox; ox, oxidation) by hydroxylation, sulfidation, or further oxidation. It was found that the single Ni_1 metal atoms were anchored on the neighboring -O/OHx groups from a Zr oxo cluster of UiO-66-NH_2, and the coordination microenvironment of Ni_1 were successfully modulated. UV – vis spectra indicated that all Ni_1 – X/UiO-66-NH_2 did not apparently influence the light absorption ability of UiO-66-NH_2 and possessed a light absorption peak at about 370 nm. The obtained Ni_1 – X/UiO-66-NH_2 featured close proximity to the photosensitive units and highest atomic availability, which facilitated charge transfer. Thus, the performance of Ni_1-X/UiO-66-NH_2 was significantly higher than that of corresponding NiS or Ni NPs

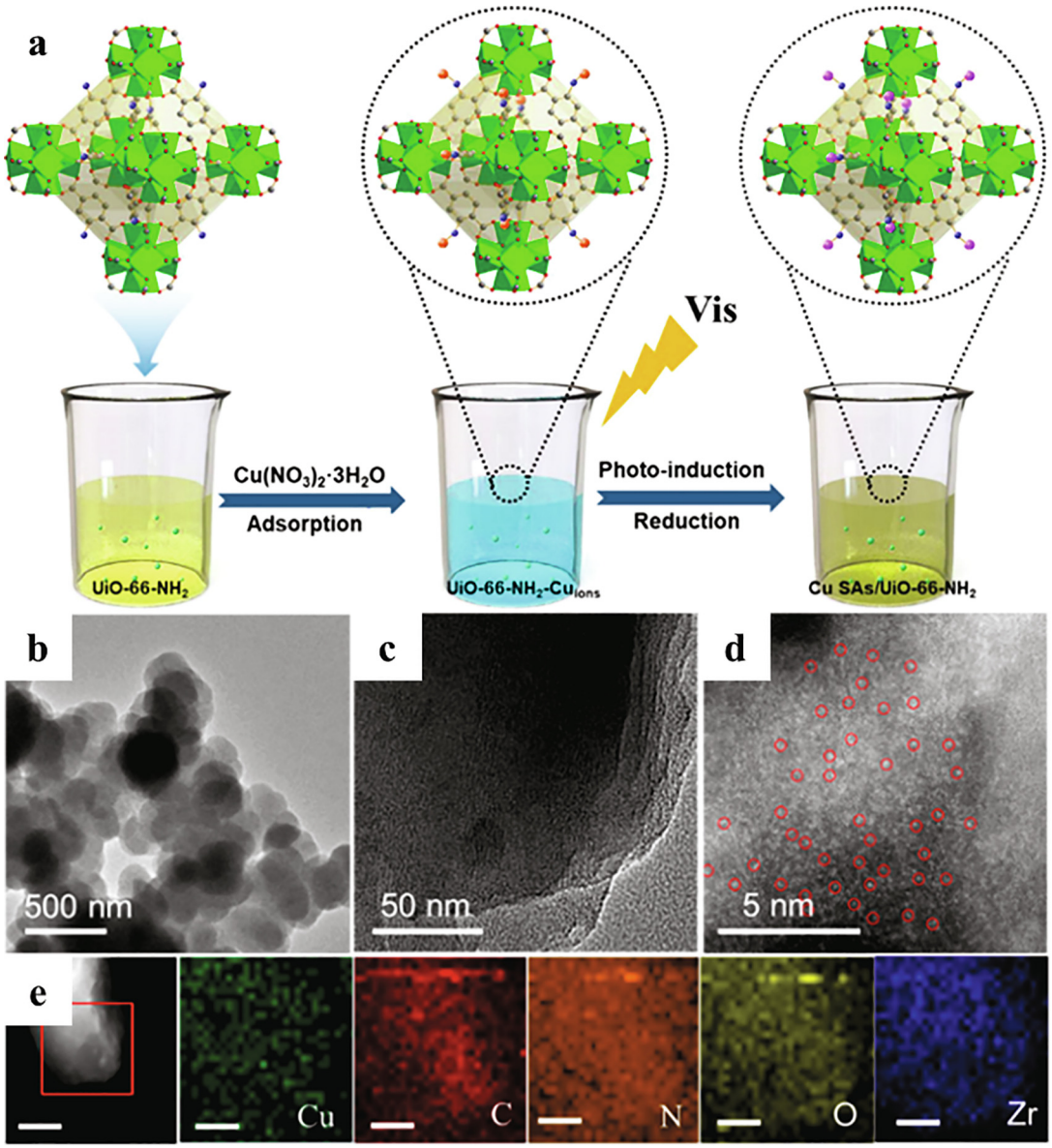

Fig. 4. (a) Synthesis illustration of the Cu SAs/UiO-66-NH_2 photocatalyst. Zr − O clusters, C, O and N atoms, Cu ions, and Cu SAs are represented in green, gray, red, blue, orange, purple; (b) TEM and (c) HRTEM images of Cu SAs/UiO-66-NH_2; (d) Aberration-corrected STEM images of Cu SAs/UiO-66-NH_2. The red circles represent Cu SAs. (e) EDS mapping images of Cu SAs/UiO-66-NH_2. Adapted with permission from Ref. [135], Copyright 2020, American Chemical Society. (For interpretation of the references to colour in this figure legend, the reader is referred to the web version of this article.)

supported by UiO-66-NH_2 in photocatalytic hydrogen generation. Notably, compared to Ni_1-O/UiO-66-NH_2 and Ni_1-Sox/UiO-66-NH_2, the Ni_1-S/UiO-66-NH_2 containing sulfur-coordinated Ni sites exhibited the best photocatalytic hydrogen generation rate of 1360 μmol $g^{-1}h^{-1}$. The superior performance of Ni_1-S/UiO-66-NH_2 could be ascribed to the most appropriate Gibbs free energy values (ΔG_{H^*}= −0.08 eV) of Ni_1-S/UiO-66-NH_2, which suggested the most efficient proton/electron transfer and easier hydrogen molecular release, as confirmed by DFT calculations. Moreover, the stability test indicated that the Ni_1-S/UiO-66-NH_2 was a particularly durable SAs with no decrease in activity after at least six cycles, suggesting the robust bonding between single Ni_1 metal atoms and the support. Most importantly, this facile microwave-assisted sulfidation approach could be successfully extended to other SAs supported by UiO-66-NH_2 to afford M_1-S/UiO-66-NH_2 (M = Co, Cu). The success of these studies demonstrates great potential for optimizing the performance of UiO-66 photocatalysts at the atomic scale.

3.5. Dye sensitization

The construction of dye-sensitized system is a relatively mature approach to modify UiO-66 with visible light harvesting [137,138]. The huge specific surface area of UiO-66 provides potential adsorption sites, making it an excellent support material for dye molecules such as Eosin Y (EY), RhB and Erythrosine B (ErB) etc. Moreover, because of the existence of benzene rings in both dye molecules and organic linkers of UiO-66, strong π-π stacking and van der Waals interactions could occur between them, which could facilitate efficient photogenerated electron transfer from the dye molecules to well-ordered structure UiO-66 in dye sensitization system (Fig. 5a) [139,140]. Yuan et al. [141] prepared the ErB-sensitized octahedron UiO-66 for hydrogen generation, which used Pt as a co-catalyst and L-ascorbic acid as a sacrificial reagent, achieving the highest hydrogen generation rate of 4.6 mol h^{-1} under visible light. The absorption intensity of Pt-UiO-66 in the visible-light region was significantly enhanced after ErB sensitiza-

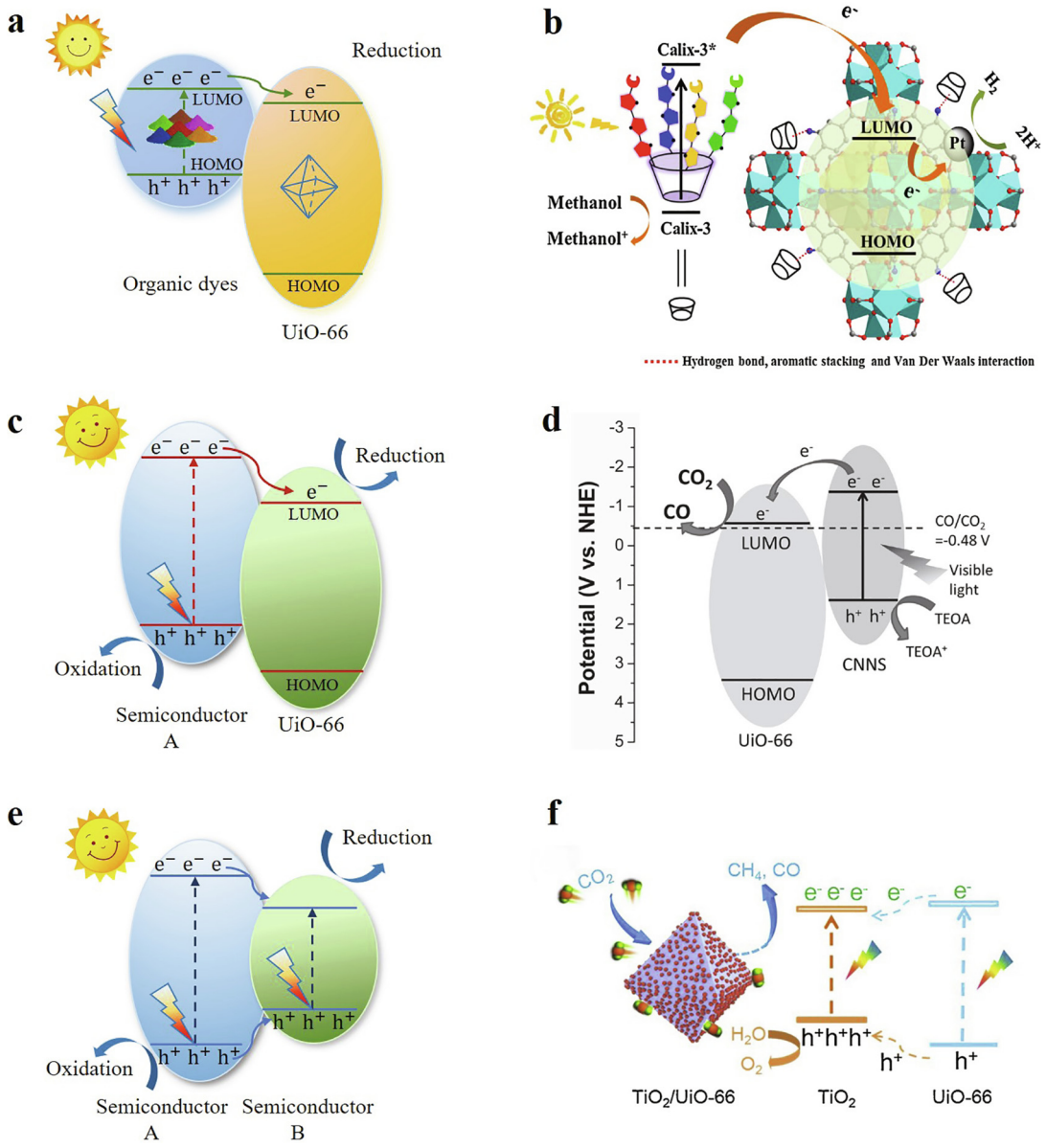

Fig. 5. Schematic illustration of the separation of photogenerated electron–hole pairs over (a) UiO-66 after photosensitization modification under visible-light irradiation; (b) Calix-3 sensitized Pt@UiO-66-NH_2 under visible-light irradiation; (c) UiO-66/semiconductor heterojunction photocatalysts under visible-light irradiation; (d) UiO-66/CNNS photocatalyst under visible-light irradiation; (e) type-II heterojunction photocatalysts; (f) TiO_2/UiO-66 heterogeneous photocatalyst under light (a 300 W xenon light) irradiation. Adapted with permission from Ref. [142,148,156], Copyright 2020 and 2017, Elsevier, Copyright 2015, WILEY-VCH.

tion, and the spectra indicated mixed features of visible-light harvesting ErB dye and UV-light harvesting UiO-66 octahedrons. Unexpectedly, the pristine Pt-UiO-66 sample had no hydrogen generation activity due to its no visible-light harvesting nature, while the ErB-sensitized Pt-UiO-66 achieved hydrogen generation activity. The ErB-sensitized Pt-UiO-66 can be excited under visible light, and the physical interaction force existed between benzene ring in the ErB dye and organic linker H_2BDC, resulting in effective photogenerated electron injection from the excited ErB dye molecule to UiO-66 octahedron for hydrogen generation. However, after three cycles of the photoreaction, the hydrogen generation activity could only be maintained above 80%, which can be attributed to the depletion of the ErB dyes or the instability between the ErB dyes and UiO-66 under prolonged visible light irradiation, resulting in a loss of the photocatalytic activity. Weak physical interactions between dye molecules and UiO-66 often result in little adsorption of dye molecules and instability after adsorption. It may also affect the effective transfer of photogenerated electrons and make dye sensitized photocatalysts less stable and less reusable. For better dye adsorption, Chen et al. [142] successfully established a Calix-3-sensitized (cone-calixarene-based dye) system using UiO-66-NH_2 embedded with Pt NPs for high-efficiency hydrogen generation under visible-light illumination. Four D-π-A units in Calix-3 could be used as active components for light-harvesting to extend the optical absorption of UiO-66-NH_2. Based on the existing van der Waals interactions and π-π stacking, the four carboxyl groups present in each Calix-3 molecule could form hydrogen bonds with the amino group in UiO-66-NH_2. This could allow stable adsorption of Calix-3 molecule and support the efficient transfer of photogenerated electron from the Calix-3 molecule to UiO-66-NH_2 and ultimately to Pt NPs to generate hydrogen (Fig. 5b). The prepared photocatalysts can achieve extremely elevated hydrogen generation activity (1528 μmol $g^{-1}h^{-1}$). Fascinatingly, it can be cycled at least three times with no significant reduction in photocatalytic performance. It is worth noting that the formation of chemical bonds between dye molecules and functional groups in organic

linkers of UiO-66, such as amino groups, is also an effective approach to construct the dye-sensitized system with better photocatalytic properties and stability [143]. For instance, Kumar et al. [143] introduced EY dyes into the amine-functionalized UiO-66-NH_2 through covalent interactions via dehydration coupling reactions between the carboxyl groups in EY and the amine groups in UiO-66-NH_2. The obtained samples acted as robust and green photocatalysts with excellent photocatalytic performance towards activating C–H bond of tertiary amines. Moreover, the photocatalysts can be cycled 10 times with no noticeable drop in activity. Recently, Shi et al. [144] developed EY-sensitized UiO-66-NH_2 for hydrogen generation using a solvothermal method, in which EY was strongly chemically immobilized on UiO-66-NH_2 via a bidentate bridging coordination (Zr ← O – C = O → Zr) between the two O atoms from −COOH group in EY dye molecule and Zr atoms in UiO-66-NH_2. The strong chemical bonds between them resulted in an incremental loading of the EY molecules onto UiO-66-NH_2, extending the photoresponse of UiO-66-NH_2 and accelerating the migration of photogenerated electrons from the EY with visible-light-harvesting to UiO-66-NH_2, resulting in significantly better stability and hydrogen generation activity (2760 μmol $g^{-1}h^{-1}$).

The construction of dye-sensitized UiO-66 has great potential for photocatalysis due to the low cost, green, simplicity of operation and the abundance of properties. In brief, this strategy is favorable for (a) enhancing the visible light absorption of UiO-66; (b) generating the transfer of photogenerated electrons from the dye molecules to UiO-66; and (c) optimizing the adverse environmental impact of dyes. However, stability is still an issue that needs to be carefully considered because of the secondary contamination caused by the desorption of dyes, even though relatively stable dye-sensitized systems have now been constructed.

3.6. Combination of UiO-66 with other semiconductors

The concept of constructing composite photocatalysts from UiO-66 and other photoactive semiconductors for photocatalytic applications provides several potential advantages over single component photocatalysts: (a) the introduced photoactive semiconductors could serve as light harvesting center to increase the solar light utilization ability of UiO-66; (b) the high surface area and permanent porosity of UiO-66 can not only act as the active-sites provider, but also serve as a support to avoid the aggregation of the foreign nanoparticles; and (c) coherent interfacial connections between UiO-66 and the photoactive semiconductors could offer extensive channels for transfer and separation of photogenerated charge.

3.6.1. UiO-66 as cocatalyst for photocatalysis

There is still a part of researches applying the composite of UiO-66 and other photocatalysts for photocatalysis under visible-light illumination. Owing to the inherent inactivity of UiO-66 upon visible light, when combined with other photocatalysts it can only act as cocatalyst to (a) reduce the particle size and preventing the aggregation of other photocatalysts [145]; and (b) provide significant surface area for adsorbents adsorption and active sites for the reaction [146-151]. Specifically, it can accept electrons generated by light-excited semiconductors, and then react with the adsorbed molecules (Fig. 5c). Shi et al. [148] adopted a facile strategy to prepare UiO-66/CNNS (2D atomic carbon nitride nanosheet) photocatalysts through electrostatic self-assembly of positively charged UiO-66 with negatively charged CNNS and they found that this photocatalysts showed efficient conversion of CO_2 to CO (59.4 μmol g^{-1} within 6 h illumination). In the aforementioned composite, CNNS were uniformly covered on the surface of UiO-66 without much aggregation, and there was a coherent and interface between CNNS and UiO-66. Moreover, based on the CO_2 adsorption isotherms and UV–vis absorption spectra, UiO-66/CNNS exhibited a maximum CO_2 uptake of 32.7 cm^3 g^{-1} and enhanced light absorption ability with an absorption edge at about 440 nm by adding CNNS. Meanwhile, electrons from photoexcited CNNS could be injected into UiO-66 due to the formation of nanojunctions in UiO-66/CNNS, which could greatly inhibit the recombination of photogenerated carriers in CNNS and provide sufficiently long-lived electrons for the activation of adsorbed CO_2 in UiO-66 and production of CO (Fig. 5d). Therefore, UiO-66/CNNS achieved markedly enhanced photocatalytic performance toward conversion of CO_2 to CO, which was over 3 times than that of CNNS (17.1 μmol g^{-1}). In addition, employing the virtues of UiO-66 as a cocatalyst, a novel series of UiO-66/$CdIn_2S_4$ nanocomposites for visible light-driven decontamination of triclosan and hydrogen generation has been prepared by Bariki et al. [149]. The prepared nanocomposites with hierarchical flowerlike 3D-microspheres consisted of well-dispersed spherical UiO-66 (20 ∼ 40 nm) immobilized on high aspect ratio $CdIn_2S_4$ nanosheets. Such unique hierarchical microflower structure would offer highly exposed reaction sites and enhance the structural stability. UV–vis DRS indicated that the UiO-66/$CdIn_2S_4$ nanocomposites showed stronger light absorption range (590–640 nm) than UiO-66. PL (photoluminescence) emission spectra confirmed that the intensity of UiO-66/$CdIn_2S_4$ nanocomposites was significantly lower than that of pure UiO-66, which was attributed to the efficient charge carrier separation property between UiO-66 and $CdIn_2S_4$. Also, owing to the constructive band alignment between UiO-66 and $CdIn_2S_4$, the photogenerated electrons could be easily transfer from the CB of $CdIn_2S_4$ (-0.87 eV) to the LUMO of UiO-66 (-0.6 V), which enhanced the photocatalytic performance. The optimal nanocomposites exhibited remarkable photocatalytic efficiency towards triclosan decontamination ((0.0094 min^{-1}) and hydrogen generation (2.95 mmol$g^{-1}h^{-1}$), far stronger than the pure $CdIn_2S_4$ and UiO-66. In another work, such flowerlike 3D-microspheres were also achieved by Liu et al. [152], which UiO-66 were uniformly embedded into $ZnIn_2S_4$ flowerlike microspheres. The introduction of appropriate amount of UiO-66 can significantly improve the migration of electrons from photoexcited $ZnIn_2S_4$ to the surface of photocatalysts and elevate the separation efficiency of photogenerated carriers. Furthermore, the nitrogen adsorption–desorption isotherms indicated the introduction of UiO-66 enhanced the specific surface areas of photocatalysts and facilitated the photocatalytic reaction. As a result, the prepared photocatalysts displayed excellent photocatalytic Cr(VI) reduction activity with a reduction rate of up to 99% after 60 min irradiation, far exceeding either UiO-66 or $ZnIn_2S_4$ alone.

The combination of UiO-66 as a cocatalyst with other high-performance semiconductors not only can compensate for the weak visible light absorption of UiO-66, but can also provide fast migration of the charge carriers and high resistance to recombination by the tight interfacial contacts, making it an effective and simple method to modify UiO-66 for photocatalysis. Meanwhile, this overlooks the potential of UiO-66 to be available under visible light after appropriate modification, and photocatalytic activity can be further enhanced.

3.6.2. UiO-66 as photocatalyst for photocatalysis

From the above, it can be concluded that various approaches have been proposed to improve the photoresponse and charge separation efficiency of UiO-66. Remarkably, engineering heterojunctions in photoresponsive UiO-66 have been demonstrated to be one of the most promising methods for the modification of UiO-66, as it is simple, feasible and effective for the spatial separation of electron-hole pairs. In general, the heterojunction is defined as an interface created by the compounding of two different semicon-

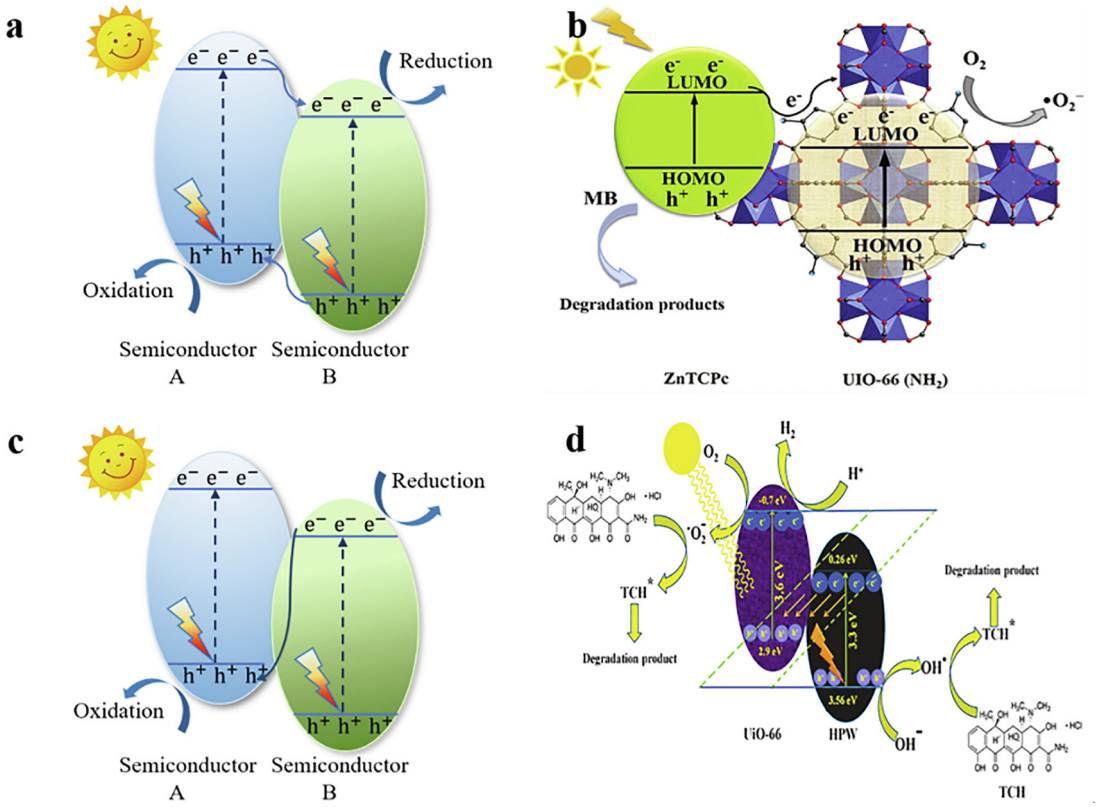

Fig. 6. schematic illustration of the separation of photogenerated electron–hole pairs over (a) type-II heterojunction photocatalysts; (b) MB over the ZnTCPc/UIO-66-NH_2; (c) Z-scheme heterojunction photocatalysts; (d) HPW@UiO-66. Adapted with permission from Ref. [177,183], Copyright 2017, Elsevier and Copyright 2019, American Chemical Society.

ductors with inequitable energy band structure, which may lead to energy band alignment [153,154]. According to current researches on the modification of heterojunctions in UiO-66, three types can be distinguished: straddling gap (type-I) (Fig. 5e), staggered gap (type-II) (Fig. 6a), Z-scheme heterojunction (Fig. 6c) [155]. Ma et al. [156] developed TiO_2/UiO-66 type-I heterojunction photocatalysts by a reflux-solvothermal approach for CO_2 reduction. Transmission electron microscopy (TEM) images revealed that crystalline TiO_2 covered on the smooth surface of UiO-66. The electrostatic repulsion between the positively charged ultrafine TiO_2 NPs on UiO-66 surface ensured fully naked sites and high CO_2 uptake of 78.9 $cm^3\ g^{-1}$ for the hierarchical porous TiO_2/UiO-66. Compared to the UV absorption of pure UiO-66, the TiO_2/UiO-66 presented enhanced light absorption and almost overlapping with TiO_2 due to dominant content of TiO_2 in the composite. Under UV–vis-IR light, the photogenerated electrons and holes in UiO-66 would migrate to TiO_2 because the well-matched band gap. And the conversion of CO_2 to CH_4 and CO took place on the CB of TiO_2 with the highest formation rate of CH_4 and CO achieved 17.9 μmol $g^{-1}h^{-1}$ and 1.9 μmol $g^{-1}h^{-1}$, respectively. Meanwhile, the photogenerated holes accumulated at TiO_2 enabled the oxidation of the adsorbed H_2O molecules to produce O_2 (Fig. 5f). Su et al. [157] prepared $Cd_{0.2}Zn_{0.8}S$@UiO-66-NH_2 type-I heterojunction photocatalysts via a facile solvothermal method for photocatalytic hydrogen generation and CO_2 reduction driven by visible light. The TEM images indicated that the $Cd_{0.2}Zn_{0.8}S$ nanoparticles were well dispersed on UiO-66-NH_2 surface. The UV–vis spectrum of $Cd_{0.2}Zn_{0.8}S$@UiO-66-NH_2 showed longer absorption wavelengths compared to the pristine UiO-66-NH_2. UiO-66-NH_2 alone could not be acted as an effective photocatalyst, with a negligible hydrogen generation rate. With the introduction of $Cd_{0.2}Zn_{0.8}S$, the hydrogen generation performance of UiO-66-NH_2 was significant improved. It was found that the prepared samples exhibited excellent photocatalytic performance due to the efficient electron–hole separation achieved through the type-I heterojunction between the $Cd_{0.2}Zn_{0.8}S$ and the UiO-66-NH_2, as confirmed by PL and photocurrent results. The optimized composite exhibited remarkably enhanced photocatalytic activity towards hydrogen generation (5846.5 μmol $h^{-1}\ g^{-1}$) and the reduction of CO_2 to CH_3OH (6.8 μmol $h^{-1}\ g^{-1}$). No significant decrease in photocatalytic activity of the resultant hybrids after 4 consecutive cycles.

In the type-I heterojunction photocatalyst, the photogenerated electrons and holes will be migrated to the same semiconductor, making impossible to effectively separate charge carriers. In addition, such a charge transfer and separation process allow redox reactions to occur on semiconductors with lower redox potentials, dramatically reducing the redox capacity of type-I heterojunction photocatalysts. However, the charge transfer phenomenon of type-II heterojunction photocatalyst could allow for the spatial separation of charge carriers on both semiconductors, thereby increasing the overall photocatalytic efficiency (Fig. 6a) [158-160]. Recently, enormous efforts have been invested to the construction of type-II heterojunction photocatalysts by combining UiO-66/UiO-66 derivatives with different semiconductors, such as TiO_2 [161-163], metal sulphides [121,157,164-167], covalent organic framework (COF) [168,169], graphitic carbon nitrides (g-C_3N_4) [151,170-172] and others [173-177]. For example, Liang et al. [177] present a facile and effective condensation strategy to develop Zinc phthalocyanine (ZnTCPc)/UiO-66-NH_2 type-II heterojunction photocatalysts, which demonstrated high-performance of methylene blue (MB) degradation under visible light. This high activity could be ascribed to the efficient charge separation and transfer realized through the type-II heterojunction between UiO-66-NH_2 and ZnTCPs through the covalent amide structure. The mechanism for the degradation of MB by ZnTCPc/UiO-66-NH_2 heterostructures was recommended by the authors in

Fig. 6b. In detail, because of the higher LUMO of ZnTCPc than UiO-66-NH_2, the photogenerated electrons could be migrated from the LUMO of ZnTCPc into UiO-66-NH_2 and then O_2 molecules to form superoxide radicals ($\bullet O_2^-$) around the surface of UiO-66-NH_2. Meanwhile, the active substances (photogenerated holes, h^+) generated by UiO-66-NH_2 were migrated and accumulated into the HOMO of ZnTCPc. The formed h^+ and $\bullet O_2^-$ were primarily involved to the degradation process of MB. Additionally, ZnTCPc/UiO-66-NH_2 photocatalyst can maintain excellent stability after 5 recycles. Moreover, morphological modulation of heterojunction photocatalysts is essential for improving the photoactivity of type-II heterojunction photocatalysts. Chen et al. [168] developed UiO-66-NH_2@hydrazone-linked COF (TFPT-DETH) core–shell heterojunction photocatalyst with a type-II heterojunction, the obtained catalyst possessed good photocatalytic performance toward hydrogen generation. UV–vis spectrum of all UiO-66-NH_2@TFPT–DETH observed a slight red-shift compared to UiO-66-NH_2 after the introduction of TFPT–DETH. The electrochemical results revealed that the hetero-framework UiO-66-NH_2@TFPT–DETH featured boosted charge transfer. Beyond the effective electron-hole separation within type-II heterojunction, UiO-66-NH_2@TFPT–DETH possessed a core–shell structure with a large contact interface that can further improve the separation efficiency of electron-hole pairs. The optimal photocatalyst with a suitable shell thickness of approximately 20 nm exhibited a remarkable hydrogen generation activity (7178 μmol $g^{-1}h^{-1}$), which was approximately 3 times higher than that of the pure TFPT-DETH. In addition, the strong covalent bonding formed by the shell-core structure conferred strong photochemical stability to UiO-66-NH_2@TFPT-DETH, resulting in no significant loss of activity within 12 h of light exposure. Furthermore, the introduction of cocatalysts for the construction of ternary heterojunction photocatalysts is beneficial for optimizing the performance of type-II heterojunction photocatalysts. Zhang et al. [171] confined carbon nanodots (CDs) to the pores of UiO-66-NH_2 to construct CDs@UiO-66-NH_2/g-C_3N_4 ternary photocatalysts for hydrogen generation. UiO-66-NH_2 presented angular particles around 200 nm in average size on the surface of sheet-like g-C_3N_4, while CDs with an average size around 0.7 nm were well distributed in CD@UiO-66-NH_2/g-C_3N_4. As regard to other counterpart materials, UV–vis spectrum of CD@UiO-66-NH_2/g-C_3N_4 exhibited a significant red-shift with the absorption region extending to 800 nm. The electrochemical measurements indicated the separation of photogenerated charges efficiency of CD@UiO-66-NH_2/g-C_3N_4 was considerably improved by constructing heterojunction and incorporating CDs. The type-II heterojunction significantly promoted the electron–hole separation efficiency between the UiO-66-NH_2 and the g-C_3N_4. Importantly, the introduced ultrasmall CDs extensively enhanced the photocatalytic hydrogen generation activity of the nanocomposites under visible light irradiation. This was because the ultra-small CDs in the UiO-66-NH_2 not only enhanced the light-harvesting ability of this nanocomposites, but acted as an effective cocatalyst to receive photogenerated electrons from the CB of UiO-66-NH_2 for hydrogen generation. Subsequently, the CD@UiO-66-NH_2/g-C_3N_4 achieved an excellent hydrogen generation rate of up to 2.930 mmol $g^{-1}h^{-1}$, which was 38.6, 32.4 and 17.5 times better than that of UiO-66-NH_2, g-C_3N_4 and UiO-66-NH_2/g-C_3N_4, respectively.

In general, type-II heterojunction photocatalysts demonstrate a broad photoresponse range, favorable electron-hole separation and fast charge transfer rates. Nevertheless, though type-II heterojunction photocatalysts have received extensive research with such mentioned advantages, there are still some challenges that may limit their practical application: (a) the migration of photogenerated electrons and holes to lower CB and VB on the semiconductor, respectively, greatly limiting the redox capability; (b) the isotropic migration of electrons/holes from high VB/CB to low VB/CB would be physically hindered by the mutual repulsion of identical charges, respectively [155].

Fortunately, in 1979, Bard et al. [178] first developed the Z-scheme charge transfer mechanism to address these challenges. The charge transfer mechanism of Z-scheme heterojunction photocatalyst is quite distinct from type-II heterojunction (Fig. 6c) [179]. In this way, compared to the other heterojunction photocatalysts, Z-scheme heterojunction photocatalysts also achieve high charge separation efficiency, but without any loss of its own strong redox capacity. Furthermore, owing to the electrostatic attraction between photogenerated charges of different electronegativity, the transfer of charge carriers will become easier and more physically rational. Accordingly, the design of Z-scheme heterojunction photocatalysts have drawn considerable interest in recent years, also over UiO-66 [77,180-185]. For instance, Subudhi et al. [183] designed phosphotungstic acid (HPW)@UiO-66 via a hydrothermal method for H_2 evolution and photodegradation of tetracycline hydrochloride (TCH). Under solar-light irradiation, 30 wt% HPW@UiO-66 showed a maximum degradation rate of 87.24% for TCH, and a hydrogen generation of about 353.89 μmol/h. The charge transfer way in HPW@UiO-66 was consistent with Z-scheme heterojunction rather than type-II, which can be explained for the following reasons: (a) the PL result demonstrated the quick recombination of photogenerated electron-hole pairs; (2) the photogenerated electron at the low VB (0.26 eV) of HPW in type-II heterojunction was not available to react with O_2 to generate $\bullet O_2^-$ ($O_2/\bullet O_2^-$ = −0.33 eV vs normal hydrogen electrode (NHE)), but the fact that $\bullet O_2^-$ was the active agents participating in TCH photodegradation has been confirmed by the scavenger test. Therefore, the mechanism of Z-scheme can be able to more closely delineate the charge transfer route of the degradation process (Fig. 6d). Moreover, the construction of hierarchical microarchitectures can further facilitate the electron–hole separation of Z-scheme heterojunction photocatalysts. Mu et al. [77] introduced MoS_2 nanosheets in Z-scheme UiO-66-$(COOH)_2$/$ZnIn_2S_4$ to construct novel efficient photocatalysts with 3D hierarchical microarchitectures for hydrogen generation and Cr(VI) reduction. It was found that after a one-step hydrothermal treatment, MoS_2 nanosheets and $ZnIn_2S_4$ with flower-like microspheres were closely contacted, and UiO-66-$(COOH)_2$ nanoparticles were decorated on $ZnIn_2S_4$ nanosheets. The formed hierarchical microarchitecture in UiO-66-$(COOH)_2$/$ZnIn_2S_4$/MoS_2 provided an improved surface area to contact reactants, as revealed by N_2 adsorption–desorption. UV–vis DRS suggested that UiO-66-$(COOH)_2$/$ZnIn_2S_4$/MoS_2 showed an intense light response enabling improved solar energy utilization. Noticeably, PL spectra consistently suggested that UiO-66-$(COOH)_2$/$ZnIn_2S_4$ showed a weaker emission profile than pristine $ZnIn_2S_4$, indicating a rapid charge transfer in UiO-66-$(COOH)_2$/$ZnIn_2S_4$. Furthermore, the PL emission profile of UiO-66-$(COOH)_2$/$ZnIn_2S_4$/MoS_2 decreased significantly after the introduction of MoS_2, demonstrating that MoS_2 could further effectively enhance the transport properties of photogenerated electrons. The tight interfacial interactions between UiO-66-$(COOH)_2$, MoS_2 and $ZnIn_2S_4$ can provide highly exposed photocatalytic active sites and further promote electron-hole separation through Z-scheme mechanism, thereby enhancing photocatalytic performance. Attractively, under simulated solar irradiation, the optimized photocatalyst demonstrated highly efficient hydrogen generation (18.794 mmol h^{-1} g^{-1}) and Cr(VI) reduction (0.06850 min^{-1}), about 15.3 and 6.7 times higher than that of pristine $ZnIn_2S_4$, respectively.

The construction of heterojunctions is the most effective and straightforward way to enhance photocatalytic performance. This can not only avoid the disadvantage of inefficient electron-hole separation suffered by the single component, but also create a synergistic effect that greatly enhances the photocatalytic performance. Based on this, future research could

Table 2
Summary of photocatalytic reactions on CO_2 reduction, hydrogen generation organic pollutants removal and Cr(VI) reduction using various modified UiO-66 photocatalysts.[a]

Photocatalysts	BET	Band gap	Reaction	Photoactivity	Reaction conditions	Recycled times	Ref.
NH_2-UiO-66	778 m^2g^{-1}	N/A	The conversion of CO_2 to $HCOO^-$	1.32 μmol h^{-1}	50 mg of photocatalyst, 60 mL of MeCN and TEOA (5/1 v/v), 500 W Xe lamp, 800 nm > λ > 420 nm	one	[54]
mixed NH_2-UiO-66	734 m^2g^{-1}	N/A		2.07 μmol h^{-1}		N/A	[54]
TiO_2/UiO-66	452 m^2 g^{-1}	3.32 eV	The conversion of CO_2 to CH_4	17.9 μmol $g^{-1}h^{-1}$	50 mg of photocatalyst, H_2O as electron donors, 300 W Xe lamp	Five	[156]
TiO_2/NH_2-UiO-66	202 m^2 g^{-1}	3.20 eV (TiO_2); 2.70 eV (UiO-66-NH_2)	The conversion of CO_2 to CO	4.24 μmol $g^{-1}h^{-1}$	3 mg of photocatalyst, H_2 as sacrificial agents, 150 W Xe arc lamp, λ > 325 nm	Three	[161]
CTU/0.6TiO_2	177 m^2 g^{-1}	2.59 eV	The conversion of CO_2 to CO, CH_4	31.32 μmol $g^{-1}h^{-1}$ (CO), 0.148 μmol $g^{-1}h^{-1}$ (CH_4)	100 mg of photocatalyst, 2 mL of distilled H_2O, 300 W Xe lampλ > 300 nm	Four	[163]
O-ZnO/rGO/ UiO-66-NH_2	877.3 m^2 g^{-1}	2.98 eV (O-ZnO) 2.82 eV (UiO-66-NH_2)	The conversion of CO_2 to CH_3OH and HCOOH	34.83 μmol $g^{-1}h^{-1}$ (CH_3OH), 6.41 μmol $g^{-1}h^{-1}$ (HCOOH)	100 mg of photocatalyst, 100 mL of $NaHCO_3$ aqueous solution (0.1 mol/L), 300 W Xe lamp, λ > 420 nm	Six	[185]
UiO-66-NH_2/2 wt% CNTs	642.5 m^2 g^{-1}	N/A	The conversion of CO_2 to HCOOH	28.8 μmol within 4 h of illumination	N/A 5 mL of TEOA and 3 mL of H_2O, 500 W Xe lamp, λ > 400 nm	Six	[204]
UiO-66-NH_2/2 wt% GR	791.2 m^2 g^{-1}	2.64 eV	The conversion of CO_2 to HCOOH	35.5 μmol within 4 h of illumination	20 mg of photocatalyst, 40 mL of DMF, 5 mL of TEOA and 3 mL of H_2O, 300 W Xe lamp, λ > 410 nm	Eight	[176]
NUZ/HGN-35%	335 m^2 g^{-1}	2.58 eV (NUZ) 2.10 eV (HGN)	The conversion of CO_2 to CO	31.6 μmol $g^{-1}h^{-1}$	10 mg of photocatalyst, 1 mL of TEOA and 20 mL of H_2O, 300 W Xe arc lamp, λ > 400 nm	Five	[181]
Cu SAs/UiO-66-NH_2	856.5 m^2 g^{-1}	N/A	The conversion of CO_2 to CH_3OH and C_2H_5OH	5.33 μmol $g^{-1}h^{-1}$ (CH_3OH), 4.22 μmol $g^{-1}h^{-1}$ (C_2H_5OH)	0.1 g of photocatalyst, 50 mL of H_2O and 0.1 mL of TEOA, 300 W Xe lamp, λ > 400 nm	Four	[135]
UiO-66	N/A	N/A	Hydrogen generation	2.4 mL within 3 h (Pt as cocatylst)	45 mg of photocatalyst, 22.5 mL of water and methanol (3/1 v/v), 200 W Xe-doped Hg lamp	~	[29]
UiO-66-NH_2	N/A	N/A	Hydrogen generation	4.5 mL within 3 h (Pt as cocatylst)		~	[29]
Pt@UiO-66-NH_2	867 m^2 g^{-1}	N/A	Hydrogen generation	257.38 μmol $g^{-1}h^{-1}$	10 mg of photocatalyst, 18 mL of acetonitrile, 0.2 mL of H_2O and 2 mL of TEOA, 300 W Xe lamp, λ > 380 nm	Four	[122]
Pt/UiO-66-NH_2	879 m^2 g^{-1}	N/A	Hydrogen generation	50.26 μmol $g^{-1}h^{-1}$		Four	[122]
GOWPt@U6N-8 mL	N/A	N/A	Hydrogen generation	18.15 mmol $g^{-1}h^{-1}$	10 mg of photocatalyst, 0.05 g of Erythrosiner B, 0.5 mL of TEOA and 100 mL of MeCN, 300 W Xe lamp, λ > 420 nm	Six	[217]
Pt@UiO-66-NH_2-100	948 m^2 g^{-1}	3.02 eV	Hydrogen generation	381.2 μmol $g^{-1}h^{-1}$	10 mg of photocatalyst, 27 mL of acetonitrile, 0.5 mL of H_2O and 2.5 mL of TEOA, 300 W Xe lamp, λ > 400 nm	Ten	[93]
UiO-66@$ZnIn_2S_4$	N/A	2.59 eV	Hydrogen generation	3061.61 μmol $g^{-1}h^{-1}$	40 mg of photocatalyst, 85 mL of H_2O and 15 mL of TEOA and 85 mL of H_2O, 300 W Xe lamp, λ > 400 nm	Four	[167]
CdS/UiO-66(10)	N/A	2.4 eV (CdS) 4.1 eV (UiO-66)	Hydrogen generation	1725 μmol $g^{-1}h^{-1}$	16 mg of photocatalyst, 31 mL of 27:3:1 MeCN/ lactic acid/H_2O, 300 W Xe lamp, λ > 380 nm	Three	[67]
MoS_2/UiO-66/CdS	407.63 m^2 g^{-1}	N/A	Hydrogen generation	650 μmol h^{-1}	20 mg of photocatalyst, 80 mL of aqueous solution containing 10% of lactic acid, 300 W Xe lamp, λ > 420 nm	Four	[218]
UiOS-CdS0.7	447.2 m^2 g^{-1}	2.98 eV (UiO-66-$(SH)_2$)	Hydrogen generation	15.32 mmol $g^{-1}h^{-1}$	10 mg of photocatalyst, 20 mL of aqueous solution with 0.35 mol/L $Na_2SO_3{\cdot}9H_2O$ and 0.25 mol/L Na_2SO_3, 225 W Xe lamp, 780 nm > λ > 420 nm	Four	[78]
TCPP@UiO-66(25%)	1002 m^2 g^{-1}	N/A	DF degradation	99 % in 4 h	5 mg of photocatalyst, 50 mL of DF solution 350 W Xe lamp, 200 nm ≤ λ ≤ 1200 nm	Four	[43]
CoUiO-1 (Zr: Co mole ratio = 1)	815.18 m^2 g^{-1}	~3.64 eV	TC degradation	94 %	20 mg of photocatalyst, 100 mL of TC solution (20 mg L^{-1}), 300 W Xe lamp	Four	[228]
Ag_2CO_3/UiO-66	522 m^2 g^{-1}	N/A	Rh B degradation	Mostly removed in 2 h	15 mg of photocatalyst, 30 mL RhB aqueous solution (0.03 mM), 500 W halogen lamp,	Four	[227]
g-C_3N_4/UiO-66 (solvothermal reaction)	1133 m^2 g^{-1}	3.79 eV	Rh B degradation	0.00899 min^{-1}	20 mg of photocatalyst, 50 mL of RhB solution (10 ppm), 500 W Xe lamp, 420 nm < λ < 760 nm	Four	[151]
g-C_3N_4/UiO-66 (anneal)	384 m^2 g^{-1}	2.72 eV	MB degradation	about 100 % in 4 h	50 mg of photocatalyst, 200 mL of MB solution (10 mg L^{-1}), 350 W Xe lamp, 420 nm < λ < 780 nm	Five	[172]

(continued on next page)

Table 2 (*continued*)

Photocatalysts	BET	Band gap	Reaction	Photoactivity	Reaction conditions	Recycled times	Ref.
UiO-66@ZnO/graphene oxide	626.55 m^2 g^{-1}	2.3 eV	TC and malathion degradation	81% (TC) and 100% (malathion) in 90 min	20 mg of photocatalyst,50 mL of pollutant solution (20 mg/L), 500 W Hg lamp, λ > 400 nm	Four	[184]
BiOBr/UiO-66	N/A	2.80 eV	Atrazine degradation	about 88% in 4 h	25 mg of photocatalyst,50 mL of atrazine solution (5 mg/L), 300 W Xe lamp, λ > 400 nm	Four	[232]
S-TiO_2/UiO-66-NH_2	167.17 m^2 g^{-1}	2.75 eV	Cr(VI) reduction	94.9 % in 45 min	10 mg of photocatalyst, 50 mL of $K_2Cr_2O_7$ solution (5 mg L^{-1} Cr(VI)), 50 mW LED lamp	Four	[162]
g-C_3N_4/UiO-66	434 m^2 g^{-1}	~2.78 eV	Cr(VI) reduction	99 % in 40 min	100.0 mg of photocatalyst, 200 mL of $K_2Cr_2O_7$ solution (10 mg L^{-1} Cr(VI)), 300 W Xe lamp	Six	[182]
U-OCl-Ti	462 m^2 g^{-1}	2.64 eV	Cr(VI) reduction	N/A	40 mg of photocatalyst, 40 mL of Cr(VI) solution (50 ppm), 300 W Xe lamp	Two	[81]
UiO − OCl − N	N/A	N/A	Cr(VI) reduction	89.4 % in 3 h	40 mg of photocatalyst, 40 mL of Cr(VI) solution (50 ppm) , 300 W Xe lamp	Three	[108]
UiO-66-NH_2 membrane	N/A	N/A	Cr(VI) reduction	>98.0% in 2 h	20 mg of photocatalyst, 30 mL of Cr(VI) (5 ppm), 300 W Xe lamp, λ > 400 nm	Twenty	[243]
AgCO@UiO/GO membrane	N/A	N/A	Cr(VI) reduction, MB degradation	almost 100%	20 mg of photocatalyst, 100 mL of Cr(VI) (10 mg/L) of 100 mL of MB (20 mg / L) , 500 W Xe arc lamp	Four	[180]

[a] Abbreviations: BET = Brunauer − Emmett − Teller specific surface area; MeCN = methyl cyanide; TEOA = triethanolamine; NA = not available; O-ZnO/rGO/UiO-66-NH_2 = Oxygen-defective ZnO/reduced graphene oxide/UiO-66-NH_2; GR = graphene; CNTs = carbon nanotubes; DMF = N,N-dimethylformamide; NUZ/HGN-35%=UiO-66-NH_2/g-C_3N_4-35%; SAs = single-atom catalysts; GOWPt@U6N = graphene-wrapped Pt@UiO-66-NH_2; UiOS-CdS0.7 = UiO-66-(S-CdS)$_2$ with 70 wt% of $Cd(NO_3)_2{\cdot}4H_2O$; TCPP = tetrakis (4-carboxyphenyl) porphyrin; DF = diclofenac; TC = tetracycline; Rh B = rhodamine b; MB = methylene blue; LED = light emitting diode; U-OCl-Ti = $ZrOCl_2{\cdot}8H_2O$-based UiO-66 with Ti substitution; UiO-OCl-N = $ZrOCl_2{\cdot}8H_2O$-based nonsolvent-assisted UiO-66; AgCO@UiO/GO = Ag_2CO_3@UiO-66NH_2/graphene oxide.

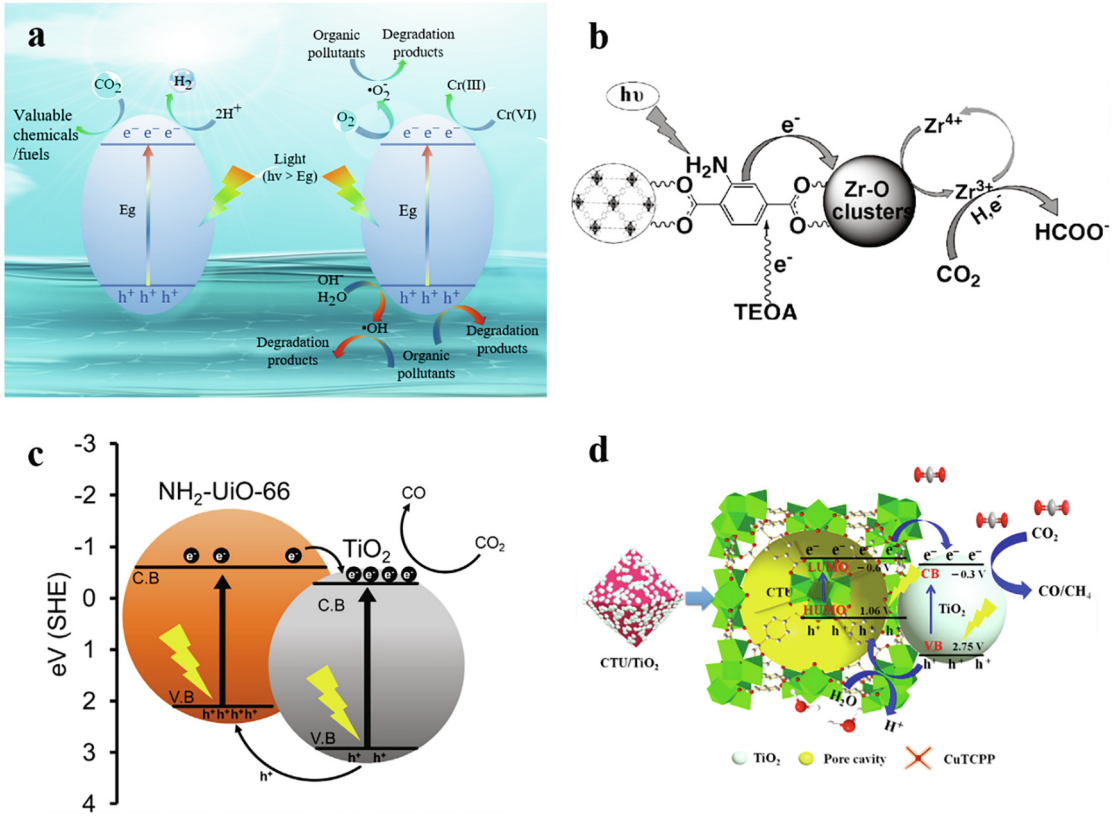

Fig. 7. Schematic illustration of (a) the mechanism for photocatalytic reaction about CO_2 reduction, hydrogen production, removal of organic pollutants, and Cr(VI) reduction over UiO-66-based photocatalyst; (b) the proposed mechanism for photocatalytic CO_2 over NH_2-UiO-66 under visible-light irradiation; (c) the proposed mechanism for photocatalytic CO_2 over TiO_2/UiO-66-NH_2 heterojunctions; (d) the proposed mechanism for photocatalytic CO_2 over CTU/TiO_2. Adapted with permission from Ref. [54,161,163], Copyright 2017 and 2019, Elsevier, Copyright 2013, WILEY-VCH.

focus on the preparation of other high-performance semiconductor@UiO-66 heterojunction photocatalysts by taking the advantages of UiO-66. In addition, the rational design of heterojunction photocatalysts with efficient structures is still necessary. For instance, the formation of strong chemical binding interactions between the individual components of the heterojunction could be an interesting topic for future research, which could not only further enhance the electron-hole separation efficiency but also benefit the stability of the composites. More importantly, further systematic studies are also needed to directly reveal the actual transport routes of electron-hole pairs at the heterojunction interface.

4. Photocatalytic applications of modified UiO-66

Decreasing society's dependence on fossil fuels and alleviating the environmental hazards of industrialization are among the most urgent energy and environmental challenges we face today [186,187]. Modified UiO-66 possess superb water stability, high photostability, fast photogenerated charge separation and migration rate, making these materials to be the ideal photocatalysts for boosting the carbon–neutral energy cycle and solving environmental remediation issues. In this section, modified UiO-66 photocatalysts in the field of photocatalysis related to CO_2 reduction, hydrogen generation, environmental remediation (removal of organic pollutants, Cr(VI) reduction and so on) are introduced (Table 2). The main steps in the photocatalytic process over the modified UiO-66 photocatalysts are illustrated in Fig. 7a: (a) the adsorption of CO_2, protons, organic pollutants and Cr(VI) by the porous modified UiO-66; (b) the absorption of light photons by the modified UiO-66 photocatalyst to generate electron-hole pairs; (c) the separation and migration of these photogenerated charge carriers (Eq. (1)); and (d) the reduction of the adsorbed CO_2 to valuable chemicals/fuels (Eq. (2)), protons to H_2 (Eq. (3)), and Cr(VI) to Cr(III) (Eq. (8) and (9)) by photogenerated electron at the CB, and the oxidation of organic pollutants to harmless degradation products by photogenerated hole, $\bullet O_2^-$ and hydroxyl radical (•OH) (Eq. (7)) [188,189]. And $\bullet O_2^-$ are obtained from the reduction of oxygen by photogenerated electrons (Eq. (4)), while •OH might be generated by the reaction of photogenerated holes with OH^- or H_2O (Eq. (5) and (6)).

$$\text{UiO - 66 - based photocatalysts} \xrightarrow{hv} e^- + h^+ \quad (1)$$

$$CO_2 + e^- \rightarrow \text{valuable chemicals/fuels (CO, } CH_4, \text{ COOH, } CH_3OH \text{ and so on)} \quad (2)$$

$$2H^+ + 2e^- \rightarrow H_2 \quad (3)$$

$$O_2 + e^- \rightarrow \cdot O_2^- \quad (4)$$

$$h^+ + OH^- \rightarrow \cdot OH \quad (5)$$

$$h^+ + 2H_2O \rightarrow 2 \cdot OH + H^+ \quad (6)$$

$$\text{Organic pollutants} + \cdot OH, \cdot O_2^- \text{ or } h^+ \rightarrow \text{Degradation products} \quad (7)$$

$$Cr_2O_7^{2-} + 14H^+ + 6e^- \rightarrow 2Cr^{3+} + 7H_2O \quad (8)$$

$$CrO_4^{2-} + 4H_2O + 3e^- \rightarrow Cr(OH)_3 + 5OH^- \quad (9)$$

4.1. Boosting the carbon–neutral energy cycle

Society's ongoing dependence on fossil fuels and the growing energy demand make the emission of carbon dioxide into the atmosphere a serious global problem [190-193]. Carbon dioxide, methane and hydrogen are thought to be at the heart of a possible solution to this problem by achieving a carbon–neutral energy cycle [194]. Specifically, this problem could be potentially addressed through the deployment of CO_2 capture and storage, methane as a transitional fuel and hydrogen as a long-term fuel. Absolutely, in this energy cycle, other available carbonaceous fuels are also available as alternatives to fossil fuels [195,196].

4.1.1. CO_2 reduction

As part of CO_2 capture and storage step, UiO-66 could be employed as an CO_2 solid adsorbent by virtue of its capacity to adsorb CO_2 at room temperature with low energy requirements [197-199]. Besides, in accordance with the deployment of sustainable development and the transitional fuels, the conversion of CO_2 into valuable chemicals/fuels (such as CH_4, CO, HCOOH and so on) through artificial photosynthesis has grabbed extensive attention [200-203]. By virtue of its porous nature and its modified photocatalytic properties, UiO-66 can achieve both adsorption and conversion of CO_2. For instance, by complete replacement of the organic linker H_2BDC over UiO-66 with H_2ATA, Sun et al. [54] developed UiO-66-NH_2 with visible-light response toward the conversion of CO_2 to $HCOO^-$. The presence of the –NH_2 groups were beneficial for the adsorption of CO_2 by MOF. At 1 atm and 273 K, the maximum CO_2 adsorption of UiO-66-NH_2 was 68 $cm^3\ g^{-1}$, higher than UiO-66 (53 $cm^3\ g^{-1}$). The yield of $HCOO^-$ over NH_2-UiO-66 reached 13.2 μmol in 10 h, however, UiO-66 exhibited negligible ability for CO_2 conversion, and this could be contributed to visible-light harvesting of the H_2ATA linker and photogenerated electrons injection from H_2ATA to Zr oxo clusters in UiO-66-NH_2 (Fig. 7b). The authors confirmed the stability of UiO-66-NH_2 with no significant change in structure after the reaction. The prolonged photocatalytic reaction showed a steady increase in $HCOO^-$ production over 24 h, which further supported the stability of UiO-66-NH_2 during photocatalytic reaction. Furthermore, the authors partially replaced the H_2ATA over UiO-66-NH_2 with 2,5-diaminoterephthalic acid to prepare mixed UiO-66-NH_2, which demonstrated a further enhanced visible-light response and greater adsorption of CO_2 with the second NH_2 groups. As expected, under the identical conditions, the mixed UiO-66-NH_2 produced 20.7 mmol of $HCOO^-$ in 10 h, exceeding by>50% compared to UiO-66-NH_2 (13.2 mmol). The mixed UiO-66-NH_2 produced 7.28 mmol $HCOO^-$ under irradiation at wavelengths>515 nm, while no $HCOO^-$ was detected for UiO-66-NH_2 under irradiation in this spectral region. This work confirmed that amine-functionalized UiO-66 can exhibit CO_2 photocatalytic reduction activity by the introduction of aromatic molecules with NH_2 groups in the organic linker.

Loading semiconductor materials onto the UiO-66 surface to form heterojunctions is an effective and facile approach to boost photocatalytic properties by preventing the aggregation of semiconductor materials to more exposed active sites [165]. For instance, Ma et al. [156] developed TiO_2/UiO-66 heterostructures as efficient photocatalysts for CO_2 conversion by assembling TiO_2 nanoparticles on UiO-66. The TiO_2/UiO-66 with adding 10 mg UiO-66 showed significantly higher specific surface area (452 m^2/g) than TiO_2 (213 m^2/g) as a consequence of loading of UiO-66 (1268 m^2/g). Additionally, the TiO_2/UiO-66 heterostructures fully maintained the light absorption ability of TiO_2 without shielding by UiO-66 incorporation, and possessed the similar bandgap energy of 3.32 eV to TiO_2. Using water as proton donors, the TiO_2/UiO-66 heterostructures with adding 10 mg UiO-66 reached the best CH_4 formation rate of 17.9 μmol $g^{-1}h^{-1}$ and photocatalytic selectivity of 90.4 %. Under light irradiation, the exposed UiO-66 and the outer layers of TiO_2 could readily absorb photons to generate electron-hole pairs, and the photogenerated electron-hole pairs will be separated according to the type-I heterojunction charge transfer due to the well-matched band gap (Fig. 5f). The photogenerated electrons reduced the adsorbed CO_2 to generate CH_4, while the holes reacted with surface H_2O to produce O_2. However, the authors found that the enhanced photocatalytic activity was not primarily accomplished by efficient internal photogenerated charge transfer and separation, which can be principally contributed to valid enrichment of CO_2 molecules in the exposed active sites, and particularly noticeable in diluted condition. Moreover, the TiO_2/UiO-66 heterostructures exhibited good stability

during 5 cycling tests due to the strong interfacial interaction between UiO-66 and TiO_2 preserving the composite structure. Photocatalytic activity is not proportional to the CO_2 molecules' adsorption capacity, which has an optimum percentage of loading. Using as-prepared UiO-66-NH_2 and TiO_2 nanosheets, Crake et al. [161] constructed novel TiO_2/UiO-66-NH_2 photocatalysts for adsorption and conversion of CO_2. Under UV–vis irradiation, the as-prepared photocatalysts containing 25 wt% UiO-66-NH_2 exhibited the greatest photocatalytic ability toward conversion of CO_2 to CO (4.24 μmol $g^{-1}h^{-1}$), and containing 37 wt% UiO-66-NH_2 possessed the maximum CO_2 molecules uptake capacity (0.56 mmol g^{-1}). This result can be explained by the following possible reasons: (a) the appropriate UiO-66-NH_2 content acted as the support to provide suitable porosity for CO_2 adsorption and prevent TiO_2 nanoparticles from aggregating to more exposed active sites, but excess UiO-66-NH_2 would make it contain small amounts of photoactive TiO_2, resulting in reduced photocatalytic ability; (b) the formation of TiO_2/UiO-66-NH_2 heterojunctions can accelerate charge transfer and avoid the recombination of charge carriers, and yet excess UiO-66-NH_2 may diminish the number of heterointerfaces in TiO_2/UiO-66-NH_2 nanohybrids (Fig. 7c). The type-II heterojunction charge transfer (Fig. 7c) allowed quick migration of photogenerated electrons from the UiO-66-NH_2 CB to the TiO_2 CB and holes to the opposite direction. Subsequently, CO_2 were photocatalytically reduced to CO by photogenerated electrons primarily on TiO_2. Moreover, this photocatalyst exhibited no apparent deactivation after three consecutive times.

As mentioned above, partially or completely substituting the organic ligand H_2BDC of UiO-66 with a light-harvesting organic ligand can broaden its optical absorption. In addition to the organic linker partial substitution of UiO-66 for the CuTCPP (Cu(II) tetra(4-carboxylphenyl)porphyrin) with light-harvesting characteristic, Wang et al. [163] integrated as-prepared CTU (CuTCPP ς UiO-66) or TU (TCPP ς UiO-66) and inorganic semiconductor TiO_2 to synthesize CTU/TiO_2 and TU/TiO_2 nanocomposites toward the conversion of CO_2 to CO, respectively. After the introduction of CuTCPP into UiO-66, the absorption intensity of the CTU dramatically enhanced in visible light region due to the great light-harvesting capability of CuTCPP. The maximum CO production rate of the CTU/TiO_2 nanocomposites reached 31.32 μmol $g^{-1}h^{-1}$, larger than TU/TiO_2 and single TiO_2. For photocatalytic activity better than TU/TiO_2 can be ascribed to the coordination of Cu^{2+} ions with the nitrogen atoms in TCPP, and thus forming another LMCT to ameliorate photocatalytic reactions. The 7-fold greater photocatalytic activity than pristine TiO_2 was primarily due to the improved charge separation caused by the high-efficiency synergistic effect between them. As shown in Fig. 7d, under Xe lamp light, both CTU and TiO_2 can be excited to generate electron-hole pairs. The type-II band alignment after combination induced a rapid transfer of photogenerated electrons from the CTU LUMO to the TiO_2 CB and holes to the opposite direction, thus improving charge separation. The photogenerated electrons in the CB of TiO_2 can reduce CO_2 to CO and low yielding methane (0.148 μmol $g^{-1}h^{-1}$). Additionally, the formation of oxygen vacancies during the synthesis of CTU/TiO_2 was confirmed by X-ray photoelectron spectroscopy, which could provide sufficient photoactive sites for CO_2 reduction and facilitate charge transfer. Taking advantage of the significant effect of oxygen defects on photocatalytic performance, Meng et al. [185] synthesized an innovative oxygen-defective ZnO (O-ZnO)/reduced graphene oxide (rGO)/UiO-66-NH_2 multiphase composite for photocatalytic reduction of CO_2 to CH_3OH and HCOOH via a solvothermal method. The best-in-class photocatalytic

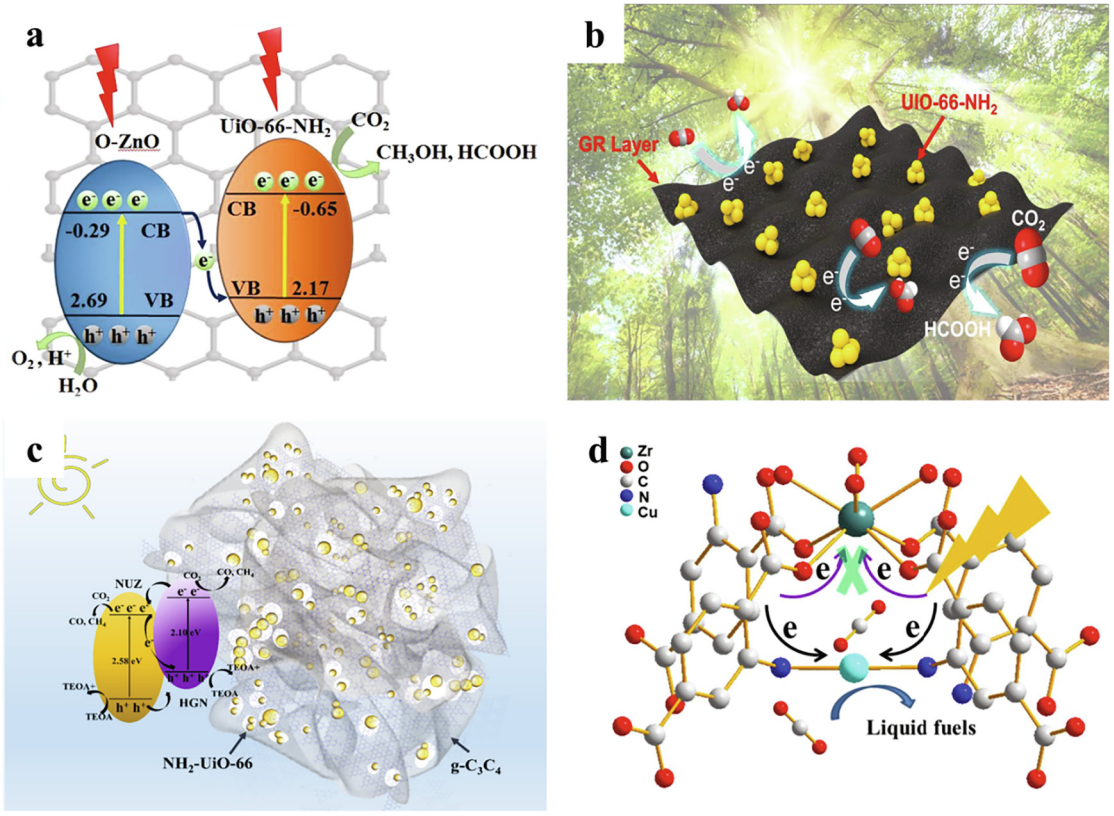

Fig. 8. Schematic illustration of the proposed mechanism of photocatalytic CO_2 over (a) the O-ZnO/rGO/UiO-66-NH_2; (b) UiO-66-NH_2/GR hybrids; (c) NUZ/HGN-35%; (d) Cu SAs/UiO-66-NH_2. Adapted with permission from Ref. [135,176,181,185], Copyright 2020, American Chemical Society, Copyright 2018, Elsevier, Copyright 2019 and 2018, American Chemical Society.

activity was exhibited by the as-prepared photocatalysts, where the evolution rates of CH_3OH and HCOOH were as high as 34.85 and 6.40 μmol $g^{-1}h^{-1}$, respectively. The presence of oxygen vacancies was vital in promotive photocatalytic activity, which can facilitate the adsorption and activation of CO_2, and might sever as photogenerated electron acceptors to hinder the photogenerated charge recombination. The transfer of photogenerated electron-hole on prepared photocatalyst followed the Z-scheme mechanism. Specifically, the CB (-0.65 eV vs NHE) of UiO-66-NH_2 was more negative compared to the CO_2 reduction potential (CO_2/CH_3OH = -0.38 eV and CO_2/HCOOH = -0.61 eV), the electrons accumulated on the CB of UiO-66-NH_2 can easily reduce CO_2 to CH_3OH and HCOOH (Fig. 8a). Moreover, the introduction of rGO with electrical conductivity, which can not only reinforce the contact between UiO-66-NH_2 and O-ZnO, but also generate new photogenerated electron transfer channels, thus significantly increasing the reduction efficiency (Fig. 8a). After six cycles, the photocatalytic activity of O-ZnO/rGO/UiO-66-NH_2 did not decrease significantly, and the crystal structure and morphology of the material did not change noticeably after the reaction. These implied that the high stability of the O-ZnO/rGO/UiO-66-NH_2 during the photocatalytic CO_2 reduction.

In contrast to the above method of constructing heterojunctions, coating UiO-66 on the surface of nanomaterials is another available way to strengthen the photocatalytic performance. For example, by using UiO-66-NH_2 and carbon nanotubes (CNTs) as photocatalyst and co-catalyst, respectively, Wang et al. [204] prepared hierarchical UiO-66-NH_2/CNTs heterojunctions for CO_2 reduction. After exposure to visible light for 4 h, the maximum HCOOH evolution of 18.2 μmol was achieved with 2 wt% CNTs in UiO-66-NH_2/CNTs, due to the tight binding of UiO-66-NH_2 to CNTs and uniform dispersion of UiO-66-NH_2 on CNTs surfaces. Their catalytic ability derived from the visible light excitation of UiO-66-NH_2 to yield photogenerated electron-hole pairs, after which the holes reacted with H_2O molecules to form H^* intermediate products, and then produced HCOOH in gradual hydrogenation with CO_2 molecules. Besides, after six cycles, UiO-66-NH_2/CNTs heterojunctions maintained relatively stable photocatalytic activity and intact crystal structure, due to a good connection between them. In addition, the robust photocatalyst, UiO-66-NH_2 nanocrystals (14.5 nm) highly dispersed onto graphene (GR) by a facile microwave-induced method, was prepared for CO_2 reduction [176]. UiO-66-NH_2 were uniformly dispersed on the surface of GR, and the aggregation of UiO-66-NH_2 synthesized by microwave-induced method can be well avoided by introducing GR. Due to the better interactions of the $-NH_2$ groups with CO_2, UiO-66-NH_2/GR showed an excellent CO_2 adsorption ability with a maximum uptake of 73 cm^3 g^{-1}. Photoelectrochemical results indicated the introduction of GR on UiO-66-NH_2 could improve the utilization visible light efficiency and enhance electron transfer by alleviating recombination of photogenerated electron-hole pairs in UiO-66-NH_2. The obtained UiO-66-NH_2/GR hybrids displayed the maximum selectivity of 78.6% for CO_2 to HCOOH reduction, in which CO_2 photoreduction efficiency (35.5 μmol within 4 h of illumination) reached approximately 11 times higher than pristine UiO-66-NH_2. This extraordinary photocatalytic activity was principally derived from the synthetic route of the microwave-induced method. This synthetic route enabled the rapid in situ crystalline growth of UiO-66-NH_2 on GR due to the presence of local "super hot" dots on GR, resulting in suitable particle size, strong junctions and well dispersed on GR [205]. These advantages provided short paths and little resistance to charge transfer in photocatalytic process [206]. Meanwhile, under visible light irradiation, the high generation of HCOOH was well-maintained even after eight cycles, which indicated that the excellent stability of UiO-66-NH_2/GR synthesized by microwave-induced method. Moreover, the CB of UiO-66-NH_2/GR hybrids was −0.82 eV, higher than the CO_2/HCOOH reduction potential (-0.66 eV) and can trigger the conversion of CO_2 to HCOOH (Fig. 8b) [207,208]. With a view to maximizing the CO_2 reduction efficiency of heterojunctions, the choice of synthesis method is of particular importance. To further confirm it, Wang et al. [181] presented a series of UiO-66-NH_2/g-C_3N_4 composites containing 35 wt% g-C_3N_4 via in situ solvothermal, physical and electrostatic method, respectively. After 12 h of illumination, maximum photocatalytic efficiency achieved by in situ solvothermal synthesis of samples, and the obtained CO yield of 31.7 μmol $g^{-1}h^{-1}$. After the introduction of g-C_3N_4, the absorption edges of UiO-66-NH_2/g-C_3N_4 showed slight red shifts and enhanced light-harvesting ability due to the interaction between UiO-66-NH_2 and g-C_3N_4. Compared to samples synthesized by other synthetic methods, in situ solvothermal process, the $-NH_x$ groups on ultra-thin g-C_3N_4 can be used to immobilize the UiO-66-NH_2 nanocrystals to form the $NH_x - Zr - O$ bond, allowing them to be tightly joined (Fig. 8c). The CB positions of UiO-66-NH_2 and g-C_3N_4 were − 0.65 and − 1.24 eV vs NHE. Thus, based on the thermodynamics, UiO-66-NH_2 and g-C_3N_4 possessed matched CB positions to the reduction of CO_2 to CO (−0.48 V vs NHE). It was this chemical bonding that enabled faster interfacial charge mobility between UiO-66-NH_2 nanocrystals and g-C_3N_4, leading to elevated photocatalytic CO_2 reduction performance. The chemical bonding also effectively immobilized UiO-66-NH_2 on g-C_3N_4 and suppressed the leaching of UiO-66-NH_2, which led to the good stability of UiO-66-NH_2/g-C_3N_4.

Single-atom catalysts with sufficient catalytic active sites and high atomic availability, bringing catalytic science to an atomic-scale perspective, have attracted widespread attention [123-134]. Wang et al. [135] recently employed a photoinduction method to chemically immobilize isolated Cu SAs into UiO-66-NH_2 structure to obtain Cu SAs/UiO-66-NH_2 with coordination mode of atomic level. The loadings of Cu elements were 0.39 wt% in Cu SAs/UiO-66-NH_2, lower than 0.82 wt% in Cu NPs/UiO-66-NH_2. TEM images (Fig. 4b, c) did not observe visible sign for the presence of Cu NPs in Cu SAs/UiO-66-NH_2, but isolated Cu SAs as identified by aberration corrected high-angle annular dark-field scanning TEM (Fig. 4d). The relevant atomic structure characterizations revealed that the Cu atoms were anchored with two N atoms at the atomic level by the UiO-66-NH_2 support. Cu SAs/UiO-66-NH_2 and Cu NPs/UiO-66-NH_2 exhibited similar light absorption with a maximum absorption peak at 500 nm, revealing that the presence of Cu can enhance visible light harvesting ability. However, after 10 h of continuous illumination, the formation rate of methanol and ethanol for Cu SAs/UiO-66-NH_2 were approximately 5.33 and 4.22 μmol $g^{-1}h^{-1}$, respectively, which were significantly greater than Cu NPs/UiO-66-NH_2 and the trace products of pristine UiO-66-NH_2. This indicated the importance and high atomic usability of the incorporation of Cu SAs. Time-resolved PL spectra demonstrated that markedly prolonged lifetime of photogenerated carriers in Cu SAs/UiO-66-NH_2. Also, the significantly enhanced charge separation efficiency of Cu SAs/UiO-66-NH_2 as revealed by photoelectrochemistry properties. These results indicated that the separation and transfer efficiency of Cu SAs/UiO-66-NH_2 was remarkably improved due to the increased electron trapping ability of Cu SAs in UiO-66-NH_2. The plausible mechanism of CO_2 reduction was proposed by the authors in Fig. 8d. As normal, photogenerated electron–hole pairs were excited and generated over UiO-66-NH_2 upon visible light, and then photogenerated electrons transferred from H_2ATA to the Zr oxo cluster. Notably, photogenerated electrons can also be transferred to Cu atoms and changed their valence state, then activating CO_2 adsorbed on UiO-66-NH_2 to gradually form ethanol and methanol under adequate photogenerated electrons in Cu SAs. More importantly, the stability test indicated that the Cu SAs/UiO-66-NH_2 with no visible active degradation after four cycles, suggesting the

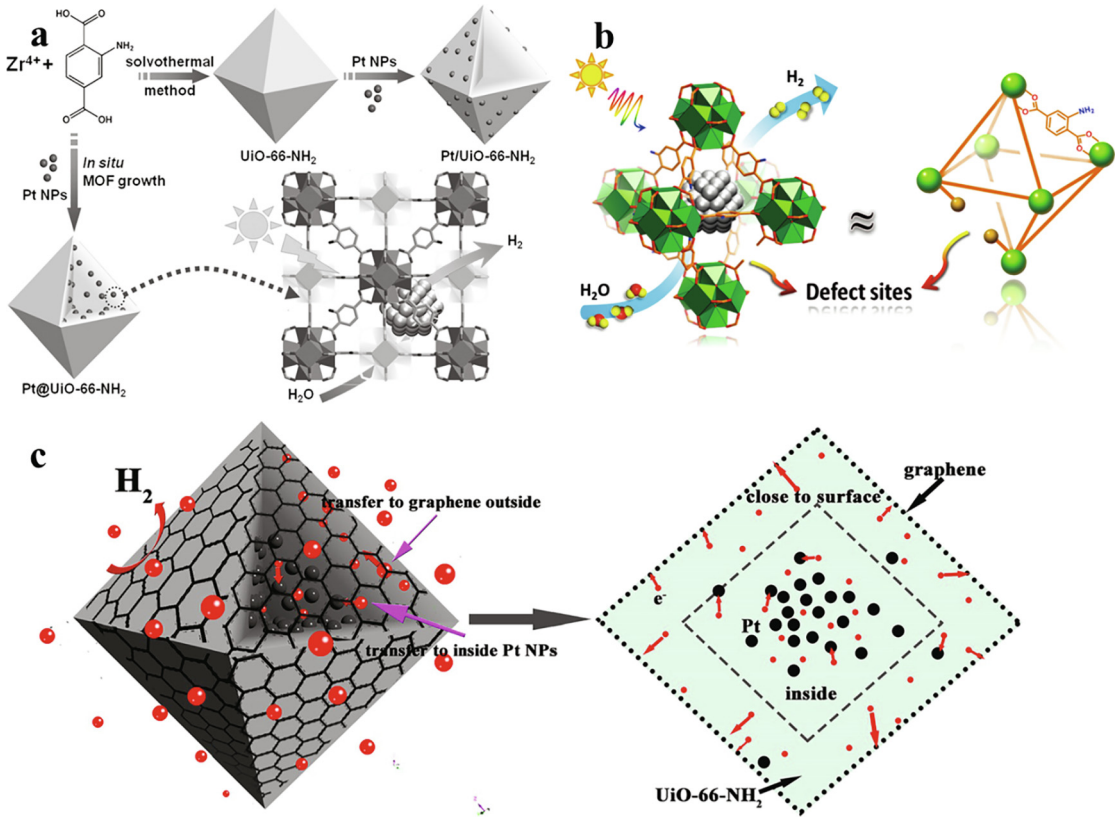

Fig. 9. Schematic diagrams for (a) the synthesis of Pt/UiO-66-NH_2 and Pt@UiO-66-NH_2, highlighting the photocatalytic hydrogen production process on Pt@UiO-66-NH_2; (b) photocatalytic hydrogen evolution over Pt@UiO-66-NH_2 with structural defects; (c) the mechanism involved in the bidirectional electron transfer between the inner and outer decoration of UiO-66-NH_2. Adapted with permission from Ref. [93,122,217], Copyright 2019, 2016 and 2018 WILEY-VCH.

robust bonding between isolated Cu SAs and the UiO-66-NH_2 support.

4.1.2. Hydrogen generation

Hydrogen, as a long-term and clean fuel, is the ideal alternative to fossil fuels and can help maintain a sustainable energy future [209-213]. Recently, tremendous progress has been devoted to employing artificial photocatalytic materials to decompose water for hydrogen generation [188,210,214-216]. Similarly, the exploitation of modified UiO-66 for hydrogen generation through water splitting has attracted considerable interest. For instance, Silva et al. [29] selected UiO-66 and aminated-UiO-66 (UiO-66-NH_2) as photocatalysts for hydrogen generation in water/methanol mixtures. The authors found that UiO-66 and UiO-66-NH_2 were isoreticular and the introduction of $-NH_2$ groups present in the micropores. Nevertheless, the presence of $-NH_2$ groups possessed dramatic effect on the photocatalytic performance of UiO-66. Exposure of UiO-66 in water/methanol with visible light did not lead to hydrogen generation. Similarly, UV irradiation of UiO-66 did not detect hydrogen in a solution without sacrificial electron donors. In contrast, UiO-66 exhibited poor hydrogen generation activity only in the presence of methanol as a sacrificial electron donor and UV illumination. Another, UiO-66-NH_2 demonstrated a slightly better hydrogen generation activity and emerged with an additional light photoresponse than pure UiO-66 owing to the presence of the NH_2 groups. Obviously, the presence of $-NH_2$ caused a new strong absorption band at 300 ~ 440 nm, which was not present in the parent UiO-66. However, the authors did not proceed to investigate the hydrogen generation activity of UiO-66-NH_2 under visible light. Additionally, the authors introduced Pt NPs on the UiO-66 and UiO-66-NH_2 surface, respectively, and achieved a significant increase in hydrogen generation activity. The authors further clearly confirmed that methanol was the most likely hydrogen source, and water improved the photocatalytic performance. Also, the spectroscopic evidence based on laser flash photolysis supported long-lived charge separation of UiO-66. These works carried out by the authors, although they did not achieve satisfactory results in terms of photocatalytic activity, provides an opportunity for future functional modifications of UiO-66.

Further, by introducing Pt NPs into different positions of amino-functionalized UiO-66-NH_2, Xiao et al. [122] prepared Pt-decorated UiO-66-NH_2 nanocomposites (Pt/UiO-66-NH_2 and Pt@UiO-66-NH_2), verified the feasibility of hydrogen generation under visible light and the influence of different Pt NPs modification positions on hydrogen generation activity (Fig. 9a). No accumulation of Pt NPs occurred in Pt/UiO-66-NH_2 and Pt@UiO-66-NH_2 and their particle size remained around 3 nm. Both samples exhibited approximately the same band gap (2.76 eV), but Pt@UiO-66-NH_2 possessed a stronger absorption than Pt/UiO-66-NH_2. This was ascribed to the close packing between UiO-66-NH_2 and Pt which contributed to markedly high scattering at long wavelengths. Under visible-light irradiation, all Pt-decorated UiO-66-NH_2 nanocomposites displayed remarkably ameliorated hydrogen productivity over pure UiO-66-NH_2 due to the low overpotential of Pt, which acted as an ideal photogenerated electron capture and a reduction site for hydrogen generation. However, the Pt@UiO-66-NH_2 displayed a significantly enhanced hydrogen generation rate (257.38 mmol $g^{-1}h^{-1}$), which was approximately 5 times better over Pt/UiO-66-NH_2 (50.26 mmol $g^{-1}h^{-1}$). The strengthened catalytic activity was owing to the shorter electron transport distance and better charge separation efficiency of Pt NPs decorated within UiO-66-NH_2. Moreover, the decoration of Pt NPs within the

UiO-66-NH_2 can effectively protect against leaching and agglomeration of Pt NPs, exhibiting high stability and recyclability. Besides, with the superiority of the Pt NPs decoration inside UiO-66-NH_2 (Pt@U6N), Wang et al. [217] also demonstrated that wrapping the outer surface of Pt@U6N with graphene oxide served to facilitate photogenerated electrons transfer on the surface (Fig. 9c). Except for pre-functionalization of organic linkers, the construction of dye-sensitized systems using RhB dye and ErB dye to sensitize Pt loaded UiO-66, is also an efficient strategy to enhance the visible light photoresponse [137,141]. In addition, defect engineering is available for modulating the energy band and electronic structure of semiconductor materials [106]. Ma et al. [93] used acetic acid as the modulator to introduce structural defects in UiO-66-NH_2-X (X = the molar equivalents of acetic acid), systematically investigated the effect of structural defects on photocatalytic performance. All UiO-66-NH_2-X had a strong light-harvesting capacity and were almost independent of the structural defects or particle size. However, negligible hydrogen generation (9.4 μmol $g^{-1}h^{-1}$) achieved by Pt@UiO-66-NH_2-0 with few structural defects. With increasing structural defects, the photocatalytic hydrogen generation efficiency exhibited a volcano-type trend. Pt@UiO-66-NH_2-100 had the most moderate defect structure for causing the energy of the unoccupied d orbital of Zr atoms to decrease and promoting photogenerated electron-hole separation, exhibiting the highest activity (381.2 μmol $g^{-1}h^{-1}$) (Fig. 9b). Moreover, Pt@UiO-66-NH_2-100 can be recycled at least 10 times and its structure well retained without significant leaching or aggregation of Pt NPs, showing excellent prospects for practical applications.

The encapsulation of Pt NPs in MOFs has been shown the enhanced photogenerated electron-hole separation. Similarly, this could also be achieved with encapsulation of Au nanodots in MOFs. Au nanodots in the pores of thiol-functionalized UiO-66 though the adsorption force of thiol worked as photogenerated electron acceptors due to the Schottky junction, resulting in highly efficient separation of charge carriers [121]. Although the encapsulation of noble-metals has been shown to explosively strengthen photocatalytic activity, its cost and scarcity will hinder large-scale dissemination. Moreover, the excess concentration of noble-metal NPs will agglomerate on the surface, becoming the recombination center of photogenerated charge carriers and reducing catalytic efficiency.

The noble-metals can be used as co-catalysts to enhance the hydrogen generation efficiency of modified UiO-66 photocatalysts, however, UiO-66 also can be more effective co-catalysts for promoting hydrogen generation activity with other semiconductor materials. Peng et al. [167] developed effective visible-light-driven photocatalysts (UiO-66@$ZnIn_2S_4$) by encapsulating UiO-66 octahedral nanoparticles with $ZnIn_2S_4$ nanosheets for hydrogen generation (Fig. 10a). Almost no H_2 was generated when using UiO-66 alone because UiO-66 has negligible visible light absorption. Notably, the hydrogen generation rate of the optimum UiO-66@$ZnIn_2S_4$ was 3061.61 μmol h^{-1} g^{-1}, which was considerably>5% Pt loaded $ZnIn_2S_4$ and UiO-66/$ZnIn_2S_4$. This demonstrated that the hierarchical structure with a tight contact interface formed by the surface modification of UiO-66 on $ZnIn_2S_4$ nanosheets can effectively facilitate photogenerated charge carrier separation. The mechanism of high hydrogen generation performance in the UiO-66@$ZnIn_2S_4$ were proposed in Fig. 10b. It was suggested only the $ZnIn_2S_4$ with visible-light harvesting could generate charge carriers. The photogenerated electrons at the CB (-1.01 eV vs NHE) of $ZnIn_2S_4$ could be rapidly injected to the LUMO (-0.64 eV vs NHE) of UiO-66 because of more negative CB of

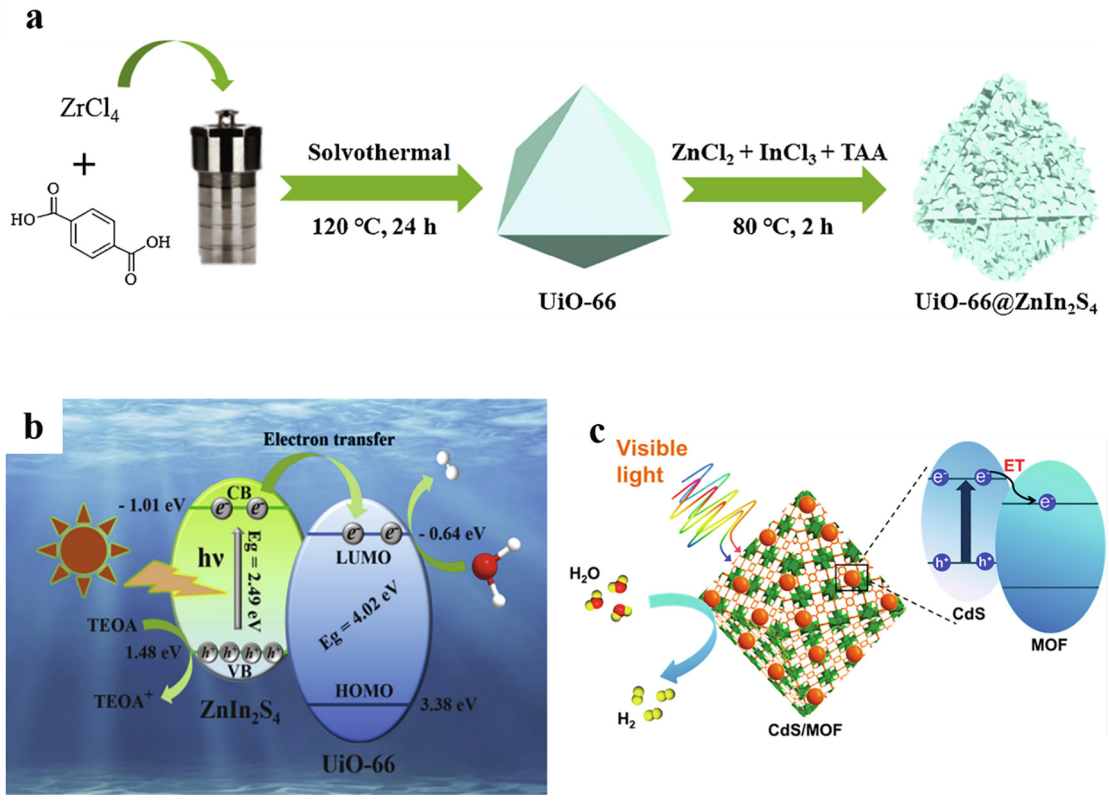

Fig. 10. Schematic illustration of (a) the synthetic process for UiO-66@$ZnIn_2S_4$ photocatalyst, (b) the photocatalytic mechanism for hydrogen evolution over UiO-66@$ZnIn_2S_4$ photocatalyst under visible light irradiation; (c) the photocatalytic mechanism for hydrogen evolution over CdS/UiO-66 composites. Adapted with permission from Ref. [67,167], Copyright 2018, American Chemical Society and Copyright 2020, Elsevier.

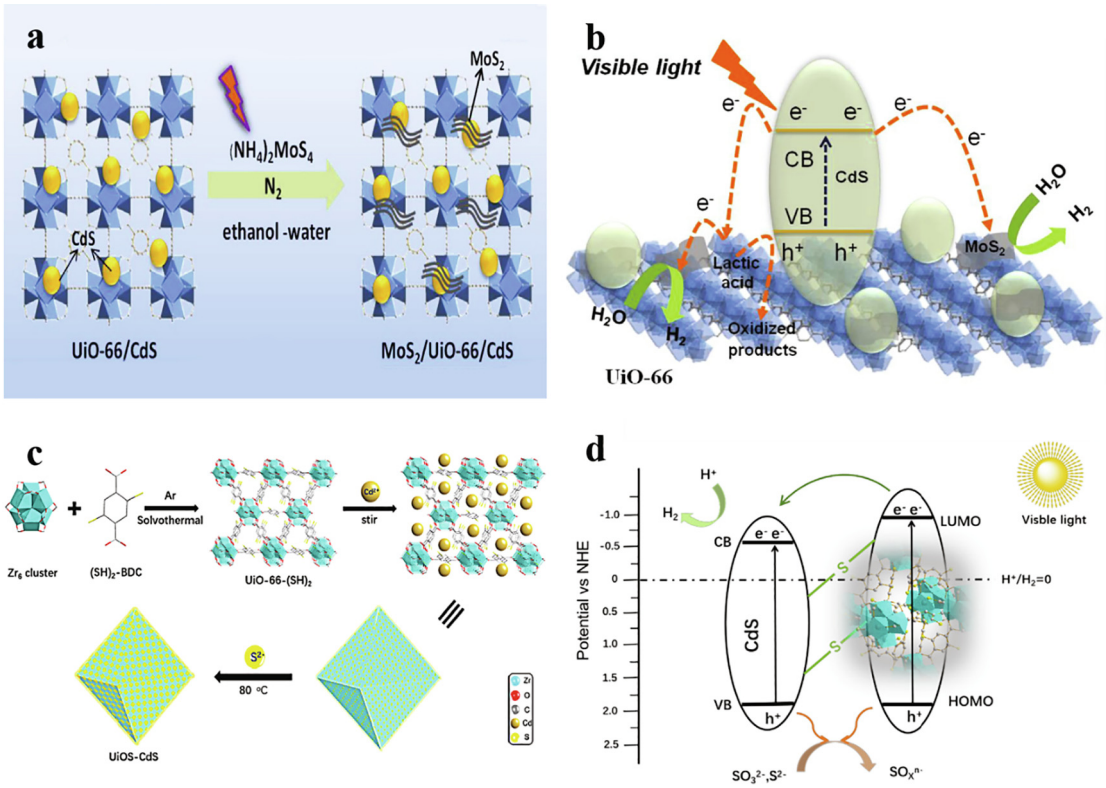

Fig. 11. Schematic illustration of (a) the fabrication of MoS_2/UiO-66/CdS composites; (b) the charge transfer in the MoS_2/UiO-66/CdS composite under visible light irradiation; (c) the synthesis process of UiOS-CdS composites; (d) the charge transfer process over UiOSCdS0.7 photocatalyst under visible light irradiation. Adapted with permission from Ref. [78,219], Copyright 2021 and 2015, Elsevier.

$ZnIn_2S_4$, and then reacted with H^+ to generate H_2. Meanwhile, the photogenerated holes at the VB of $ZnIn_2S_4$ were quenched by the sacrificial agent, avoiding the recombination of charge carriers. Notably, during the photocatalytic reaction, the wavelength of incident light largely influenced the rate of hydrogen generation and apparent quantum yield of the UiO-66@$ZnIn_2S_4$. Upon 400 nm incident monochromatic light, UiO-66@$ZnIn_2S_4$ possessed a high apparent quantum yield of 19.39% than at 420 nm (9.84%), indicting visible light excitation can indeed drive hydrogen generation. Additionally, after 4 cycles, the hydrogen generation efficiency of UiO-66@$ZnIn_2S_4$ did not deactivate apparently, demonstrating the good stability of the prepared photocatalyst.

The same is true for metal sulfide modification of UiO-66, Xu et al. [67] developed a series of CdS/UiO-66 nanocomposites to generate hydrogen from photocatalytic water splitting. The system employing UiO-66 alone did not generate hydrogen due to its unresponsive property to visible light. After modifying UiO-66 with CdS, CdS/UiO-66 nanocomposites featured absorption properties of both constituents, and the visible absorption increased with increasing CdS content in the nanocomposites. All the CdS/UiO-66 nanocomposites showed considerably enhanced photocatalytic hydrogen generation activity than pure CdS. The best hydrogen generation activity can reach 1725 μmol $g^{-1}h^{-1}$ by CdS/UiO-66 (10). On the one hand, UiO-66 can act excellent support to maintain a well-dispersed nature and constrain the size of CdS particles, resulting in sufficient photocatalytic active sites. On the other hand, the appropriate band positions of CdS and UiO-66 allowed it thermodynamically possible for photogenerated electron transfer from the CB (-0.7 eV vs NHE) of CdS into LUMO (-0.6 eV vs NHE) of UiO-66 in CdS/UiO-66 composites, which was favorable for significantly inhibiting the recombination of photogenerated charge carriers (Fig. 10c). Eventually, elevated photocatalytic hydrogen generation activity was achieved by CdS/UiO-66. However, CdS/UiO-66 showed relatively poor stability and recyclability, and can only maintain high hydrogen generation activity in three cycles, which may greatly limit its prospects in practical applications.

UiO-66 with large specific surface area and is able to greatly disperse CdS particles, and MoS_2 as co-catalyst, Shen et al. [218] developed MoS_2/UiO-66/CdS photocatalysts for hydrogen generation driven by visible light. In detail, upon the illumination of a 300 W xenon lamp, MoS_2 were photodeposited on prepared UiO-66/CdS composites to synthetic MoS_2/UiO-66/CdS via a photo-assisted strategy (Fig. 11a). Interestingly, using MoS_2–CdS as a comparison, the as-prepared photocatalysts with the same amount of MoS_2 demonstrated much higher hydrogen generation activity, indicating the importance of the presence of UiO-66. Additionally, the results manifested that the hydrogen generation activity of MoS_2/UiO-66/CdS was greatest when MoS_2 content reached 1.5%, after which the photocatalytic activity decreased along with the content increased. This is most likely due to the light-shielding effect of MoS_2, and the excessive MoS_2 content with too much light absorption weaken the photoexcitation of CdS [219,220]. When containing 1.5 wt% MoS_2 and 50 wt% UiO-66, the MoS_2/UiO-66/CdS composites reached up to 650 μmol h^{-1}hydrogen generation rate, 60 times that of CdS counterparts. The photocatalytic hydrogen generation mechanism of MoS_2/UiO-66/CdS was proposed in Fig. 11b. It was suggested that CdS could be photoexcited under visible light ($\lambda \geq 420$ nm). The photogenerated electrons in the CB of CdS can directly migrate to MoS_2 nanosheets or migrate to UiO-66 followed by MoS_2 nanosheets, then reacting with the adsorbed H^+ ions to generate hydrogen. Simultaneously, the photogenerated holes in the VB of CdS would be quickly scavenged by lattice acid. In order to more firmly anchor CdS on UiO-66 and

effective prevention of CdS aggregation, Mao et al. [78] first immobilized Cd^{2+} ions in the UiO-66-$(SH)_2$ cavities by coordination with thiol groups under alkaline conditions to form UiO-66-$(S\text{-}Cd)_2$, and then reacted with thiourea to develop UiO-66-$(S\text{-}CdS)_2$ (Fig. 11c). A great number of CdS quantum dots were uniformly attached on external surface (about 3 nm) and/or encapsulated within the cavity (about 1 nm) of UiO-66-$(SH)_2$ without any agglomeration. After incorporating CdS into UiO-66$(SH)_2$, the absorption edges of UiO-66-$(S\text{-}CdS)_2$ showed a large red-shift and positioned between CdS (550 nm) and UiO-66-$(SH)_2$ (450 nm). Notably, the existence of thio linkage linkers between them could play a role as the effective bridge that greatly facilitated the interfacial transfer of carriers (Fig. 11d). Subsequently, the optimized UiO-66-$(S\text{-}CdS)_2$ with 40 wt% of $Cd(NO_3)_2{\cdot}4H_2O$ showed the best photocatalytic hydrogen generation activity under visible light irradiation without noble-metal co-catalysts, with a yield of 15.32 mmol $g^{-1}h^{-1}$ and an apparent quantum efficiency of 11.9%, which was much stronger than the above discussed photocatalysts. Moreover, the morphology of the UiO-66-$(S\text{-}CdS)_2$ remained unchanged during a 48-h test, demonstrating the exceptional stability of the UiO-66-$(S\text{-}CdS)_2$.

4.2. Solving environmental remediation issues

4.2.1. Removal of organic pollutants

With the rapid expansion of modern industry, there is a growing concern about the deteriorating environmental pollution [221-223]. Industrial wastewater contains a large number of organic pollutants (e.g., dyes, sulfamethazine, pharmaceuticals, pesticides etc.), causing potential harm to the environment and human health [224-226]. In recent years, photocatalysis as an effective strategy has been widely employed to degrade pollutants. Currently, an increasing number of scholars are researching on UiO-66-based materials used as some of the most effective photocatalysts for removing these organic pollutants [147,164,227].

4.2.1.1. Antibiotics. Antibiotics are omnipresent in the aquatic environment today due to their widespread production and application. Their carcinogenicity, persistence, mutagenicity, aquatic toxicity and other ecological effects have caused widespread concern [228]. The modified UiO-66 has the advantages of excellent porosity, high photoactivity and good water stability, making it an ideal platform for photocatalytic removal of antibiotics. In the photocatalytic degradation of organic pollutants, the adsorption of pollutant molecules is the first step and one of the important factors that determine the degradation efficiency of organic pollutants [229]. Gao et al. [43] successfully introduced TCPP into UiO-66 by the method of "one-pot synthesis", which was employed to degrade diclofenac (DF). Through the experiment of maximum adsorption capacity, the authors pointed out that the adsorption of TCPP@UiO-66 composites on pollutants was not only simple physical adsorption, but also through electrostatic interaction, Lewis acid-base interaction, π-π interaction, anion-π interaction, hydrogen bonding. In addition, the most suitable TCPP@UiO-66 complex was photocatalytically efficient in the degradation of DF with 99% removal under simulated sunlight irradiation. The high efficiency of the photoreaction process was confirmed by the authors to contain type II photosensitization reaction and photocatalytic process (Fig. 12). In photosensitization reaction, under irradiation, TCPP can be excited to yield ^{1}[TCPP]*. What's more, rapid production of the sensitizer triplet state ^{3}[TCPP]* through inter-system crossover process, which can be used to generate $^1O_2$ with undissolved O_2 for the degradation of DF. In photocatalytic

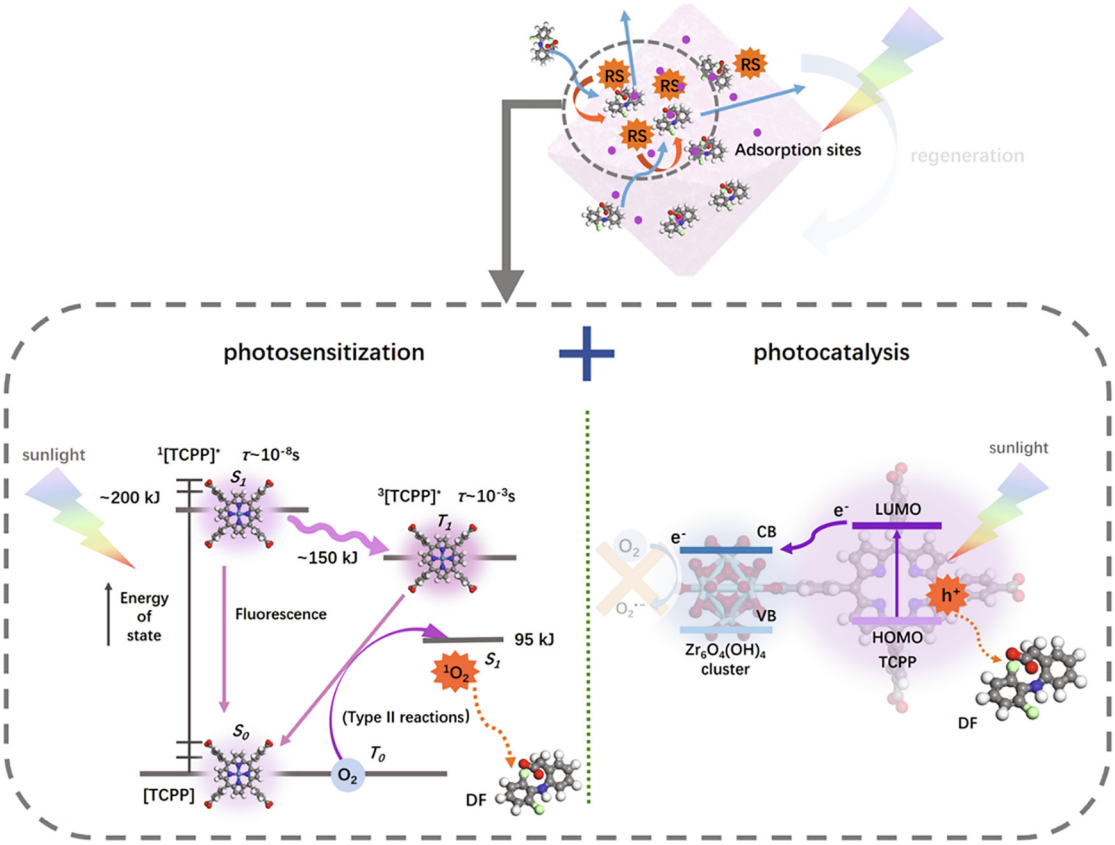

Fig. 12. Schematic the types II photosensitization reaction and photocatalytic process in TCPP@UiO-66. Adapted with permission from Ref. [43], Copyright 2020 American Chemical Society.

process, under sunlight irradiation, the TCPP linkers are excited to transfer photogenerated electrons into Zr ions, then yielding $[TCPP]^+$. In addition, photogenerated electrons and holes are produced and photogenerated holes can take part in the degradation of DF.

The introduction of small amounts of transition metal elements into the framework of MOFs can be a significant contribution to the optimization of adsorption and photocatalytic performance. Cao et al. [228] reported degradation of tetracycline (TC) by a series of Co-containing UiO-66 CoUiO-66. The authors found that the amount of TC adsorbed by CoUiO-66 increased with increasing cobalt content. This may be due to the valence electrons provided by the doped cobalt, which facilitated the binding of the adsorbed TC to the metal center [230]. What is more, the doped cobalt also contributed to the photodegradation process, which could induce an additional light photoresponse and facilitate the electron transfer though MMCT excitation between Co and Zr species. With such a dual effect, under simulated sunlight exposure, the degradation of adsorbed TC molecules over CoUiO-66–1 (the molar ratio of the Zr: Co was 1:1) can reach over 94% of the initial concentration. Under simulative sunlight irradiation, CoUiO-66 could be photoexcited to generate electron-hole pairs, and photogenerated electrons transferred from the photoexcited H_2BDC to the Zr oxo clusters and then to Co. Based on MMCT excitation between Co and Zr species, the electron-hole pairs were effectively separated. The photogenerated electrons reacted with O_2 to generate $\cdot O_2^-$ and subsequently yielded ·OH. Then the formed $\cdot O_2^-$ and ·OH effectively degraded TC molecules. The effect of pH on degradation efficiency of CoUiO-66–1 studied and the result indicated that, the adsorption of TC rose with increasing pH and then decreased, with a maximum at 10. The reason was explained as that, different pH values could affect the protonation state of the TC and the CoUiO-66–1 surface charge, which will change their interaction forces.

4.2.1.2. Dyes. In recent years, the water environment has been forced to accept a large amount of dye effluent from the textile, paper and printing industries, which poses a serious threat to human health. Fortunately, the modified UiO-66 photocatalyst also excels at removing dyes. Sha et al. [227] first developed a series of Ag_2CO_3/UiO-66 composites for the degradation of RhB with superior photocatalytic activity through a simple solution method. In all of the prepared Ag_2CO_3/UiO-66 composites, the RhB molecules were largely removed within 2 h. Photocorrosion was still a very common phenomenon in most Ag_2CO_3-based photocatalysts. However, after four cycles of degradation experiments, the Ag_2CO_3/UiO-66 composites were still able to retain most of their initial photocatalytic activity. This suggested that a strong interaction between Ag_2CO_3 and the UiO-66 support, which was beneficial for inhibiting the photocorrosion of Ag_2CO_3 and improving the structural stability of the final photocatalyst.

Recently, the modification of UiO-66 with g-C_3N_4 have gathered much notice in photocatalytic degradation of organic dyes because of its low-cost, proper band structure (2.7 eV), non-toxic and chemical stability properties [170,202,231]. In 2018, Zhang et al. [151] fabricated low-cost g-C_3N_4/UiO-66 nanohybrids under solvothermal condition for the degradation of RhB. The prepared photocatalysts possessed high degradation activity (0.00899 min^{-1}), which was mainly ascribed to the remarkable structural stability and permanent porosity of UiO-66, the obvious visible light response of g-C_3N_4, as well as the synergistic effect of the two monomers. The synergistic effect derived from matched energy band structure of the two monomers, which can induce the directional transfer of electrons, thereby avoiding the recombination of charge carries. To be specific, both UiO-66 and g-C_3N_4 could be excited under artificial solar light irradiation, the photogenerated electrons on CB (-0.79 eV vs NHE) of g-C_3N_4 were injected into CB (-0.53 eV vs NHE) of UiO-66. Meanwhile, the CB of UiO-66 and g-C_3N_4 were more negative than $O_2/\bullet O_2^-$ potential (-0.33 eV vs NHE), the O_2 would be reduced by photogenerated electrons to form $\bullet O_2^-$. Besides, the adsorbed water molecule can be oxidized by photogenerated holes of UiO-66 to produce •OH due to the VB (+3.31 eV vs NHE) of UiO-66 was more positive than $\bullet OH/H_2O$ potential (+2.4 eV vs NHE). Eventually, RhB were dominantly degraded by the strongly oxidizing h^+, $\bullet O_2^-$ and •OH. After 4 cycles of RhB oxidation, the photocatalytic ability of g-C_3N_4/UiO-66 showed no obvious deactivation, indicating that the photocatalyst exhibited good stability and could be adapted repeatedly for RhB removal. However, given the complexity of the synthesis requiring two solvothermal reactions, Zhang et al. [172] adopted a straightforward method to thermally anneal the mixture of UiO-66 octahedrons and g-C_3N_4 nanosheets in air atmosphere to obtain UiO-66/g-C_3N_4 (UC) hybrids for the oxidative removal of MB under visible light. UC hybrids exhibited an absorption edge at around 480 nm and thus responded to visible light because of the existence of g-C_3N_4 nanosheets (about 485 nm). Moreover, the exceptional heterojunction between g-C_3N_4 and UiO-66 can promote charge transfer because of the inner electric field, ultimately boosting photocatalytic efficiency for removal of MB. The best removal efficiency was obtained for UC hybrids capable of removing almost all MB in 240 min. Additionally, after five cycles of degradation, the degradation efficiency of MB did not decrease significantly and the crystal structure of UC was well maintained, and the loss of UC during the recycling process was minimal.

4.2.1.3. Other organic pollutants. In addition to antibiotics and organic dyes, several studies have focused on the removal of other organic pollutants by modified UiO-66 photocatalytic systems. For instance, Fakhri et al. [184] successfully synthesized two ternary heterojunctions (UiO-66@metal oxides/graphene oxide) containing different metal oxides ZnO and TiO_2 for the photodegradation of TC and malathion (as a member of organophosphates) pollutants in the environment using a straightforward ultrasound-solvothermal technique. This design developed a ternary heterojunction Z-scheme mechanism and created compact atomic decorations, dense oxygen functionality, better dispersion, good separation of carriers, good electron mobility on graphene oxide layers and high specific surface area. Subsequently, under optimal conditions, UiO-66@ZnO/graphene oxide showed the highest photodegradation efficiency for TC (81%) and malathion (100%) within 90 min. Xue et al. [232] fabricated the photocatalyst BiOBr/UiO-66 with visible light responsive through a simple solution process, and applied it to the degradation of atrazine. Compared with pure BiOBr, the photocatalytic performance of BiOBr/UiO-66 material for the degradation of atrazine upon visible light irradiation was significantly improved, up to about 88%. However, the degradation efficiency of atrazine was considerably reduced when this catalyst was applied to actual water bodies. Moreover, the sulphate and bicarbonate ions in water exhibited a significant inhibition of photocatalytic degradation efficiency of atrazine by BiOBr/UiO-66.

4.2.2. Anion reduction (Cr(VI), Se(VI))

Hexavalent chromium (Cr(VI)), one of the heavy metal ions, is the most toxic form of Cr and is approximately 300 times more toxic than trivalent Cr (Cr(III)) [233]. Due to their high toxicity, there is an urgent requirement for practicable and efficient methods to remove these Cr(VI) contaminants [234]. In this regard, the modified UiO-66 photocatalyst shows extraordinary adsorption and photocatalytic degradation of Cr(VI). Li et al. [162] developed series S-TiO_2/UiO-66-NH_2 nanocomposites via the incorporation as-prepared S-TiO_2 into the framework of UiO-66 by facile ball-milling method for Cr(VI) reduction (Fig. 13a). U1T3 (composite with a mass ratio of 3 between S-TiO_2 and UiO-66-NH_2) demonstrated optimum reduction efficiency, achieving a 94.9 % Cr(VI)

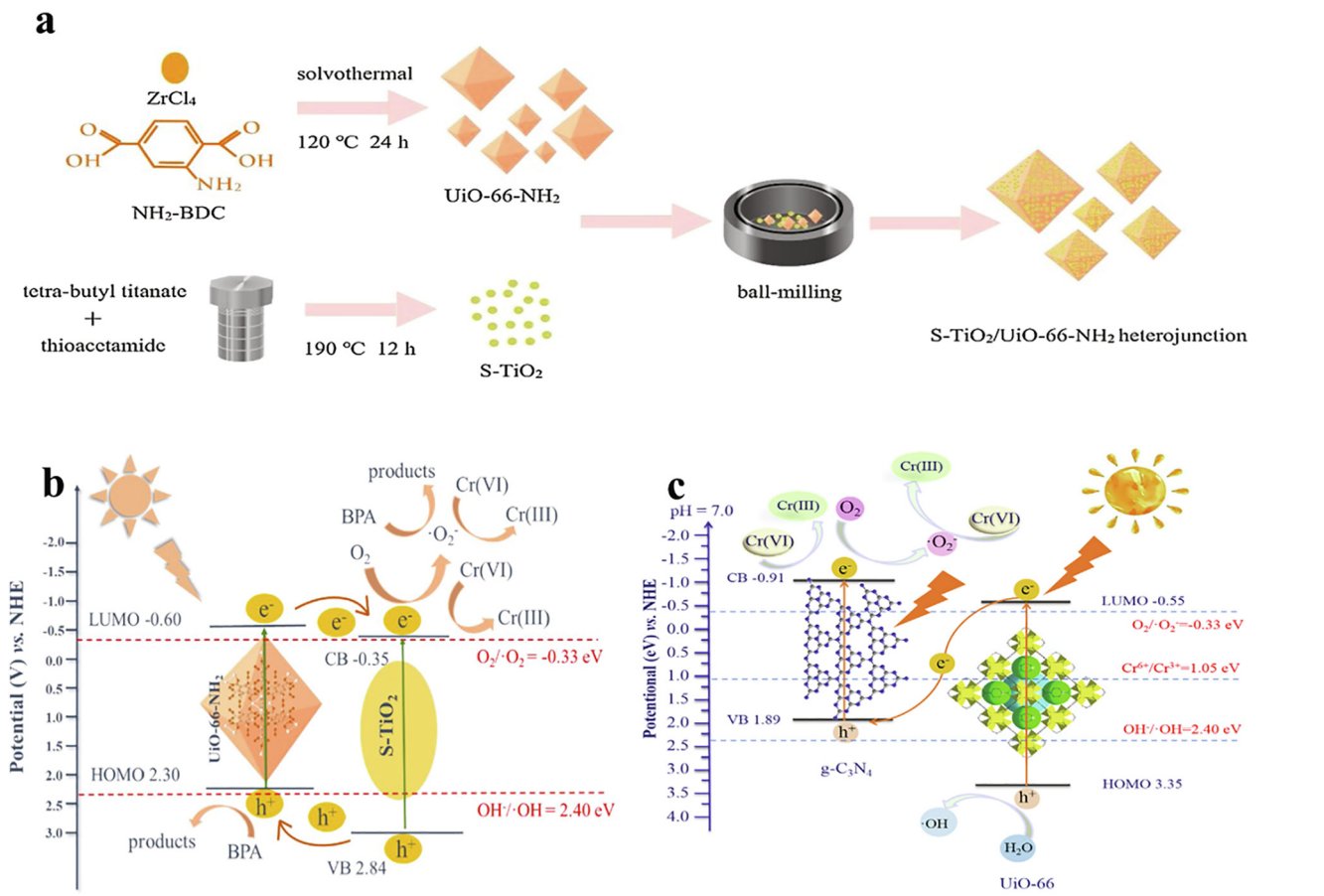

Fig. 13. Schematic illustration of (a) the fabrication of S-TiO_2/UiO-66-NH_2 composites; (b) the mechanism of photocatalytic system about the Cr(VI) reduction over U1T3; (c) The proposed mechanism for Cr(VI) reduction over g-C_3N_4/UiO-66. Adapted with permission from Ref. [162,182], Copyright 2020 and 2019, Elsevier.

reduction in 45 min, followed by a complete reduction in 75 min. The authors confirmed that the strong interaction between them gave U1T3 an excellent charge separation and transfer efficiency. The authors also revealed the type-II mechanism of heterojunction photocatalytic system about the Cr(VI) reduction (Fig. 13b). It was suggested that both UiO-66-NH_2 and S-TiO_2 could be excited under visible light irradiation. The photogenerated electrons in the LUMO of UiO-66-NH_2 can direct migrate to the CB of S-TiO_2 and participate in Cr(VI) reduction, due to LUMO of UiO-66-NH_2 (-0.6 eV vs. NHE) was higher than CB of S-TiO_2 (-0.35 eV vs. NHE). Furthermore, because the LUMO of UiO-66-NH_2 (-0.6 eV vs. NHE) and CB of S-TiO_2 (-0.35 eV vs. NHE) were higher than that of $O_2/\bullet O_2^-$ (-0.33 eV vs. NHE), $\bullet O_2^-$ could be produced (Eq. (4)) to involve in Cr(VI) reduction to Cr(VI) but exerted minor effect. What's more, this composite also can be used as a bifunctional photocatalyst for the oxidation of bisphenol A, where $\bullet O_2^-$ and photogenerated holes can be used in this reaction process. In the 4th cycle, because of the adsorption of Cr species on the photocatalyst surface, the Cr (VI) removal rate of U1T3 decreased to 85.0%. However, it was still much stronger than the UiO-66-NH_2 (34.8 %) and S-TiO_2 (23.7 %), indicating the better reusability and stability of U1T3.

With regard to the previously mentioned disadvantages of type-II heterojunction photocatalyst, the construction of Z-scheme heterojunction photocatalyst has been proven to a convenient and effective strategy to avoid these problems. Yi et al. [182] also fabricated series Z-scheme g-C_3N_4/UiO-66 heterojunctions following a straightforward ball-milling method, which were employed as white-light reactive photocatalysts to achieve extraordinary reduction of Cr(VI). The influence of initial pH on the Cr(VI) reduction was investigated and the results manifested that a relatively lower pH was preferable for Cr(VI) reduction. When pH = 2, BG60U40 containing 60 wt% g-C_3N_4 and 40 wt% UiO-66 achieved the best-in-class Cr(VI) photocatalytic reduction efficiency of 99% within 40 min. This was because under low pH, $Cr_2O_7^{2-}$ was the dominant form of Cr(VI) and the excessive H^+ could facilitate the conversion of Cr(VI) to Cr(III) [235]. However, Cr(VI) was mainly present as CrO_4^{2-} and the corresponding efficiency was affected in the opposite way under alkaline conditions [236]. Moreover, under high pH conditions, $Cr(OH)_3$ precipitates formed by the reduction process will hide the active sites with reduced Cr(VI) reduction performance [237]. The authors also proposed that g-C_3N_4/UiO-66 was consistent with the Z-scheme mechanism for Cr(VI) reduction (Fig. 13c). Such an electron transfer process can optimize the redox capability of Z-scheme heterojunction photocatalysts by maintaining the photogenerated electrons in g-C_3N_4, which had a high reduction capability to Cr(VI) reduction via sequential one-electron-transfer steps [238,239]. To be specific, the CB (-0.91 eV vs NHE) of g-C_3N_4 was more negative than that of Cr(VI)/Cr(III) pairs (1.05 eV vs NHE), and the electrons can readily reduce Cr(VI) to form Cr(III). The Cr(VI) reduction efficiency of BG60U40 did not decrease significantly after six runs and maintained its structural integrity, indicating that BG60U40 can stably and efficiently operate in long-term photocatalytic reactions.

Recently, by using the $ZrOCl_2{\cdot}8H_2O$ as the Zr precursor, NH_2-BDC as organic linkers, and following postsynthetic treatment by Ti ion substitution, Feng et al. [81] synthesized Ti-incorporated $ZrOCl_2{\cdot}8H_2O$-based UiO-66-NH_2 U-OCl-Ti as robust photocatalysts for Cr(VI) reduction (Fig. 14a). Due to the competition of the H_2ATA

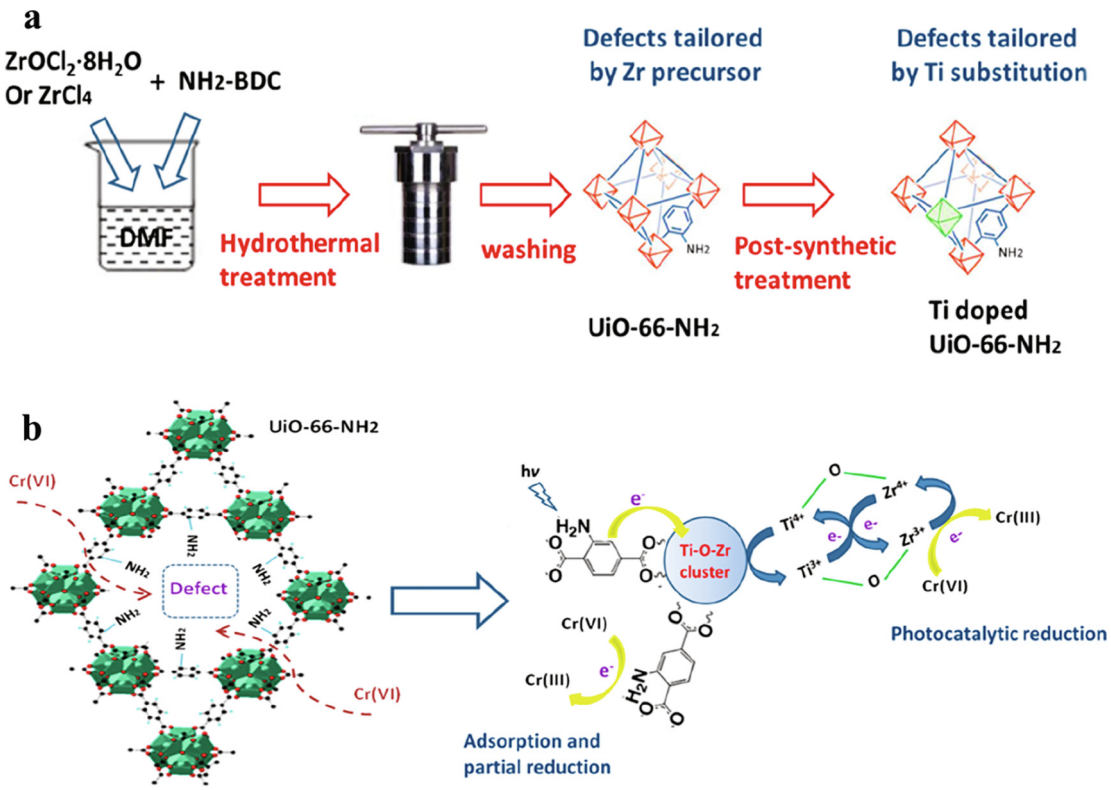

Fig. 14. Schematic illustration of (a) the progressive synthesis of U-OCl-Ti; (b) adsorption and photocatalytic mechanism of U-OCl-Ti for Cr(VI) reduction. Adapted with permission from Ref. [81], Copyright 2019 American Chemical Society.

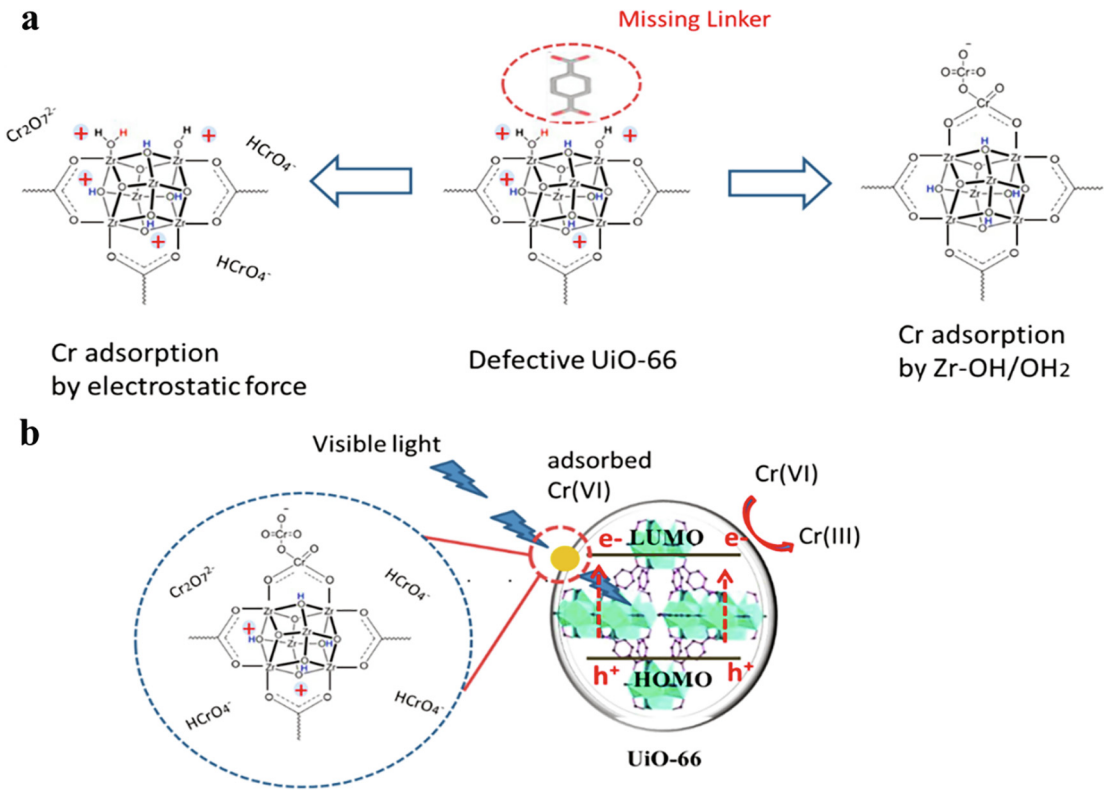

Fig. 15. Schematic illustration of (a) the adsorbing mechanism; (b) photosensitization-derived photocatalytic reduction of Cr(VI) to Cr(III). Adapted with permission from Ref. [108], Copyright 2019 American Chemical Society.

organic linkers with the hydroxyl ion groups and coordinated water in $ZrOCl_2{\cdot}8H_2O$, and the fact that the six-coordinated Ti was attached with fewer organic linkers compared to the eight-coordinated Zr ions, a high density of defective pores was generated along with the absence of organic linkers. Such a high density of defective extent would allow a large number of unliganded Ti and $-NH_2$ groups to be exposed on the surface as light harvesting and Cr(VI) adsorption sites. Subsequently, under a 300 W xenon lamp irradiation, U-OCl-Ti can be photoexcited to create photogenerated electrons and holes. Then, because of the LMCT (NH_2-BDC to Ti-O-Cr cluster) and MMCT (Ti and Zr species) processes, photogenerated electrons in these processes participated in the reduction of the adsorbed Cr(VI) (Fig. 14b). In addition, this research group has also demonstrated that defect rich UiO-66 synthesized by using $ZrOCl_2{\cdot}8H_2O$ as Zr precursor and without solvent-assisted synthesis conditions was effectively useful for adsorbtion and photocatalytic reduction of Cr(VI) [108]. Due to H_2BDC linker can only substitute part of $ZrOCl_2{\cdot}8H_2O$'s hydroxyl ion groups and the coordinated water and the dissolution of organic linkers without the help of organic solvents, defect rich UiO-66 can be obtained, exposing more –OH and $-OH_2$ groups for the adsorption of Cr(VI) [240,241]. What's more, the positively charged UiO-66 samples can further adsorb anionic Cr(VI) ions ($HCrO_4^-$ and $Cr_2O_7^{2-}$) via electrostatic effects (Fig. 15a). In the photocatalytic process (Fig. 15b), the adsorption of colored Cr(VI) by UiO-66 samples endowed UiO-66 visible light responsive, which was then excited by light to produce charge carriers (electrons and holes), resulting photogenerated electrons to reduce Cr(VI). Subsequently, the reduced cationic Cr(III) can desorb from cationic UiO-66. The prepared defect rich UiO-66 achieved high adsorption and photocatalytic degradation performance of Cr(VI) (89.4 % in 3 h), and remained stable after three consecutive cycles.

For those photocatalysts in the form of micron/nanopowder, it is difficult to achieve separation and recovery in wastewater, which seriously hinders their practical application [242]. In view of this point, Du et al. [243] developed UiO-66-NH_2 membrane photocatalysts on α-Al_2O_3 carriers using a reactive seeding method. The authors found that the Cr(VI) reduction efficiency over UiO-66-NH_2 membrane was slightly lower than UiO-66-NH_2 powder. The authors speculated that this was mainly because the significantly reduced contact area between Cr(VI) and UiO-66-NH_2 membrane compared with the powder form of UiO-66-NH_2. However, after twenty runs, UiO-66-NH_2 membrane could still achieve about 94.1% Cr(VI) photocatalytic reduction efficiency and retain its crystal structure, which demonstrated photocatalysts in the form of membranes was favorable for recyclability and structure stability [244]. In the photocatalytic reduction of Cr(VI), under intermittent visible light irradiation, UiO-66-NH_2 be photoexcited to generate electron-hole pairs. The flat-band potential (-0.83 V vs. Ag/AgCl at pH = 6.8) of UiO-66-NH_2 was more negative than the Cr(VI)/Cr(III) (+0.51 V). Thermodynamically, the reduction of Cr(VI) to Cr(III) can be achieved by photogenerated electrons on the UiO-66-NH_2 membrane. Furthermore, the authors also simulated the environment of the real lake to study the effect of foreign ions for UiO-66-NH_2 membrane on Cr(VI) reduction. The results revealed that the existence of common foreign ions had no significant adverse effect on Cr(VI) reduction for UiO-66-NH_2 membrane, which demonstrated feasibility for future applications in real water environments.

In the photocatalytic process, photogenerated electrons are the main active species for Cr(VI) reduction. Notably, photogenerated holes and the formed •OH might exert a minor reverse effect on Cr(VI) reduction, which could allow Cr(V) to oxidize back to Cr (VI) [238]. In the absence of sacrificial agents, the problem can be solved in another way. Zeng et al. [180] developed Ag_2CO_3@UiO-66-NH_2/GO membranes for the simultaneous removal of organic dyes and Cr(VI), which were self-assembled by vacuum filtration of graphene oxide (GO), UiO-66-NH_2 and Ag_2CO_3 at a membrane surface. The as-prepared membrane can nearly remove all adsorbed Cr(VI) and organic dyes. The removal pathway and mechanism were proposed and confirmed by authors (Fig. 16). Under visible light, the photogenerated electrons at the VB of UiO-66-NH_2 and Ag_2CO_3 will be excited to the CB, and the electrons will inject from Ag_2CO_3 into the VB of UiO-66-NH_2, then consumed by the holes. Of note is that the electrons created on UiO-66-NH_2 could be directly involved in the Cr(VI) reduction, avoiding photocorrosion by Ag_2CO_3. Subsequently, the photogenerated holes on Ag_2CO_3 can be used to directly or indirectly (formation of •OH) oxidize the absorbed organic dyes by hydrogen bonding, electrostatic interaction, and π-π interaction of GO and UiO-66-NH_2 (Fig. 16).

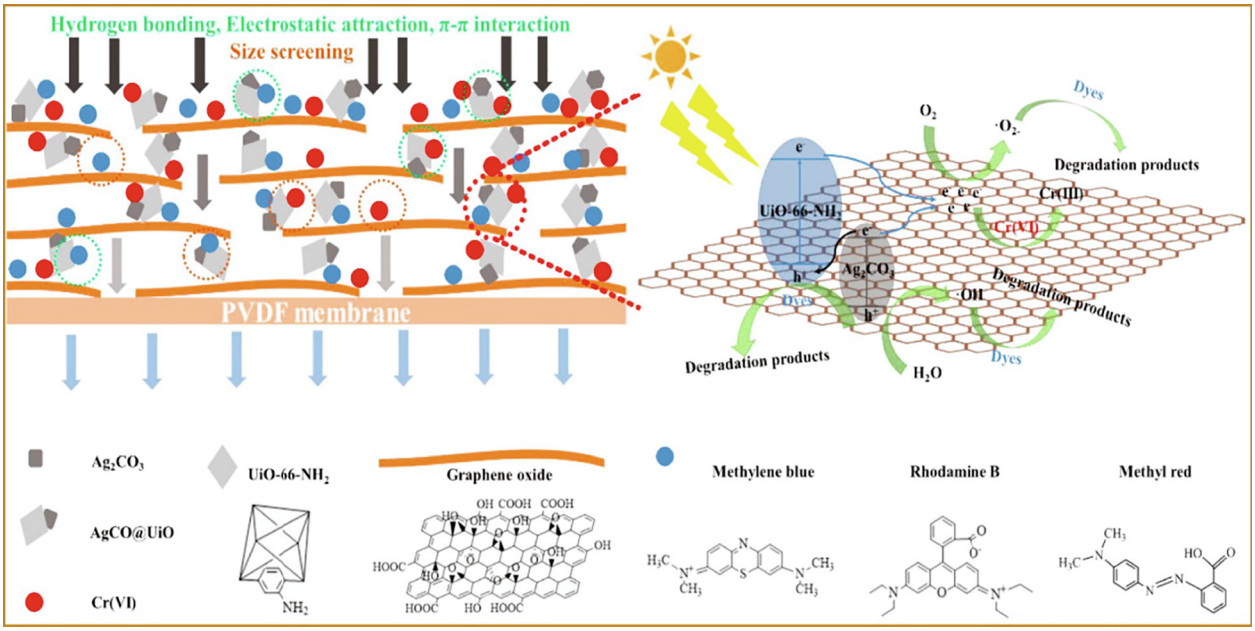

Fig. 16. Schematic diagram of the filtration and photocatalytic mechanism of Ag_2CO_3@UiO-66-NH_2/GO membrane. Adapted with permission from Ref. [180], Copyright 2020 Elsevier.

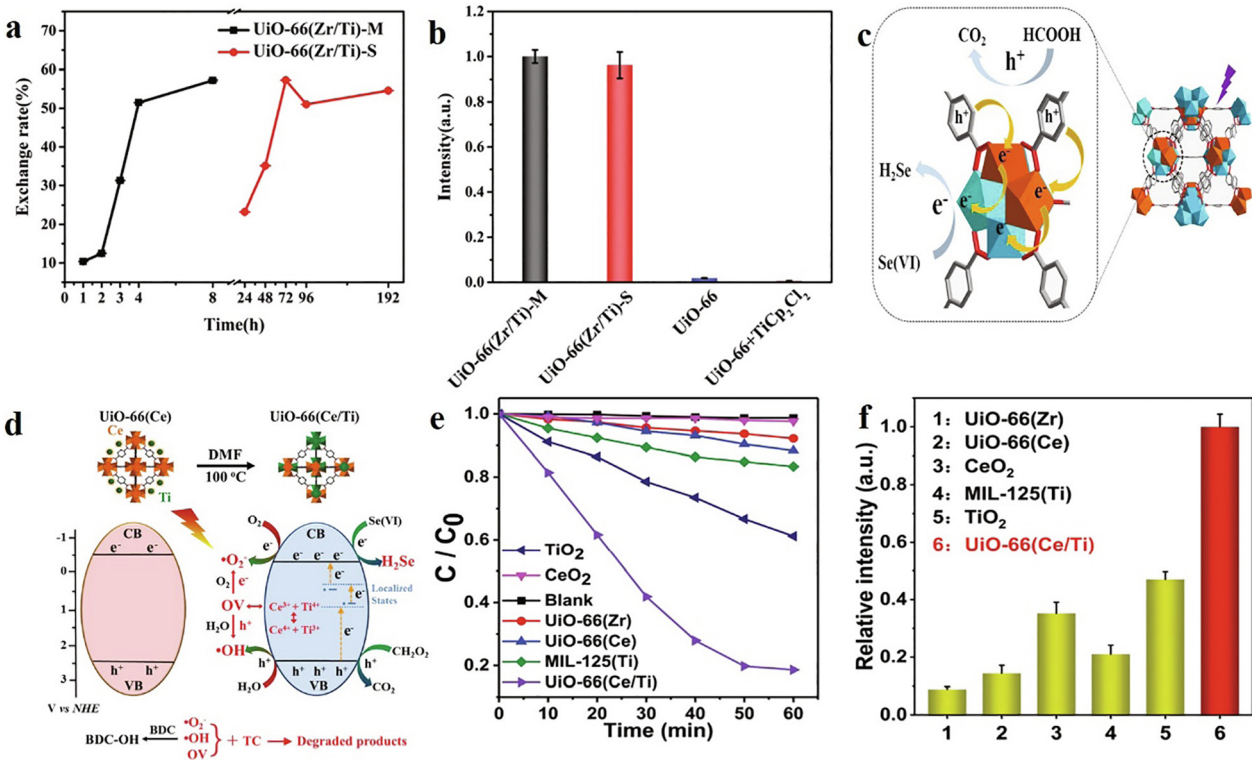

Fig. 17. Schematic illustration of (a) the exchange rate of UiO-66(Zr/Ti)-M and UiO-66(Zr/Ti)-S increasing with the incubation period. (b) atomic fluorescence spectrometry (AFS) intensity obtained from UiO-66(Zr/Ti)-M (obtained after 4 h incubation), UiO-66(Zr/Ti)-S (obtained after 4 d incubation), UiO-66, and the mixture of UiO-66 and $TiCp_2Cl_2$ as photocatalysts for the reduction of Se(VI); (c) the proposed mechanism for the enhanced photocatalytic performance of UiO-66(Zr/Ti)-M; (d) Ti incorporation into UiO-66(Ce) and the corresponding enhancement in photocatalytic activity; (e) time-evolving curve for TC photodegradation and (f) AFS signal intensity of the reduced Se(VI) by using different kinds of photocatalysts. Adapted with permission from Ref. [41,91], Copyright 2017 and 2019, The Royal Society of Chemistry.

What's more, $\bullet O_2^-$ can also act as active components to participate in organic dyes degradation. In this way, both organic dyes and Cr (VI) are removed simultaneously, while effectively avoiding Cr(V) to oxidize back to Cr(VI). The experimental results indicated that the removal efficiency of Cr(VI) and dyes by Ag_2CO_3@UiO-66-NH_2/GO membrane under light conditions was almost 100%.

Selenium(Se) is an essential nutrient, but excessive intake may pose a health risk and cause alkali or other diseases [89]. The reduction capacity exhibited by the modified UiO-66 has been applied to the photoreduction of Se(VI) for environmental remediation. Tu et al. [41] employed a microwave-assisted approach to substitute Zr in UiO-66 with Ti (UiO-66(Zr/Ti)-M) and used it for the reduction of Se(VI). Although the microwave-assisted synthesis of UiO-66(Zr/Ti)-M had similar photocatalytic activity to that of the conventional high energy-consuming synthesis of UiO-66(Zr/Ti) from solvothermal approach (UiO-66(Zr/Ti)-S), UiO-66(Zr/Ti)-M required less synthesis time and was highly promising in terms of practical utility (Fig. 17a, b). The exchange rate of UiO-66(Zr/Ti)-S was only about 35% after 2 d and still below 60% after 8 d, while UiO-66(Zr/Ti)-M surprisingly reached>50% after 4 h. Notably, UiO-66(Zr/Ti)-M with the introduction of Ti exhibited vastly better photocatalytic reduction of Se(VI) than the negligible activity of UiO-66 (Fig. 17b). Specifically, the incorporation of Ti could act as an electron trap to effectively capture photogenerated electrons to improve the LMCT from photoexcited H_2BDC to Zr oxo clusters. Furthermore, based on Ti incorporation, the group [91] also introduced Ti into UiO-66 with Ce as the metal node (UiO-66(Ce/Ti)) to obtain significantly enhanced photocatalytic efficiency for TC degradation and Se(VI) reduction. The authors found that the introduction of Ti in UiO-66(Ce) induced the formation of OV due to the Ce–Ti synergistic effect ($Ce^{4+} + Ti^{3+} \leftrightarrow Ce^{3+} + Ti^{4+} + OV$). Specially, to balance intrinsic Ti^{3+} defect in electrical charge, the lattice oxygen will be removed to form OVs, which can trap the electron from Ti^{3+} to form Ti^{4+}, and Ti^{4+} also can be reduced to Ti^{3+} upon electron donor (Ce^{3+}) and light irradiation. The OV can could as a capture center for electron and hole and facilitate the formation of oxidative $\bullet O_2^-$ and •OH. Subsequently, UiO-66(Ce/Ti) showed better degradation efficiency than the other samples, with more than 80% of the TC degraded within 1 h (Fig. 17e). Additionally, OV could also bring in local states lower than CB (Fig. 17d), which were very beneficial for LMCT. Because of the greatly enhanced LMCT, the photogenerated electrons in UiO-66(Ce/Ti) performed the reduction of Se(VI) with higher efficiency than other samples (Fig. 17f).

5. Conclusion and outlooks

Due to the remarkable characteristics, intrinsic photocatalytic activity, remarkable thermal and chemical stability of UiO-66, its related research has achieved its flourishing stage. In this review, the functional modifications of UiO-66 and the applications of modified UiO-66 for photocatalytic CO_2 reduction, hydrogen generation, removal of organic pollutants, and Cr(VI) reduction were summarized and discussed in detail. Because UiO-66 suffers from inefficient photocatalysis, various approaches have been used to modify UiO-66 to form effective photocatalysts, including selecting functional metal nodes or organic linkers, defect engineering, metal modifications, constructing dye sensitization system, combing with other photoactive semiconductors. The principles for designing and modifying UiO-66 to perform in photocatalytic reactions could be clearly illustrated as follows: (a) the permanent pores and larger specific surface area of UiO-66 could increase

the concentration of adsorption and reaction active sites; (b) various modifications could boost the sunlight utilization of UiO-66; and (c) tight interfacial connections between UiO-66 and the photofunctional components can offer widespread channels for transfer and separation of charge carriers. As a result, modified UiO-66 photocatalysts often demonstrate significantly outperformance of single UiO-66.

During the last few years, various modified UiO-66 photocatalysts for the CO_2 reduction, hydrogen production, removal of organic pollutants, and Cr(VI) reduction have been developed. With their striking advantages such as permanent pores, larger specific surface area, abundant active sites, thermochemical stability and effective charge separation, they will present a distinct window for developing robust photocatalysts. Although considerable progresses have been made in the field of photocatalysis based on UiO-66 materials, the practical applications of these photocatalysts are still limited. In order to enable the widespread application of these materials in practical production, it deserves great consideration to the following challenges in the future.

(1) Much of the work in this research area has been conducted through laboratory-scale experiments that typically used Xe lamps (light cut k > 420 nm) as the light source. And laboratory-scale experiments are often only single target substance, which is mild and comfortable for the modified UiO-66 photocatalyst to perform its catalytic action. However, it is worth noting that photocatalysts may have different photocatalytic efficiency in actual sunlight, with other co-existing ions, at different pH, and in complex environments than those demonstrated in the laboratory. It is also noted that in most cases, only a few photocatalysts were used. Therefore, considerable efforts are still needed to achieve practical applications for modified UiO-66 photocatalysts.

(2) Diverse sacrificial electron donors have been widely applied to nearly all published systems about modified UiO-66 photocatalysts for photocatalytic applications. On the one hand, it would be fascinating to unveil the effects of sacrificial agents and their reaction products on the photocatalytic ability of modified UiO-66 photocatalysts. On the other hand, careful consideration should be given to the selection of sacrificial agents that are low-cost, plentiful and sustainably available.

(3) Co-catalysts are an essential component of many photocatalytic systems. Noble-metals, such as Pt, Au and Pd, have been considered as a viable co-catalyst for a wide range of photocatalytic systems. However, photocatalysts using noble-metals as co-catalysts are still challenging to scale up for synthesis and cost for practical applications. Several other types of co-catalysts, such as MoS_2, reduced graphene oxide, have been used in visible light responsive photocatalytic systems to demonstrate their potential for practical applications. In further studies, the development of noble-metal-free co-catalysts should be emphasized to better understand their role in photocatalytic systems.

(4) Some theoretical insights are necessary in the exploration of the reaction mechanism. The redox potential of the target reactants should be given for further comparison with the correspondingly modified UiO-66 to show that the reaction is thermodynamically feasible. However, these aspects are somewhat vague and underexplored in some of the current research work. Additionally, there are also few investigations on the mechanism of water-splitting and CO_2 photoreduction in modified UiO-66, especially the current perception of the photogenerated charge transfer and photocatalytic reaction paths remains ambiguous. Specifically, it would be a great leap forward in understanding the mechanism of photocatalysis if further and more direct evidence of the actual photogenerated charge transfer process could be found. What's more, it is also critical to understand the product distribution, electronic structure and structural property relationships in modified UiO-66 with high charge utilization efficiency by DFT calculations.

(5) UiO-66-based photocatalysts are currently at their infancy and possess tremendous opportunities in future energy renewable and environmental remediation. Notably, the construction of multifunctional photocatalysts is an exciting but challenging task, implying that both oxidation and reduction reactions should occur simultaneously in a single system. So far, photoreduction of Cr (VI) and oxidation of alcohols and, hydrogen generation and CO_2 reduction have been achieved in one photocatalytic system. Multifunctional UiO-66-based photocatalysts are desirable for more types of reactions in one system.

(6) Modification of organic linkers of UiO-66 with electron-donating groups has been shown to enhance light absorption, while existing studies have been limited to the effect of a single functional group on the photoactivity of UiO-66. Increasing the number of functional groups on each linker to improve this effect, as well as determining the appropriate number of functional groups on each H_2BDC to achieve optimal performance, could be considered in the future.

(7) Partial or total metal substitution with metals such as Ti, Ce, etc. in the $Zr_6O_4(OH)_4$ metal cluster of UiO-66 is a promising modification method to adjust the band gap, the LMCT and the degree of hybridization between the metal and the organic linker. However, the effect of the number and position of individual metals in the metal cluster on the photoactivity of UiO-66 is still unknown. In the future, precise tuning of the position and number of metal centers (e.g., $Zr_mTi_nCe_{6-m-n}O_4(OH)_4$) can be carried out theoretically and experimentally to achieve targeted optimization of key electronic structure parameters. Furthermore, after tuning the metal nodes, other modifications can be further utilized to enhance the photocatalytic activity, including functionalization of organic linkers, photosensitization, and introduction of photoactive substances.

(8) Most modified UiO-66 photocatalysts are applied in powder form for photocatalytic reactions, which poses challenges for large-scale processes related to recovery efficiency and stability. Notably, some studies related to the modification of UiO-66 into membrane photocatalysts have been reported, which are more suitable for large-scale applications than powder photocatalysts. Membrane photocatalysts are not only similar to powders in terms of photocatalytic efficiency, but also retain their activity and structural integrity after recycled many times in photocatalytic reaction systems. Therefore, the development of more efficient membrane photocatalysts could be considered in the future.

(9) Several faster, solvent-free and energy-efficient approaches to the synthesis of UiO-66 compared to conventional solvothermal method have been reported, such as microwave-assisted, electrochemical film deposition, mechanochemical and so on. These approaches have the potential to increase the widespread availability of UiO-66, but few studies have actually been applied to the synthesis of highly efficient modified UiO-66. It is necessary to explore these synthetic approaches to achieve industrial production of modified UiO-66. In addition, these convenient, efficient approaches methods could be adapted to the synthesis of other types of microporous MOFs to improve their practical accessibility.

Declaration of Competing Interest

The authors declare that they have no known competing financial interests or personal relationships that could have appeared to influence the work reported in this paper.

Acknowledgements

This study was financially supported by the Program for the National Natural Science Foundation of China (51909084, 51909085, 51979103), China Postdoctoral Science Foundation Funded Project (2018M642977), the Natural Science Foundation of Hunan Province, China (2020JJ5055, 2020JJ5069), and the Fundamental Research Funds for the Central Universities (531118010247).

References

[1] W. Wang, X. Xu, W. Zhou, Z. Shao, Adv. Sci. 4 (2017) 1600371, https://doi.org/10.1002/advs.201600371.
[2] P. Zhang, S.B. Wang, B.Y. Guan, X.W. Lou, Energy Environ. Sci. 12 (2019) 164–168, https://doi.org/10.1039/c8ee02538j.
[3] X. Li, X. Yang, H. Xue, H. Pang, Q. Xu, EnergyChem 2 (2020), https://doi.org/10.1016/j.enchem.2020.100027 100027.
[4] G. Liu, Y. Sheng, J.W. Ager, M. Kraft, R. Xu, EnergyChem 1 (2019), https://doi.org/10.1016/j.enchem.2019.100014 100014.
[5] Q. Yang, Y.-H. Wang, Y. Qiao, M. Gau, P.J. Carroll, P.J. Walsh, E.J. Schelter, Science 372 (2021) 847–852, https://doi.org/10.1126/science.abd8408.
[6] S. Wang, B.Y. Guan, X. Wang, X.W.D. Lou, J. Am. Chem. Soc. 140 (2018) 15145–15148, https://doi.org/10.1021/jacs.8b07721.
[7] S. Zhang, H. Ye, J. Hua, H. Tian, EnergyChem 1 (2019), https://doi.org/10.1016/j.enchem.2019.100015 100015.
[8] Y. Park, S. Kim, L. Tian, H. Zhong, G.D. Scholes, P.J. Chirik, Nat. Chem. 13 (2021) 969–976, https://doi.org/10.1038/s41557-021-00732-z.
[9] A. Fujishima, K. Honda, Nature 238 (1972) 37–38, https://doi.org/10.1038/238037a0.
[10] O.M. Yaghi, M. O'Keeffe, N.W. Ockwig, H.K. Chae, M. Eddaoudi, J. Kim, Nature 423 (2003) 705–714, https://doi.org/10.1038/nature01650.
[11] T. Luo, L. Li, Y. Chen, J. An, C. Liu, Z. Yan, J.H. Carter, X. Han, A.M. Sheveleva, F. Tuna, E.J.L. McInnes, C.C. Tang, M. Schroder, S. Yang, Nat. Commun. 12 (2021) 3583, https://doi.org/10.1038/s41467-021-23302-w.
[12] R. Zhu, J. Ding, L. Jin, H. Pang, Coord. Chem. Rev. 389 (2019) 119–140, https://doi.org/10.1016/j.ccr.2019.03.002.
[13] X. Li, Q.-L. Zhu, EnergyChem 2 (2020), https://doi.org/10.1016/j.enchem.2020.100033 100033.
[14] H.C. Zhou, S. Kitagawa, Chem. Soc. Rev. 43 (2014) 5415–5418, https://doi.org/10.1039/c4cs90059f.
[15] Z. Liang, R. Zhao, T. Qiu, R. Zou, Q. Xu, EnergyChem 1 (2019), https://doi.org/10.1016/j.enchem.2019.100001 100001.
[16] X. Xiao, G. Zhang, Y. Xu, H. Zhang, X. Guo, Y. Liu, H. Pang, J. Mater. Chem. A 7 (2019) 17266–17271, https://doi.org/10.1039/c9ta05409j.
[17] G. Zhang, L. Jin, R. Zhang, Y. Bai, R. Zhu, H. Pang, Coord. Chem. Rev. 439 (2021), https://doi.org/10.1016/j.ccr.2021.213915 213915.
[18] J.H. Cavka, S. Jakobsen, U. Olsbye, N. Guillou, C. Lamberti, S. Bordiga, K.P. Lillerud, J. Am. Chem. Soc. 130 (2008) 13850–13851, https://doi.org/10.1021/ja8057953.
[19] M. Ding, R.W. Flaig, H.-L. Jiang, O.M. Yaghi, Chem. Soc. Rev. 48 (2019) 2783–2828, https://doi.org/10.1039/c8cs00829a.
[20] R. Li, W. Zhang, K. Zhou, Adv. Mater. 30 (2018) 1705512, https://doi.org/10.1002/adma.201705512.
[21] Y. Liu, C. Tang, M. Cheng, M. Chen, S. Chen, L. Lei, Y. Chen, H. Yi, Y. Fu, L. Li, ACS Catal. 11 (2021) 13374–13396, https://doi.org/10.1021/acscatal.1c03866.
[22] Z.B. Liang, C. Qu, D.G. Xia, R.Q. Zou, Q. Xu, Angew. Chem. Int. Ed. 57 (2018) 9604–9633, https://doi.org/10.1002/anie.201800269.
[23] E.-X. Chen, M. Qiu, Y.-F. Zhang, L. He, Y.-Y. Sun, H.-L. Zheng, X. Wu, J. Zhang, Q. Lin, Angew. Chem. Int. Ed. 60 (2021) 2–9, https://doi.org/10.1002/anie.202111622.
[24] J.R. Choi, T. Tachikawa, M. Fujitsuka, T. Majima, Langmuir 26 (2010) 10437–10443, https://doi.org/10.1021/la101770h.
[25] M. Alvaro, E. Carbonell, B. Ferrer, F.X. Llabres i Xamena, H. Garcia, Chemistry-a European Journal, 13 (2007) 5106-5112. 10.1002/chem.200601003.
[26] F.X.L.i. Xamena, A. Corma, H. Garcia, J. Phys. Chem. C, 111 (2007) 80-85. 10.1021/jp063600e.
[27] P. Tian, X. He, W.X. Li, L. Zhao, W. Fang, H. Chen, F.Q. Zhang, W.Q. Zhang, W. Wang, J. Mater. Sci., 53 (2018) 12016-12029. 10.1007/s10853-018-2476-0.
[28] S. Mandal, S. Natarajan, P. Mani, A. Pankajakshan, Adv. Funct. Mater. 31 (2021) 2006291, https://doi.org/10.1002/adfm.202006291.
[29] C.G. Silva, I. Luz, F.X. Llabres i Xamena, A. Corma, H. Garcia, Chemistry-a European Journal, 16 (2010) 11133-11138. 10.1002/chem.200903526.
[30] Z. Ren, X. Liu, Z. Zhuge, Y. Gong, C.Q. Sun, Chin. J. Catal. 41 (2020) 180–187, https://doi.org/10.1016/s1872-2067(19)63484-4.
[31] Z. Zhuge, X. Liu, T. Chen, Y. Gong, C. Li, L. Niu, S. Xu, X. Xu, Z.A. Alothman, C.Q. Sun, J.G. Shapter, Y. Yamauchi, Chem. Eng. J. 421 (2021), https://doi.org/10.1016/j.cej.2020.127838 127838.
[32] X. Liu, B. Liu, L. Li, Z. Zhuge, P. Chen, C. Li, Y. Gong, L. Niu, J. Liu, L. Lei, C.Q. Sun, Appl. Catal., B, 249 (2019) 82-90. 10.1016/j.apcatb.2019.02.061.
[33] X. Liu, T. Chen, Y. Gong, C. Li, L. Niu, S. Xu, X. Xu, L. Pan, J.G. Shapter, Y. Yamauchi, J. Na, M. Eguchi, J. Photochem. Photobiol., C 47 (2021), https://doi.org/10.1016/j.jphotochemrev.2021.100404 100404.
[34] J. Canivet, A. Fateeva, Y. Guo, B. Coasne, D. Farrusseng, Chem. Soc. Rev. 43 (2014) 5594–5617, https://doi.org/10.1039/C4CS00078A.
[35] J. Gascon, F. Kapteijn, Angew. Chem. Int. Ed. 49 (2010) 1530–1532, https://doi.org/10.1002/anie.200906491.
[36] S.J. Garibay, S.M. Cohen, Chem. Commun. 46 (2010) 7700–7702, https://doi.org/10.1039/C0CC02990D.
[37] A. Dhakshinamoorthy, A.M. Asiri, H. Garcia, Angew. Chem. Int. Ed. 55 (2016) 5414–5445, https://doi.org/10.1002/anie.201505581.
[38] J. He, Y. Zhang, J. He, X. Zeng, X. Hou, Z. Long, Chem. Commun. 54 (2018) 8610–8613, https://doi.org/10.1039/C8CC04891F.
[39] T. He, S. Chen, B. Ni, Y. Gong, Z. Wu, L. Song, L. Gu, W. Hu, X. Wang, Angew. Chem. Int. Ed. 57 (2018) 3493–3498, https://doi.org/10.1002/anie.201800817.
[40] Y. Horiuchi, T. Toyao, M. Saito, K. Mochizuki, M. Iwata, H. Higashimura, M. Anpo, M. Matsuoka, J. Phys. Chem. C 116 (2012) 20848–20853, https://doi.org/10.1021/jp3046005.
[41] J. Tu, X. Zeng, F. Xu, X. Wu, Y. Tian, X. Hou, Z. Long, Chem. Commun. 53 (2017) 3361–3364, https://doi.org/10.1039/c7cc00076f.
[42] T.-F. Chen, S.-Y. Han, Z.-P. Wang, H. Gao, L.-Y. Wang, Y.-H. Deng, C.-Q. Wan, Y. Tian, Q. Wang, G. Wang, G.-S. Li, Appl. Catal., B, 259 (2019) 118047. doi: 10.1016/j.apcatb.2019.118047.
[43] Y. Gao, J. Lu, J. Xia, G. Yu, ACS Appl. Mater. Interfaces 12 (2020) 12706–12716, https://doi.org/10.1021/acsami.9b21122.
[44] F.-M. Zhang, J.-L. Sheng, Z.-D. Yang, X.-J. Sun, H.-L. Tang, M. Lu, H. Dong, F.-C. Shen, J. Liu, Y.-Q. Lan, Angew. Chem. Int. Ed. 57 (2018) 12106–12110, https://doi.org/10.1002/anie.201806862.
[45] Y. Sun, L. Sun, D. Feng, H.-C. Zhou, Angew. Chem. Int. Ed. 55 (2016) 6471–6475, https://doi.org/10.1002/anie.201602274.
[46] Y. Liu, H. Cheng, M. Cheng, Z. Liu, D. Huang, G. Zhang, B. Shao, Q. Liang, S. Luo, T. Wu, S. Xiao, Chem. Eng. J. 417 (2020), https://doi.org/10.1016/j.cej.2020.127914 127914.
[47] S. Wang, X. Wang, Small 11 (2015) 3097–3112, https://doi.org/10.1002/smll.201500084.
[48] L. Zeng, X. Guo, C. He, C. Duan, ACS Catal. 6 (2016) 7935–7947, https://doi.org/10.1021/acscatal.6b02228.
[49] G. Zhang, D. Huang, M. Cheng, L. Lei, S. Chen, R. Wang, W. Xue, Y. Liu, Y. Chen, Z. Li, J. Mater. Chem. A 8 (2020) 17883–17906, https://doi.org/10.1039/d0ta05662f.
[50] D. Huang, G. Wang, M. Cheng, G. Zhang, S. Chen, Y. Liu, Z. Li, W. Xue, L. Lei, R. Xiao, Chem. Eng. J. 421 (2020), https://doi.org/10.1016/j.cej.2020.127817 127817.
[51] N. Kolobov, M.G. Goesten, J. Gascon, Angew. Chem. Int. Ed. 60 (2021) 2–17, https://doi.org/10.1002/anie.202106342.
[52] L. Shen, S. Liang, W. Wu, R. Liang, L. Wu, Dalton Trans. 42 (2013) 13649–13657, https://doi.org/10.1039/c3dt51479j.
[53] L. Shen, W. Wu, R. Liang, R. Lin, L. Wu, Nanoscale 5 (2013) 9374–9382, https://doi.org/10.1039/c3nr03153e.
[54] D. Sun, Y. Fu, W. Liu, L. Ye, D. Wang, L. Yang, X. Fu, Z. Li, Chemistry-a European Journal 19 (2013) 14279–14285, https://doi.org/10.1002/chem.201301728.
[55] P. Hu, R. Wang, Z. Gao, S. Jiang, Z. Zhao, H. Ji, Z. Zhao, Appl. Catal., B, 296 (2021) 120371. 10.1016/j.apcatb.2021.120371.
[56] M. Xu, D. Li, K. Sun, L. Jiao, C. Xie, C. Ding, H.L. Jiang, Angew. Chem. Int. Ed. 60 (2021) 16372–16376, https://doi.org/10.1002/anie.202104219.
[57] L.W. Chen, Y.C. Hao, Y. Guo, Q. Zhang, J. Li, W.Y. Gao, L. Ren, X. Su, L. Hu, N. Zhang, S. Li, X. Feng, L. Gu, Y.W. Zhang, A.X. Yin, B. Wang, J. Am. Chem. Soc. 143 (2021) 5727–5736, https://doi.org/10.1021/jacs.0c13342.
[58] Y. Feng, Q. Chen, M. Jiang, J. Yao, Ind. Eng. Chem. Res. 58 (2019) 17646–17659, https://doi.org/10.1021/acs.iecr.9b03188.
[59] D. Zou, D. Liu, Mater. Today Chem. 12 (2019) 139–165, https://doi.org/10.1016/j.mtchem.2018.12.004.
[60] W. Xiang, Y. Zhang, Y. Chen, C.-J. Liu, X. Tu, J. Mater. Chem. A 8 (2020) 21526–21546, https://doi.org/10.1039/d0ta08009h.
[61] A. Melillo, M. Cabrero-Antonino, S. Navalon, M. Alvaro, B. Ferrer, H. Garcia, Appl. Catal., B, 278 (2020). 10.1016/j.apcatb.2020.119345.
[62] V. Guillerm, S. Gross, C. Serre, T. Devic, M. Bauer, G. Ferey, Chem. Commun. 46 (2010) 767–769, https://doi.org/10.1039/b914919h.
[63] K. Tulig, K.S. Walton, RSC Adv. 4 (2014) 51080–51083, https://doi.org/10.1039/c4ra08856e.
[64] M.R. DeStefano, T. Islamoglu, S.J. Garibay, J.T. Hupp, O.K. Farha, Chem. Mater. 29 (2017) 1357–1361, https://doi.org/10.1021/acs.chemmater.6b05115.
[65] K. Uzarevic, T.C. Wang, S.Y. Moon, A.M. Fidelli, J.T. Hupp, O.K. Farha, T. Friscic, Chem. Commun. 52 (2016) 2133–2136, https://doi.org/10.1039/c5cc08972g.
[66] I. Stassen, M. Styles, T. Van Assche, N. Campagnol, J. Fransaer, J. Denayer, J.-C. Tan, P. Falcaro, D. De Vos, R. Ameloot, Chem. Mater. 27 (2015) 1801–1807, https://doi.org/10.1021/cm504806p.
[67] H.-Q. Xu, S. Yang, X. Ma, J. Huang, H.-L. Jiang, ACS Catal. 8 (2018) 11615–11621, https://doi.org/10.1021/acscatal.8b03233.
[68] Y. Bai, Y. Dou, L.-H. Xie, W. Rutledge, J.-R. Li, H.-C. Zhou, Chem. Soc. Rev. 45 (2016) 2327–2367, https://doi.org/10.1039/C5CS00837A.
[69] J. Winarta, B. Shan, S.M. McIntyre, L. Ye, C. Wang, J. Liu, B. Mu, Cryst. Growth Des. 20 (2020) 1347–1362, https://doi.org/10.1021/acs.cgd.9b00955.
[70] C.G. Piscopo, A. Polyzoidis, M. Schwarzer, S. Loebbecke, Microporous Mesoporous Mater. 208 (2015) 30–35, https://doi.org/10.1016/j.micromeso.2015.01.032.
[71] X. Xu, R. Liu, Y. Cui, X. Liang, C. Lei, S. Meng, Y. Ma, Z. Lei, Z. Yang, Appl. Catal., B, 210 (2017) 484-494. 10.1016/j.apcatb.2017.04.021.

[72] M.A. Nasalevich, C.H. Hendon, J.G. Santaclara, K. Svane, B. van der Linden, S.L. Veber, M.V. Fedin, A.J. Houtepen, M.A. van der Veen, A. Walsh, J. Gascon, Sci. Rep. 6 (2016) 23676, https://doi.org/10.1038/srep23676.
[73] Y. Lee, S. Kim, J.K. Kang, S.M. Cohen, Chem. Commun. 51 (2015) 5735–5738, https://doi.org/10.1039/c5cc00686d.
[74] L. Shen, R. Liang, M. Luo, F. Jing, L. Wu, PCCP 17 (2015) 117–121, https://doi.org/10.1039/c4cp04162c.
[75] K. Hendrickx, D.E.P. Vanpoucke, K. Leus, K. Lejaeghere, A. Van Yperen-De Deyne, V. Van Speybroeck, P. Van Der Voort, K. Hemelsoet, Inorg. Chem. 54 (2015) 10701–10710, https://doi.org/10.1021/acs.inorgchem.5b01593.
[76] X. Mu, J. Jiang, F. Chao, Y. Lou, J. Chen, Dalton Trans. 47 (2018) 1895–1902, https://doi.org/10.1039/c7dt04477a.
[77] F. Mu, Q. Cai, H. Hu, J. Wang, Y. Wang, S. Zhou, Y. Kong, Chem. Eng. J. 384 (2020), https://doi.org/10.1016/j.cej.2019.123352 123352.
[78] S. Mao, Y. Zou, G. Sun, L. Zeng, Z. Wang, D. Ma, Y. Guo, Y. Cheng, C. Wang, J.-W. Shi, J. Colloid Interface Sci. 581 (2021) 1–10, https://doi.org/10.1016/j.jcis.2020.07.121.
[79] A. Wang, Y. Zhou, Z. Wang, M. Chen, L. Sun, X. Liu, RSC Adv. 6 (2016) 3671–3679, https://doi.org/10.1039/c5ra24135a.
[80] D. Sun, W. Liu, M. Qiu, Y. Zhang, Z. Li, Chem. Commun. 51 (2015) 2056–2059, https://doi.org/10.1039/c4cc09407g.
[81] Y. Feng, Q. Chen, M. Cao, N. Ling, J. Yao, A.C.S. Appl, Nano Mater. 2 (2019) 5973–5980, https://doi.org/10.1021/acsanm.9b01403.
[82] A. Santiago Portillo, H.G. Baldoví, M.T. García Fernandez, S. Navalón, P. Atienzar, B. Ferrer, M. Alvaro, H. Garcia, Z. Li, J. Phys. Chem. C, 121 (2017) 7015-7024. 10.1021/acs.jpcc.6b13068.
[83] X.P. Wu, L. Gagliardi, D.G. Truhlar, J. Am. Chem. Soc. 140 (2018) 7904–7912, https://doi.org/10.1021/jacs.8b03613.
[84] K. Hendrickx, J.J. Joos, A. De Vos, D. Poelman, P.F. Smet, V. Van Speybroeck, P. Van Der Voort, K. Lejaeghere, Inorg. Chem. 57 (2018) 5463–5474, https://doi.org/10.1021/acs.inorgchem.8b00425.
[85] D. Zhao, C. Cai, Dyes Pigm. 185 (2021), https://doi.org/10.1016/j.dyepig.2020.108957 108957.
[86] X. Qiu, Y. Zhu, X. Zhang, Y. Zhang, L.T. Menisa, C. Xia, S. Liu, Z. Tang, Solar RRL 4 (2019), https://doi.org/10.1002/solr.201900449.
[87] Y. Xiong, S. Chen, F. Ye, L. Su, C. Zhang, S. Shen, S. Zhao, Chem. Commun. 51 (2015) 4635–4638, https://doi.org/10.1039/c4cc10346g.
[88] M. Lammert, M.T. Wharmby, S. Smolders, B. Bueken, A. Lieb, K.A. Lomachenko, D. De Vos, N. Stock, Chem. Commun. 51 (2015) 12578–12581, https://doi.org/10.1039/c5cc02606g.
[89] Y. Zhang, X. Zeng, X. Jiang, H. Chen, Z. Long, Microchem. J. 149 (2019), https://doi.org/10.1016/j.microc.2019.103967 103967.
[90] M. Campanelli, T. Del Giacco, F. De Angelis, E. Mosconi, M. Taddei, F. Marmottini, R. D'Amato, F. Costantino, ACS Appl. Mater. Interfaces 11 (2019) 45031–45037, https://doi.org/10.1021/acsami.9b13730.
[91] Y.J. Zhang, H.J. Chen, Y. Pan, X.L. Zeng, X.F. Jiang, Z. Long, X.D. Hou, Chem. Commun. 55 (2019) 13959–13962, https://doi.org/10.1039/c9cc06562h.
[92] K. An, H. Ren, D. Yang, Z. Zhao, Y. Gao, Y. Chen, J. Tan, W. Wang, Z. Jiang, Appl. Catal., B, 292 (2021) 120167. 10.1016/j.apcatb.2021.120167.
[93] X. Ma, L. Wang, Q. Zhang, H.-L. Jiang, Angew. Chem. Int. Ed. 58 (2019) 12175–12179, https://doi.org/10.1002/anie.201907074.
[94] D.F. Yan, Y.X. Li, J. Huo, R. Chen, L.M. Dai, S.Y. Wang, Adv. Mater. 29 (2017) 1606459, https://doi.org/10.1002/adma.201606459.
[95] W. Zhou, H.G. Fu, Inorg. Chem. Front. 5 (2018) 1240–1254, https://doi.org/10.1039/c8qi00122g.
[96] P. Yang, H. Zhuzhang, R. Wang, W. Lin, X. Wang, Angew. Chem. Int. Ed. 58 (2019) 1134–1137, https://doi.org/10.1002/anie.201810648.
[97] A. Walsh, A. Zunger, Nat. Mater. 16 (2017) 964–967, https://doi.org/10.1038/nmat4973.
[98] S. Ling, B. Slater, Chem. Sci. 7 (2016) 4706–4712, https://doi.org/10.1039/C5SC04953A.
[99] A. Koutsianos, E. Kazimierska, A.R. Barron, M. Taddei, E. Andreoli, Dalton Trans. 48 (2019) 3349–3359, https://doi.org/10.1039/C9DT00154A.
[100] L. Van Nhieu, V. The Ky, K.S. Yoo, J. Kim, Sep. Purif. Technol., 274 (2021) 119079. 10.1016/j.seppur.2021.119079.
[101] H. Wu, Y.S. Chua, V. Krungleviciute, M. Tyagi, P. Chen, T. Yildirim, W. Zhou, J. Am. Chem. Soc. 135 (2013) 10525–10532, https://doi.org/10.1021/ja404514r.
[102] G. Ye, H. Wang, X. Zeng, L. Wang, J. Wang, Appl. Catal., B, 299 (2021) 120659. 10.1016/j.apcatb.2021.120659.
[103] Y. Jiao, Y. Liu, G. Zhu, J.T. Hungerford, S. Bhattacharyya, R.P. Lively, D.S. Sholl, K.S. Walton, J. Phys. Chem. C 121 (2017) 23471–23479, https://doi.org/10.1021/acs.jpcc.7b07772.
[104] B. Bueken, N. Van Velthoven, A. Krajnc, S. Smolders, F. Taulelle, C. Mellot-Draznieks, G. Mali, T.D. Bennett, D. De Vos, Chem. Mater. 29 (2017) 10478–10486, https://doi.org/10.1021/acs.chemmater.7b04128.
[105] A. De Vos, K. Hendrickx, P. Van der Voort, V. Van Speybroeck, K. Lejaeghere, Chem. Mater. 29 (2017) 3006–3019, https://doi.org/10.1021/acs.chemmater.6b05444.
[106] M. Taddei, G.M. Schukraft, M.E.A. Warwick, D. Tiana, M.J. McPherson, D.R. Jones, C. Petit, J. Mater. Chem. A 7 (2019) 23781–23786, https://doi.org/10.1039/c9ta05216j.
[107] Y. Fu, J. Wu, R. Du, K. Guo, R. Ma, F. Zhang, W. Zhu, M. Fan, RSC Adv. 9 (2019) 37733–37738, https://doi.org/10.1039/c9ra08097j.
[108] Q. Chen, Y. Feng, R. Tian, J. Chen, A. Wang, J. Yao, Ind. Eng. Chem. Res. 58 (2019) 21562–21568, https://doi.org/10.1021/acs.iecr.9b05464.
[109] W. Gao, X. Li, X. Zhang, S. Su, S. Luo, R. Huang, Y. Jing, M. Luo, Nanoscale 13 (2021) 7801–7809, https://doi.org/10.1039/d1nr00697e.
[110] W.Y. Lin, H. Frei, J. Am. Chem. Soc. 127 (2005) 1610–1611, https://doi.org/10.1021/ja040162l.
[111] R. Nakamura, A. Okamoto, H. Osawa, H. Irie, K. Hashimoto, J. Am. Chem. Soc. 129 (2007) 9596–9597, https://doi.org/10.1021/ja073668n.
[112] S. Mao, J.-W. Shi, G. Sun, Y. Zhang, X. Ji, Y. Lv, B. Wang, Y. Xu, Y. Cheng, Chem. Eng. J. 404 (2021), https://doi.org/10.1016/j.cej.2020.126533 126533.
[113] Z. Yang, X. Xu, X. Liang, C. Lei, L. Gao, R. Hao, D. Lu, Z. Lei, Appl. Surf. Sci. 420 (2017) 276–285, https://doi.org/10.1016/j.apsusc.2017.05.158.
[114] C. Xu, Y. Pan, G. Wan, H. Liu, L. Wang, H. Zhou, S.-H. Yu, H.-L. Jiang, J. Am. Chem. Soc. 141 (2019) 19110–19117, https://doi.org/10.1021/jacs.9b09954.
[115] Y. Lee, S. Kim, H. Fei, J.K. Kang, S.M. Cohen, Chem. Commun. 51 (2015) 16549–16552, https://doi.org/10.1039/c5cc04506a.
[116] N. Ogiwara, H. Kobayashi, M. Inuka, Y. Nishiyama, P. Concepcion, F. Rey, H. Kitagawa, Nano Lett. 20 (2020) 426–432, https://doi.org/10.1021/acs.nanolett.9b04124.
[117] Z. Gu, L. Chen, B. Duan, Q. Luo, J. Liu, C. Duan, Chem. Commun. 52 (2016) 116–119, https://doi.org/10.1039/c5cc07042b.
[118] J.-H. Wang, S.-Z. Huang, S.-S. Yang, Y.-L. Chen, Y.-M. Wu, N.-N. Li, X.-Y. Dong, F.-F. Li, Z. Anorg, Allg. Chem. 645 (2019) 706–711, https://doi.org/10.1002/zaac.201900048.
[119] Y.-H. Li, J.-Y. Li, Y.-J. Xu, EnergyChem 3 (2021), https://doi.org/10.1016/j.enchem.2020.100047 100047.
[120] J. Zhang, T. Bai, H. Huang, M.-H. Yu, X. Fan, Z. Chang, X.-H. Bu, Adv. Mater. (2020) 2004747, https://doi.org/10.1002/adma.202004747.
[121] S. Mao, J.-W. Shi, G. Sun, D. Ma, C. He, Z. Pu, K. Song, Y. Cheng, Appl. Catal., B, 282 (2021) 119550. 10.1016/j.apcatb.2020.119550.
[122] J.-D. Xiao, Q. Shang, Y. Xiong, Q. Zhang, Y. Luo, S.-H. Yu, H.-L. Jiang, Angew. Chem. Int. Ed. 55 (2016) 9389–9393, https://doi.org/10.1002/anie.201603990.
[123] L. Cao, Q. Luo, W. Liu, Y. Lin, X. Liu, Y. Cao, W. Zhang, Y. Wu, J. Yang, T. Yao, S. Wei, Nat. Catal. 2 (2019) 134–141, https://doi.org/10.1038/s41929-018-0203-5.
[124] H. Fei, J. Dong, Y. Feng, C.S. Allen, C. Wan, B. Volosskiy, M. Li, Z. Zhao, Y. Wang, H. Sun, P. An, W. Chen, Z. Guo, C. Lee, D. Chen, I. Shakir, M. Liu, T. Hu, Y. Li, A.I. Kirkland, X. Duan, Y. Huang, Nat. Catal. 1 (2018) 63–72, https://doi.org/10.1038/s41929-017-0008-y.
[125] E.D. Goodman, A.C. Johnston-Peck, E.M. Dietze, C.J. Wrasman, A.S. Hoffman, F. Abild-Pedersen, S.R. Bare, P.N. Plessow, M. Cargnello, Nat. Catal. 2 (2019) 748–755, https://doi.org/10.1038/s41929-019-0328-1.
[126] K. Jiang, S. Back, A.J. Akey, C. Xia, Y. Hu, W. Liang, D. Schaak, E. Stavitski, J.K. Nørskov, S. Siahrostami, H. Wang, Nat. Commun. 10 (2019) 3997, https://doi.org/10.1038/s41467-019-11992-2.
[127] D. Liu, X. Li, S. Chen, H. Yan, C. Wang, C. Wu, Y.A. Haleem, S. Duan, J. Lu, B. Ge, P.M. Ajayan, Y. Luo, J. Jiang, L. Song, Nat. Energy 4 (2019) 512–518, https://doi.org/10.1038/s41560-019-0402-6.
[128] J.-C. Liu, H. Xiao, J. Li, J. Am. Chem. Soc. 142 (2020) 3375–3383, https://doi.org/10.1021/jacs.9b06808.
[129] J. Mao, C.-T. He, J. Pei, Y. Liu, J. Li, W. Chen, D. He, D. Wang, Y. Li, Nano Lett. 20 (2020) 3442–3448, https://doi.org/10.1021/acs.nanolett.0c00364.
[130] H.B. Yang, S.-F. Hung, S. Liu, K. Yuan, S. Miao, L. Zhang, X. Huang, H.-Y. Wang, W. Cai, R. Chen, J. Gao, X. Yang, W. Chen, Y. Huang, H.M. Chen, C.M. Li, T. Zhang, B. Liu, Nat. Energy 3 (2018) 140–147, https://doi.org/10.1038/s41560-017-0078-8.
[131] X.-F. Yang, A. Wang, B. Qiao, J. Li, J. Liu, T. Zhang, Acc. Chem. Res. 46 (2013) 1740–1748, https://doi.org/10.1021/ar300361m.
[132] Y. Yao, Z. Huang, P. Xie, L. Wu, L. Ma, T. Li, Z. Pang, M. Jiao, Z. Liang, J. Gao, Y. He, D.J. Kline, M.R. Zachariah, C. Wang, J. Lu, T. Wu, T. Li, C. Wang, R. Shahbazian-Yassar, L. Hu, Nat. Nanotechnol. 14 (2019) 851–857, https://doi.org/10.1038/s41565-019-0518-7.
[133] B. Zhang, G. Sun, S. Ding, H. Asakura, J. Zhang, P. Sautet, N. Yan, J. Am. Chem. Soc. 141 (2019) 8185–8197, https://doi.org/10.1021/jacs.9b00486.
[134] J. Zhang, C. Zheng, M. Zhang, Y. Qiu, Q. Xu, W.-C. Cheong, W. Chen, L. Zheng, L. Gu, Z. Hu, D. Wang, Y. Li, Nano Res. 13 (2020) 3082–3087, https://doi.org/10.1007/s12274-020-2977-4.
[135] G. Wang, C.-T. He, R. Huang, J. Mao, D. Wang, Y. Li, J. Am. Chem. Soc. 142 (2020) 19339–19345, https://doi.org/10.1021/jacs.0c09599.
[136] X. Ma, H. Liu, W. Yang, G. Mao, L. Zheng, H.L. Jiang, J. Am. Chem. Soc. 143 (2021) 12220–12229, https://doi.org/10.1021/jacs.1c05032.
[137] J. He, J. Wang, Y. Chen, J. Zhang, D. Duan, Y. Wang, Z. Yan, Chem. Commun. 50 (2014) 7063–7066, https://doi.org/10.1039/c4cc01086h.
[138] Z. Jin, H. Yang, Nanoscale Res. Lett. 12 (2017) 539, https://doi.org/10.1186/s11671-017-2311-6.
[139] S. Min, G. Lu, J. Phys. Chem. C 116 (2012) 19644–19652, https://doi.org/10.1021/jp304022f.
[140] Y. Wang, J. Hong, W. Zhang, R. Xu, Catal, Sci. Technol. 3 (2013) 1703–1711, https://doi.org/10.1039/c3cy20836b.
[141] Y.-P. Yuan, L.-S. Yin, S.-W. Cao, G.-S. Xu, C.-H. Li, C. Xue, Appl. Catal., B, 168 (2015) 572-576. 10.1016/j.apcatb.2014.11.007.
[142] Y.-F. Chen, L.-L. Tan, J.-M. Liu, S. Qin, Z.-Q. Xie, J.-F. Huang, Y.-W. Xu, L.-M. Xiao, C.-Y. Su, Appl. Catal., B, 206 (2017) 426-433. https://doi.org/10.1016/j.apcatb.2017.01.040
[143] G. Kumar, P. Solanki, M. Nazish, S. Neogi, R.I. Kureshy, N.-u.H. Khan, J. Catal., 371 (2019) 298-304. 10.1016/j.jcat.2019.02.011.

[144] J. Shi, F. Chen, L. Hou, G. Li, Y. Li, X. Guan, H. Liu, L. Guo, Appl. Catal., B, 280 (2021) 119385. 10.1016/j.apcatb.2020.119385.
[145] Y. Zhang, Z. Jin, PCCP 21 (2019) 8326–8341, https://doi.org/10.1039/c9cp01180c.
[146] X. Tong, Z. Yang, J. Feng, Y. Li, H. Zhang, Appl. Organomet. Chem. 32 (2018), https://doi.org/10.1002/aoc.4049 e4049.
[147] C. Wang, Y. Xue, P. Wang, Y. Ao, J. Alloy. Compd. 748 (2018) 314–322, https://doi.org/10.1016/j.jallcom.2018.03.129.
[148] L. Shi, T. Wang, H. Zhang, K. Chang, J. Ye, Adv. Funct. Mater. 25 (2015) 5360–5367, https://doi.org/10.1002/adfm.201502253.
[149] R. Bariki, D. Majhi, K. Das, A. Behera, B.G. Mishra, Appl. Catal., B, 270 (2020) 118882. 10.1016/j.apcatb.2020.118882.
[150] W. Dong, D. Wang, H. Wang, M. Li, F. Chen, F. Jia, Q. Yang, X. Li, X. Yuan, J. Gong, H. Li, J. Ye, J. Colloid Interface Sci. 535 (2019) 444–457, https://doi.org/10.1016/j.jcis.2018.10.008.
[151] X. Zhang, Y. Yang, W. Huang, Y. Yang, Y. Wang, C. He, N. Liu, M. Wu, L. Tang, Mater. Res. Bull. 99 (2018) 349–358, https://doi.org/10.1016/j.materresbull.2017.11.028.
[152] B. Liu, X. Liu, J. Liu, C. Feng, Z. Li, C. Li, Y. Gong, L. Pan, S. Xu, C.Q. Sun, Appl. Catal., B, 226 (2018) 234-241. 10.1016/j.apcatb.2017.12.052.
[153] K.T. Ranjit, B. Viswanathan, J. Photochem. Photobiol., A 108 (1997) 79–84, https://doi.org/10.1016/S1010-6030(97)00005-1.
[154] K. Vinodgopal, P.V. Kamat, Environ. Sci. Technol. 29 (1995) 841–845, https://doi.org/10.1021/es00003a037.
[155] J. Low, J. Yu, M. Jaroniec, S. Wageh, A.A. Al-Ghamdi, Adv. Mater. 29 (2017) 1601694, https://doi.org/10.1002/adma.201601694.
[156] Y. Ma, Q. Tang, W.-Y. Sun, Z.-Y. Yao, W. Zhu, T. Li, J. Wang, Appl. Catal., B, 270 (2020) 118856. 10.1016/j.apcatb.2020.118856.
[157] Y. Su, Z. Zhang, H. Liu, Y. Wang, Appl. Catal., B, 200 (2017) 448-457. 10.1016/j.apcatb.2016.07.032.
[158] R. Marschall, Adv. Funct. Mater. 24 (2014) 2421–2440, https://doi.org/10.1002/adfm.201303214.
[159] H. Zhou, Y. Qu, T. Zeid, X. Duan, Energy Environ. Sci. 5 (2012) 6732–6743, https://doi.org/10.1039/C2EE03447F.
[160] S.J.A. Moniz, S.A. Shevlin, D.J. Martin, Z.-X. Guo, J. Tang, Energy Environ. Sci. 8 (2015) 731–759, https://doi.org/10.1039/C4EE03271C.
[161] A. Crake, K.C. Christoforidis, A. Kafizas, S. Zafeiratos, C. Petit, Appl. Catal., B, 210 (2017) 131-140. 10.1016/j.apcatb.2017.03.039.
[162] Y.-X. Li, X. Wang, C.-C. Wang, H. Fu, Y. Liu, P. Wang, C. Zhao, J. Hazard. Mater. 399 (2020), https://doi.org/10.1016/j.jhazmat.2020.123085 123085.
[163] L. Wang, P. Jin, S. Duan, H. She, J. Huang, Q. Wang, Science Bulletin 64 (2019) 926–933, https://doi.org/10.1016/j.scib.2019.05.012.
[164] L. Shen, S. Liang, W. Wu, R. Liang, L. Wu, J. Mater. Chem. A 1 (2013) 11473–11482, https://doi.org/10.1039/c3ta12645e.
[165] H. Zhao, X. Yang, R. Xu, J. Li, S. Gao, R. Cao, J. Mater. Chem. A 6 (2018) 20152–20160, https://doi.org/10.1039/c8ta05970e.
[166] J.-J. Zhou, R. Wang, X.-L. Liu, F.-M. Peng, C.-H. Li, F. Teng, Y.-P. Yuan, Appl. Surf. Sci. 346 (2015) 278–283, https://doi.org/10.1016/j.apsusc.2015.03.210.
[167] X. Peng, L. Ye, Y. Ding, L. Yi, C. Zhang, Z. Wen, Appl. Catal., B, 260 (2020) 118152. 10.1016/j.apcatb.2019.118152.
[168] Y. Chen, D. Yang, B. Shi, W. Dai, H. Ren, K. An, Z. Zhou, Z. Zhao, W. Wang, Z. Jiang, J. Mater. Chem. A., 8 (2020) 7724-7732. doi: 10.1039/d0ta00901f.
[169] F. Li, D. Wang, Q.-J. Xing, G. Zhou, S.-S. Liu, Y. Li, L.-L. Zheng, P. Ye, J.-P. Zou, Appl. Catal., B, 243 (2019) 621-628. 10.1016/j.apcatb.2018.10.043.
[170] Z. Wang, Z. Jin, H. Yuan, G. Wang, B. Ma, J. Colloid Interface Sci., 532 (2018) 287-299. doi: 10.1016/j.jcis.2018.07.138.
[171] X. Zhang, H. Dong, X.-J. Sun, D.-D. Yang, J.-L. Sheng, H.-L. Tang, X.-B. Meng, F.-M. Zhang, ACS Sustainable Chem. Eng. 6 (2018) 11563–11569, https://doi.org/10.1021/acssuschemeng.8b01740.
[172] Y. Zhang, J. Zhou, Q. Feng, X. Chen, Z. Hu, Chemosphere 212 (2018) 523–532, https://doi.org/10.1016/j.chemosphere.2018.08.117.
[173] R. Bibi, Q. Shen, L. Wei, D. Hao, N. Li, J. Zhou, RSC Adv. 8 (2018) 2048–2058, https://doi.org/10.1039/c7ra11500h.
[174] Z. Sha, J. Sun, H.S.O. Chan, S. Jaenicke, J. Wu, RSC Adv. 4 (2014) 64977–64984, https://doi.org/10.1039/c4ra13000f.
[175] S. Wan, M. Ou, Q. Zhong, X. Wang, Chem. Eng. J. 358 (2019) 1287–1295, https://doi.org/10.1016/j.cej.2018.10.120.
[176] X. Wang, X. Zhao, D. Zhang, G. Li, H. Li, Appl. Catal., B, 228 (2018) 47-53. 10.1016/j.apcatb.2018.01.066
[177] Q. Liang, M. Zhang, Z. Zhang, C. Liu, S. Xu, Z. Li, J. Alloys Compd., 690 (2017) 123-130. doi: 10.1016/j.jallcom.2016.08.087.
[178] A.J. Bard, J. Photochem., 10 (1979) 59-75. 10.1016/0047-2670(79)80037-4.
[179] N. Tian, H. Huang, Y. He, Y. Guo, T. Zhang, Y. Zhang, Dalton Trans. 44 (2015) 4297–4307, https://doi.org/10.1039/C4DT03905J.
[180] H. Zeng, Z. Yu, L. Shao, X. Li, M. Zhu, Y. Liu, X. Feng, X. Zhu, Desalination 491 (2020), https://doi.org/10.1016/j.desal.2020.114558 114558.
[181] Y. Wang, L. Guo, Y. Zeng, H. Guo, S. Wan, M. Ou, S. Zhang, Q. Zhong, A.C.S. Appl, Mater. Interfaces 11 (2019) 30673–30681, https://doi.org/10.1021/acsami.9b04302.
[182] X.-H. Yi, S.-Q. Ma, X.-D. Du, C. Zhao, H. Fu, P. Wang, C.-C. Wang, Chem. Eng. J. 375 (2019), https://doi.org/10.1016/j.cej.2019.121944 121944.
[183] S. Subudhi, S. Mansingh, G. Swain, A. Behera, D. Rath, K. Parida, Inorg. Chem. 58 (2019) 4921–4934, https://doi.org/10.1021/acs.inorgchem.8b03544.
[184] H. Fakhri, H. Bagheri, J. Environ. Sci. 91 (2020) 222–236, https://doi.org/10.1016/j.jes.2020.01.013.
[185] J. Meng, Q. Chen, J. Lu, H. Liu, A.C.S. Appl, Mater. Interfaces 11 (2019) 550–562, https://doi.org/10.1021/acsami.8b14282.
[186] Y. Wen, J. Zhang, Q. Xu, X.-T. Wu, Q.-L. Zhu, Coord. Chem. Rev. 376 (2018) 248–276, https://doi.org/10.1016/j.ccr.2018.08.012.
[187] Z. Liang, C. Qu, W. Guo, R. Zou, Q. Xu, Adv. Mater. 30 (2018) 1702891, https://doi.org/10.1002/adma.201702891.
[188] S. Zhu, D. Wang, Adv. Energy Mater. 7 (2017) 1700841, https://doi.org/10.1002/aenm.201700841.
[189] Z. Cheng, W. Qi, C.H. Pang, T. Thomas, T. Wu, S. Liu, M. Yang, Adv. Funct. Mater. 31 (2021) 2100553, https://doi.org/10.1002/adfm.202100553.
[190] X. Tan, H. Lai, B. Gu, Y. Zeng, H. Li, Energy Policy 118 (2018) 429–439, https://doi.org/10.1016/j.enpol.2018.03.072.
[191] G. Xu, W. Wang, Energy 195 (2020), https://doi.org/10.1016/j.energy.2020.117045 117045.
[192] N. Zhou, N. Khanna, W. Feng, J. Ke, M. Levine, Nat. Energy 3 (2018) 978–984, https://doi.org/10.1038/s41560-018-0253-6.
[193] Y. Zhang, Nat. Rev. Chem. 1 (2017) 0057, https://doi.org/10.1038/s41570-017-0057.
[194] A. Schoedel, Z. Ji, O.M. Yaghi, Nat. Energy 1 (2016) 16034, https://doi.org/10.1038/nenergy.2016.34.
[195] S. Tonda, S. Kumar, M. Bhardwaj, P. Yadav, S. Ogale, A.C.S. Appl, Mater. Interfaces 10 (2018) 2667–2678, https://doi.org/10.1021/acsami.7b18835.
[196] M. Marszewski, S. Cao, J. Yu, M. Jaroniec, Mater. Horiz. 2 (2015) 261–278, https://doi.org/10.1039/C4MH00176A.
[197] Q. Yang, A.D. Wiersum, P.L. Llewellyn, V. Guillerm, C. Serred, G. Maurin, Chem. Commun. 47 (2011) 9603–9605, https://doi.org/10.1039/c1cc13543k.
[198] G.E. Cmarik, M. Kim, S.M. Cohen, K.S. Walton, Langmuir 28 (2012) 15606–15613, https://doi.org/10.1021/la3035352.
[199] J. Shen, G. Liu, K. Huang, Q. Li, K. Guan, Y. Li, W. Jin, J. Membr. Sci. 513 (2016) 155–165, https://doi.org/10.1016/j.memsci.2016.04.045.
[200] Y.-F. Xu, M.-Z. Yang, B.-X. Chen, X.-D. Wang, H.-Y. Chen, D.-B. Kuang, C.-Y. Su, J. Am. Chem. Soc. 139 (2017) 5660–5663, https://doi.org/10.1021/jacs.7b00489.
[201] Z. Zheng, H. Xu, Z. Xu, J. Ge, Small 14 (2018) 1702812, https://doi.org/10.1002/smll.201702812.
[202] C. Bie, B. Cheng, J. Fan, W. Ho, J. Yu, EnergyChem 3 (2021), https://doi.org/10.1016/j.enchem.2021.100051 100051.
[203] S. Kreft, D. Wei, H. Junge, M. Beller, EnergyChem 2 (2020), https://doi.org/10.1016/j.enchem.2020.100044 100044.
[204] X. Wang, G. Yang, G. Chai, M.S. Nasir, S. Wang, X. Zheng, C. Wang, W. Yan, Int. J. Hydrogen Energy 45 (2020) 30634–30646, https://doi.org/10.1016/j.ijhydene.2020.08.273.
[205] W. Zhu, P. Liu, S. Xiao, W. Wang, D. Zhang, H. Li, Appl. Catal., B, 172-173 (2015) 46-51. 10.1016/j.apcatb.2015.02.003.
[206] D. Zhang, P. Liu, S. Xiao, X. Qian, H. Zhang, M. Wen, Y. Kuwahara, K. Mori, H. Li, H. Yamashita, Nanoscale 8 (2016) 7749–7754, https://doi.org/10.1039/C5NR07505J.
[207] W.H. Koppenol, J.D. Rush, J. Phys. Chem. 91 (1987) 4429–4430, https://doi.org/10.1021/j100300a045.
[208] C. Liu, T.R. Cundari, A.K. Wilson, J. Phys. Chem. C 116 (2012) 5681–5688, https://doi.org/10.1021/jp210480c.
[209] C.-F. Fu, X. Wu, J. Yang, Adv. Mater. 30 (2018) 1802106, https://doi.org/10.1002/adma.201802106.
[210] Z. Wang, C. Li, K. Domen, Chem. Soc. Rev. 48 (2019) 2109–2125, https://doi.org/10.1039/C8CS00542G.
[211] X. Chen, S. Shen, L. Guo, S.S. Mao, Chem. Rev. 110 (2010) 6503–6570, https://doi.org/10.1021/cr1001645.
[212] H. Wang, L. Zhang, Z. Chen, J. Hu, S. Li, Z. Wang, J. Liu, X. Wang, Chem. Soc. Rev. 43 (2014) 5234–5244, https://doi.org/10.1039/C4CS00126E.
[213] P. Zhang, D. Luan, X.W. Lou, Adv. Mater. 32 (2020) 2004561, https://doi.org/10.1002/adma.202004561.
[214] L. Wang, Y. Zhang, L. Chen, H. Xu, Y. Xiong, Adv. Mater. 30 (2018) 1801955, https://doi.org/10.1002/adma.201801955.
[215] Y. Liu, H. Cheng, M. Cheng, Z. Liu, D. Huang, G. Zhang, B. Shao, Q. Liang, S. Luo, T. Wu, S. Xiao, Chem. Eng. J. (2020), https://doi.org/10.1016/j.cej.2020.127914 127914.
[216] Y. Liu, D.L. Huang, M. Cheng, Z.F. Liu, C. Lai, C. Zhang, C.Y. Zhou, W.P. Xiong, L. Qin, B.B. Shao, Q.H. Liang, Coord. Chem. Rev. 409 (2020), https://doi.org/10.1016/j.ccr.2020.213220 213220.
[217] Y. Wang, L. Ling, W. Zhang, K. Ding, Y. Yu, W. Duan, B. Liu, ChemSusChem 11 (2018) 666–671, https://doi.org/10.1002/cssc.201702316.
[218] L. Shen, M. Luo, Y. Liu, R. Liang, F. Jing, L. Wu, Appl. Catal., B, 166 (2015) 445-453. 10.1016/j.apcatb.2014.11.056.
[219] C.B. Liu, L.L. Wang, Y.H. Tang, S.L. Luo, Y.T. Liu, S.Q. Zhang, Y.X. Zeng, Y.Z. Xu, Appl. Catal., B, 164 (2015) 1-9. doi: 10.1016/j.apcatb.2014.08.046.
[220] Y. Hou, A.B. Laursen, J. Zhang, G. Zhang, Y. Zhu, X. Wang, S. Dahl, I. Chorkendorff, Angew. Chem. Int. Ed. 52 (2013) 3621–3625, https://doi.org/10.1002/anie.201210294.
[221] Y. Liu, M. Cheng, Z. Liu, G. Zeng, H. Zhong, M. Chen, C. Zhou, W. Xiong, B. Shao, B. Song, Chemosphere 236 (2019), https://doi.org/10.1016/j.chemosphere.2019.124387 124387.
[222] L. Li, C. Lai, F. Huang, M. Cheng, G. Zeng, D. Huang, B. Li, S. Liu, M. Zhang, L. Qin, M. Li, J. He, Y. Zhang, L. Chen, Water Res. 160 (2019) 238–248, https://doi.org/10.1016/j.watres.2019.05.081.
[223] D. Huang, G. Zhang, J. Yi, M. Cheng, C. Lai, P. Xu, C. Zhang, Y. Liu, C. Zhou, W. Xue, R. Wang, Z. Li, S. Chen, Chemosphere 263 (2021), https://doi.org/10.1016/j.chemosphere.2020.127672 127672.

[224] F. Qin, Y. Peng, G. Song, Q. Fang, R. Wang, C. Zhang, G. Zeng, D. Huang, C. Lai, Y. Zhou, X. Tan, M. Cheng, S. Liu, J. Hazard. Mater. 398 (2020), https://doi.org/10.1016/j.jhazmat.2020.122816 122816.
[225] M. Cheng, G.M. Zeng, D.L. Huang, C. Lai, Y. Liu, C. Zhang, J. Wan, L. Hu, C.Y. Zhou, W.P. Xiong, Water Res. 138 (2018) 7–18, https://doi.org/10.1016/j.watres.2018.03.022.
[226] M. Cheng, G.M. Zeng, D.L. Huang, C. Lai, P. Xu, C. Zhang, Y. Liu, Chem. Eng. J. 284 (2016) 582–598, https://doi.org/10.1016/j.cej.2015.09.001.
[227] Z. Sha, H.S.O. Chan, J. Wu, J. Hazard. Mater. 299 (2015) 132–140, https://doi.org/10.1016/j.jhazmat.2015.06.016.
[228] J. Cao, Z.-H. Yang, W.-P. Xiong, Y.-Y. Zhou, Y.-R. Peng, X. Li, C.-Y. Zhou, R. Xu, Y.-R. Zhang, Chem. Eng. J. 353 (2018) 126–137, https://doi.org/10.1016/j.cej.2018.07.060.
[229] D. Xu, B. Cheng, S. Cao, J. Yu, Appl. Catal., B, 164 (2015) 380-388. 10.1016/j.apcatb.2014.09.051.
[230] H. Nguyen Thi Thu, O.V. Lefedova, H. Nguyen Ngoc, Russ. J. Phys. Chem. A, 90 (2016) 220-225. 10.1134/s0036024415120201.
[231] C. Feng, Z. Wang, Y. Ma, Y. Zhang, L. Wang, Y. Bi, Appl. Catal., B, 205 (2017) 19-23. 10.1016/j.apcatb.2016.12.014.
[232] Y. Xue, P. Wang, C. Wang, Y. Ao, Chemosphere 203 (2018) 497–505, https://doi.org/10.1016/j.chemosphere.2018.04.017.
[233] K.K. Krishnani, S. Ayyappan, Heavy metals remediation of water using plants and lignocellulosic agrowastes, in: G.W. Ware, D.M. Whitacre, L.A. Albert, P. de Voogt, C.P. Gerba, O. Hutzinger, J.B. Knaak, F.L. Mayer, D.P. Morgan, D.L. Park, R.S. Tjeerdema, R.S.H. Yang, F.A. Gunther (Eds.), Reviews of Environmental Contamination and Toxicology: Continuation of Residue Reviews, Springer, New York, New York, NY, 2006, pp. 59–84.
[234] W.J. Wang, Q.Y. Niu, G.M. Zeng, C. Zhang, D.L. Huang, B.B. Shao, C.Y. Zhou, Y. Yang, Y.X. Liu, H. Guo, W.P. Xiong, L. Lei, S.Y. Liu, H. Yi, S. Chen, X. Tang, Appl. Catal., B, 273 (2020) 119051. doi: 10.1016/j.apcatb.2020.119051.
[235] C.-C. Wang, X.-D. Du, J. Li, X.-X. Guo, P. Wang, J. Zhang, Appl. Catal., B, 193 (2016) 198-216. 10.1016/j.apcatb.2016.04.030.
[236] F. Zhang, Y. Zhang, C. Zhou, Z. Yang, H. Xue, D.D. Dionysiou, Chem. Eng. J. 324 (2017) 140–153, https://doi.org/10.1016/j.cej.2017.05.009.
[237] H. Wang, X. Yuan, Y. Wu, G. Zeng, X. Chen, L. Leng, Z. Wu, L. Jiang, H. Li, J. Hazard. Mater. 286 (2015) 187–194, https://doi.org/10.1016/j.jhazmat.2014.11.039.
[238] J.J. Testa, M.A. Grela, M.I. Litter, Langmuir 17 (2002) 3515–3517, https://doi.org/10.1021/la010100y.
[239] J.-C. Wang, J. Ren, H.-C. Yao, L. Zhang, J.-S. Wang, S.-Q. Zang, L.-F. Han, Z.-J. Li, J. Hazard. Mater. 311 (2016) 11–19, https://doi.org/10.1016/j.jhazmat.2016.02.055.
[240] C.A. Trickett, K.J. Gagnon, S. Lee, F. Gandara, H.-B. Buergi, O.M. Yaghi, Angew. Chem. Int. Ed. 54 (2015) 11162–11167, https://doi.org/10.1002/anie.201505461.
[241] G.C. Shearer, S. Forselv, S. Chavan, S. Bordiga, K. Mathisen, M. Bjorgen, S. Svelle, K.P. Lillerud, Top. Catal. 56 (2013) 770–782, https://doi.org/10.1007/s11244-013-0027-0.
[242] S. Leong, A. Razmjou, K. Wang, K. Hapgood, X. Zhang, H. Wang, J. Membr. Sci. 472 (2014) 167–184, https://doi.org/10.1016/j.memsci.2014.08.016.
[243] X.-D. Du, X.-H. Yi, P. Wang, W. Zheng, J. Deng, C.-C. Wang, Chem. Eng. J. 356 (2019) 393–399, https://doi.org/10.1016/j.cej.2018.09.084.
[244] X. Liu, N.K. Demir, Z. Wu, K. Li, J. Am. Chem. Soc. 137 (2015) 6999–7002, https://doi.org/10.1021/jacs.5b02276.